Electron Field Emission from Carbons and Their Emission Mechanism

Chun Hwa Patrick Poa

Submitted for the Degree of
Doctor of Philosophy
from the
University of Surrey

UniS

Large Area Electronics Group
Advanced Technology Institute
School of Electronics and Physical Sciences
University of Surrey
Guildford, Surrey GU2 7XH, United Kingdom.

December 2002

Abstract

This thesis is concerned with the research of the electron field emission properties of carbon based materials. Low emission threshold fields have been observed from both amorphous carbon thin films and carbon nanotubes. The emission mechanism can be subdivided into two groups depending on the type of electric field enhancement. These are the amorphous carbon flat films with non-geometric field enhancement and carbon nanotubes with high surface geometric field enhancement.

Amorphous carbon thin films are deposited using an rf-plasma enhanced chemical vapour deposition technique. Changing the deposition conditions such as the addition of Argon or Nitrogen modifies the electronic properties. This induces variations in the sp^2 concentration and its distribution within the films. The electron field emission properties from amorphous carbon thin films show a close relationship to its sp^2 configuration. A model based on non-geometric field enhancement is proposed to explain the variation in the field emission characteristics. Nano-structured amorphous carbon films custom "designed" using ion beam assisted deposition with sp^2 cluster sizes of around 60 nm have also been investigated. The field emission threshold field was shown to be controlled by the film's intrinsic stress and the local carbon density. With increasing stress, there is a concomitant increase in the local density, which is postulated to decrease the distance between the carbon graphitic "planes". This results in enhancement of the electron emission at lower fields. Stress within the films also induces changes to the band structure of the nano-structured carbon which are beneficial to the field emission process.

Field emission from carbon nanotubes that are embedded in a polymer matrix has been investigated. The emission threshold fields are observed to be dependent on the nanotube density. The effect of electric field screening is used to explain the reduction of field enhancement observed in these films with increasing nanotube density. The field emission properties are compared with those films which have vertically aligned and in e-beam fabricated nanotube arrays. Results indicate that field emission properties from non-aligned nanotube films are comparable in performance to the best designed arrays in the literature.

Although this study shows carbon based materials to have superior field emission properties, integrating the cathodes to fabricate commercial devices could prove to be very challenging.

Acknowledgments

I would like to thank my supervisor, Prof. S.R.P. Silva for all his kind advice, guidance and support. I am indebted to him for both my undergraduate and postgraduate studies in the University of Surrey. I have been exposed to quality research where we are presently at the cutting edge of the carbon-based material electronics.

I would also like to acknowledge the research fellows of the Large Area Electronics group who have in one way or another contributed to my studies at this university. Dr. David Carey, Dr. Roy Forrest, Dr. Dagou Zeze, Dr. David Cox, Dr. Vlad Stolojan. I am also grateful to the postgraduate students such as G.Y. Chen, Richard Smith, Damitha Adikaari and Patrick Too for their support. In addition, I have to thank Dr Riz Khan for the initial work of this project, especially his guidance on the thin film deposition and analysis.

I must also thank the co-workers at the University of Sussex, United Kingdom Dr Kuang Hsu, Paul Watts, Dr David Walton and Prof. Sir Harry Kroto. I also have to thank Dr Rodrigo Lacerda and Dr. Francisco Marques from the Universidade Estadual de Campinas, Brazil. In particular Dr Lacerda has been the one who has motivated me into research. I have learned much from his experience, especially during his 6 month stay at Surrey.

Financial support from my studies was provided by a University of Surrey Research Studentship (URS) and a CVCP Overseas Research Studentship (ORS). Support received is gratefully acknowledged.

Finally, I would like to thank my family and friends for their support, without them I would not have been able to complete my studies.

Glossary

AC	Alternating current
a-C	Amorphous carbon
a-C:H	Hydrogentaed amorphous carbon
AFM	Atomic force microscopy
B-MWNT	Boron doped multi-walled nanotube
CNT	Carbon nanotube
CVD	Chemical vapour deposition
DAC	Diamond-like amorphous carbon
DC	Direct current
E_C	Conduction band minimum
EELS	Electron energy loss spectroscopy
E_F	Fermi level
E_{th}	Field emission threshold
E_V	Valence band maximum
FE	Field emission
F-N	Fowler-Nordheim
GAC	Graphite-like amorphous carbon
IBAD	Ion beam assisted deposition
ITO	Indium-tin oxide
MWNT	Multi-walled carbon nanotube
PAC	Polymer-like amorphous carbon
PECVD	Plasma enhanced chemical vapour deposition
PS	Polystyrene
PTFE	Polytetrafluoroethylene

RBS	Rutherford back-scattering spectroscopy
SEM	Scanning electron microscopy
STM	Scanning tunnelling electron microscopy
SWNT	Single-walled carbon nanotube
TAC	Tetrahedral amorphous carbon
TEM	Transmission electron microscopy
XPS	X-ray Photoelectron spectroscopy

Declaration

This thesis is submitted for the degree of Doctor of Philosophy at the University of Surrey. It describes the research carried out in the Advanced Technology Institute of the School of Electronics and Physical Sciences between October 1999 and September 2002. This work has been carried out under the supervision of Professor S. R. P. Silva, head of the Large Area Electronics group. Except where referenced, this work is original and has not been the result of collaboration. No part of this thesis has been or is currently being submitted for any other degree, diploma or other qualification.

C.H.P. Poa
December 2002

Key words: Field emission, amorphous carbon, carbon nanotubes, and field emission mechanism.

Email: c.poa@eim.surrey.ac.uk

Contents

Abstract i
Acknowledgements ii
Glossary iii
Declaration v

1 **Introduction** 1
1.1 Carbon based materials as electron sources 1
1.2 Project aim 2
1.3 Outline of thesis 2

2 **Literature Review** 4
2.1 Carbon in its different forms 4
2.2 Field emission mechanism 6
2.2.1 Fowler-Nordheim Theory 7
2.2.2 Hot electron induced emission 12
2.2.3 Negative Electron Affinity 13
2.2.4 Field Enhancement from Carbon Structures 14
2.3 Field emission from carbon based material 16
2.3.1 Tetrahedral Amorphous Carbon Films 17
2.3.2 Diamond-like Amorphous Carbon 20
2.3.3 Polymer-like Amorphous Carbon 21
2.3.4 Graphite-like Amorphous Carbon 22
2.3.5 Carbon Nanotubes 24
2.4 Summary 28

3 **Experimental Techniques** 30
3.1 Thin film deposition 30
3.1.1 Ion beam assisted deposition technique 30
3.1.2 Radio-frequency plasma enhanced chemical vapour deposition technique 32
3.2 Carbon nanotube-polystyrene composite preparation 33

3.3 Thin film characterisation ... 34
  3.3.1 Ellipsometry ... 35
  3.3.2 Optical absorption spectroscopy ... 36
  3.3.3 Intrinsic stress measurement ... 36
  3.3.4 Photoelectron spectroscopy ... 37
  3.3.5 Electron-energy-loss spectroscopy ... 39
3.4 Microscopy techniques ... 40
  3.4.1 Scanning electron microscopy ... 40
  3.4.2 Scanning probe microscopy ... 41
3.5 Field emission characterisation ... 42
  3.5.1 Probe measurements ... 42
  3.5.2 Planar measurement / site density maps ... 43
  3.5.3 Comparison of planar and probe measurements ... 44

4 Physically-based device simulation ... 46

4.1 Silvaco simulation software ... 46
4.2 Specifying material properties ... 47
4.3 Field emission simulation models ... 48
4.4 Other Models ... 50

5 Field emission properties of polymer-like amorphous carbon thin films ... 51

5.1 Introduction ... 51
5.2 Effects of Argon dilution ... 51
  5.2.1 Experimental detail ... 52
  5.2.2 Thin films characterisation ... 53
  5.2.3 Field emission analysis ... 56
  5.2.4 Summary and discussions ... 57
5.3 Field emission from nitrogenated amorphous carbon ... 59
  5.3.1 Experimental detail ... 59
  5.3.2 Raman spectroscopy analysis ... 61
  5.3.3 Field emission analysis ... 64
  5.3.4 Summary and discussions ... 65
5.4 Surface treated amorphous carbon thin films ... 65
  5.4.1 Experimental detail ... 66

5.4.2 Field emission analysis 66
5.4.3 Summary and discussions 68
5.5 Summary 68

6 **Field emission properties of nanostructured graphite-like amorphous carbon films** 70

6.1 Introduction 70
6.2 Experimental conditions 70
6.3 Structural analysis 71
6.4 Intrinsic stress and carbon densities 73
6.5 STM and TEM investigations 77
6.6 Field emission properties 80
6.7 Simulation of two conductive spheres 83
6.8 Discussion 89
6.8.1 Structural properties 89
6.8.2 Effect of stress within the films 90
6.8.3 The field emission model 92
6.9 Summary 95

7 **Field emission properties of carbon nanotubes** 96

7.1 Introduction 96
7.2 Characteristics of the CNT-PS films 96
7.3 Field emission characteristics 102
7.3.1 Probe technique 102
7.3.2 Planar technique 104
7.3.3 Field emission site density 106
7.4 Discussion 112
7.4.1 Fowler-Nordheim analysis 112
7.4.2 Emission current density 113
7.4.3 Current saturation effects 116
7.4.4 Field emission model 123
7.5 Summary 124

8 Influence of external stress on the field emission properties ... 125

8.1 Introduction ... 125
8.2 Experimental setup ... 125
8.3 Effects of bending on a-C films ... 126
8.4 Effects of bending CNT-PS films ... 128
8.5 Summary and discussions ... 129

9 Conclusions ... 131

9.1 Amorphous carbon thin films ... 131
9.2 Carbon nanotubes ... 133
9.3 Suggestions for future research ... 134

References

Publications

Chapter 1

1 Introduction

Carbon is an unique element in terms of the many different forms that it can exist in. The great diversity of short, medium and long-range configurations has allowed carbon to be one of the most studied materials in the last 30 years. Two pure carbon crystalline forms have been well known, graphite that is based on threefold planar bonding, and diamond based on fourfold tetrahedral bonding. The recent addition to the carbon family has been the cage structured carbon. Perhaps the best known and the most abundant member is buckminsterfullene or C_{60}.[1] Shortly after the discovery of this fullerene family, carbon nanotubes were realised.[2] These nanometer diameter fibres with length of a few microns are predicted to have extraordinary mechanical, chemical and electronic properties. Nanotubes can be metallic or semi-conducting depending on the chirality of the structure, and this opens up interesting prospects into using carbon for future electronic applications. In the short-range ordered materials, amorphous carbon thin films have also shown increasingly good prospects. The only major industrial application for amorphous carbon has been limited to the passive applications such as in hard disk coating. The electronic applications of amorphous carbon have attracted the most interest. It is very easy to produce amorphous carbon at low temperature and over a large area, which has opened up the prospects of using these materials for devices.

One of the most promising applications for carbon based materials has been in the area of electron field emission. It is a vital process in vacuum microelectronic applications and flat panel field emission displays. With the current knowledge in both crystalline and amorphous carbons, active applications for these materials need to be developed.

1.1 Carbon based materials as electron sources

Electron sources are crucial in modern technologies. It is been predicted that the current cathode ray tube display will soon be phased out by liquid crystal and plasma displays. One of the most promising candidates for flat panel displays is based on field emission devices. Flat panel displays are currently dominated by liquid crystal displays. However, there are limitations to the current technology, the viewing angle, power consumption and brightness of these LCD's are considered as deficiencies when compared to current cathode ray tube displays. Field emission displays operate under similar conditions and principles as the cathode ray tube display. To produce electron field emission displays, atomically sharp tips such as Spindt tips [3] are required to allow low field electrons emission. Field emission devices can also be fabricated from metal and semiconductor microtips such as Mo and Si. However, the current field emission technology still lacks a material that is chemically and mechanically robust, cheap and easy to process and possess excellent field emission characteristics. Therefore, the investigation of carbon based material and its field emission properties are important. It has been shown that carbon based materials are unique in their field emission characteristics and they possess good mechanical and chemical properties.

1.2 Project aim

The aim of this study is to investigate the field emission characteristics of carbon based materials, especially the field emission mechanism. Thus far, there have been many field emission models proposed to explain the field emission characteristics of the carbon based materials. However, none are universally accepted as of yet and this results in a vacuum in our understanding to these materials and their potential for further electronic applications.

1.3 Outline of thesis

The first part of this thesis will review the background theories of carbon based materials and their properties. It includes the field emission mechanism and models proposed in the literature. The field emission properties and characteristics of carbon based materials such as amorphous carbon thin films and carbon nanotubes will be discussed. As the type of hybridisation within the amorphous carbon films is important for the electronics properties, discussion will be based on the field emission characteristics with different hybridisation composites. For the field emission properties of carbon nanotubes, the emphasis on the structure and deposition techniques will be compared.

In chapter 3, the experimental setup will discuss the techniques available to synthesise amorphous carbon thin films and carbon nanotubes. Following that the characterisation techniques for the carbon based materials will be explained. The field emission measurements will cover the two main techniques employed, namely the probe and planar techniques. Chapter 4 is dedicated to simulation work, where the simulation package and models used will be explained.

Chapter 5 and 6 will discuss and compare the field emission properties and characteristics of the amorphous carbon thin films. The effect of intrinsic stress on graphite-like amorphous carbon thin films is of particular interest, where changing the intrinsic stress changes the field emission properties. In Chapter 7, the field emission properties of carbon nanotubes will study the effect of electric field screening and the current density of the carbon nanotube-polymer composite thin films. Chapter 8 will discuss the application of externally applied stress on the amorphous carbon thin films and carbon nanotube-polymer composite thin films.

Finally, chapter 9 will summarise the results presented in this study and highlight the field emission properties of amorphous carbon thin film and carbon nanotubes. Suggestions for future work will also be discussed.

Chapter 2

2 Literature Review

This chapter will outline different forms of carbon-based materials and their properties. A wide range of carbon-based materials will be discussed, where changing the deposition process allows for the properties of these thin films to be either diamond-like or graphite-like in nature. The properties of carbon nanotubes will also be covered. Secondly, the proposed models for field emission in the literature will be examined. The emission mechanism will be explained in terms of a front surface or back contact related emission process.

2.1 Carbon in its different forms

The advancement in the science of carbon has been recently marked by the discovery of C_{60} and carbon nanotubes. This allows scientists to use these materials for future nanoscale science and technology studies. Also, the development of disordered carbons has benefited from this advancement, while a wide range of amorphous carbon containing fullerene-like clusters have been realised. More methods have been developed to synthesise amorphous carbon (a-C) and the growth of carbon material has been broadly understood.

Carbon exists in a great variety of crystalline and amorphous forms. The ability to configure carbon in three different hybridisations, sp^1, sp^2 and sp^3 allows different forms of carbon to exist. In the sp^3 hybridisation of carbon, the tetrahedral bonded carbon formed by strong σ bonds in adjacent atoms give rise to diamond-like properties. Diamond has a large band gap of 5.5 eV and undoped diamond at room temperature behaves like an insulator. Diamond is also the hardest known material with high hardness coefficient and highest atom density. Based on three-fold coordinated sp^2 network, the graphite-like configuration is formed by the in-plane σ bonds and a weaker out of plane π bond. Graphite has strong intra-layer σ bonding and yet weak bonding between its layers. At room temperature, a single graphite plane behaves as a semiconductor/metal with zero bandgap. Figure 2-1 shows the lattice structure of (a) a diamond structure (b) a graphite planar structure.

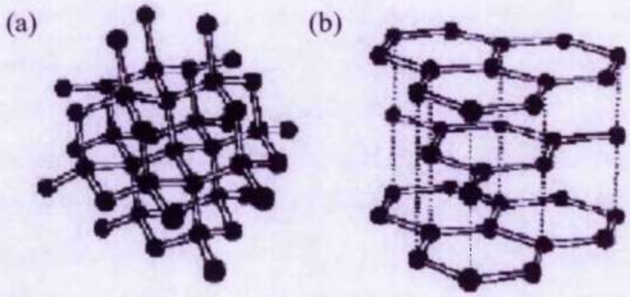

Figure 2-1: Illustration of (a) diamond lattice and (b) graphite planar structure.

Fullerenes are a new family of carbon caged structures, all based on a three-fold coordinated sp^2 network. C_{60} is the most abundant and best known member of this new carbon structure. The fullerene structure is unique in the sense that the molecules are edgeless, chargeless, and have no boundaries, no dangling bonds, and no unpaired electrons. These characteristics set the fullerenes apart from other crystalline structures such as graphite or diamond which have edges with dangling bonds and electrical charges. Such features allow these molecules, and particularly the C_{60} which is the most symmetrical, to spin with essentially no restraint at a very high rate. The first stable fullerene and the first to be discovered was the C_{60}. It is the dominant molecule with sixty carbon atoms arranged so that they form twenty hexagons, in addition to the necessary twelve pentagons, giving it the appearance of a soccer ball.

However, perhaps the most exciting discovery recently to the fullerene family is the carbon nanotubes (CNT). A single-wall carbon nanotube (SWNT) is a hollow cylinder, consisting of single graphite sheet wrapped round into a cylinder. CNTs possess extraordinary mechanical and electrical properties. The graphitic network provides strength and elasticity across the tube. SWNT can be metallic or semiconducting depending on the chirality of the tube structure. These have opened up a series of electronic applications for carbon based materials. Figure 2-2 illustrates the structure of (a) Carbon C_{60} molecule and (b) a single-walled carbon nanotube.

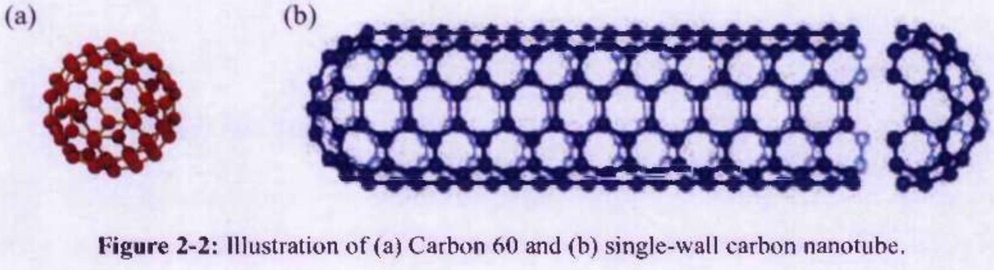

Figure 2-2: Illustration of (a) Carbon 60 and (b) single-wall carbon nanotube.

Carbon in its amorphous form can have a different mixture of hybridisation with or without the possible presence of hydrogen. The ternary phase diagram in Figure 2-3 shows the possible composition of the a-C. The left corner consists of a group of graphitic disordered carbon such as glassy carbon and evaporated a-C. The hydrocarbon polymer lies close to the right hand corner. Sputtering techniques produce graphite-like a-C (GAC) with a significant sp^2 content. However, to distinguish it from a-C with high sp^3 content, tetrahedral a-C (TAC) was also introduced. Using different plasma enhanced techniques, some films with large amounts of hydrogen can be produced, such as hydrogenated polymer-like a-C (a-C:H). The properties of a-C are strongly related to the amount sp^3 and sp^2 bonding within the material. The sp^3 bonding provides unique mechanical properties associated with diamond itself, such as high hardness, chemical inertness and wide bandgap. However, the electrical properties of a-C are strongly provided by its sp^2 content. The amount of sp^2 concentration and the size of the sp^2 clusters control the electronic structure of the material.

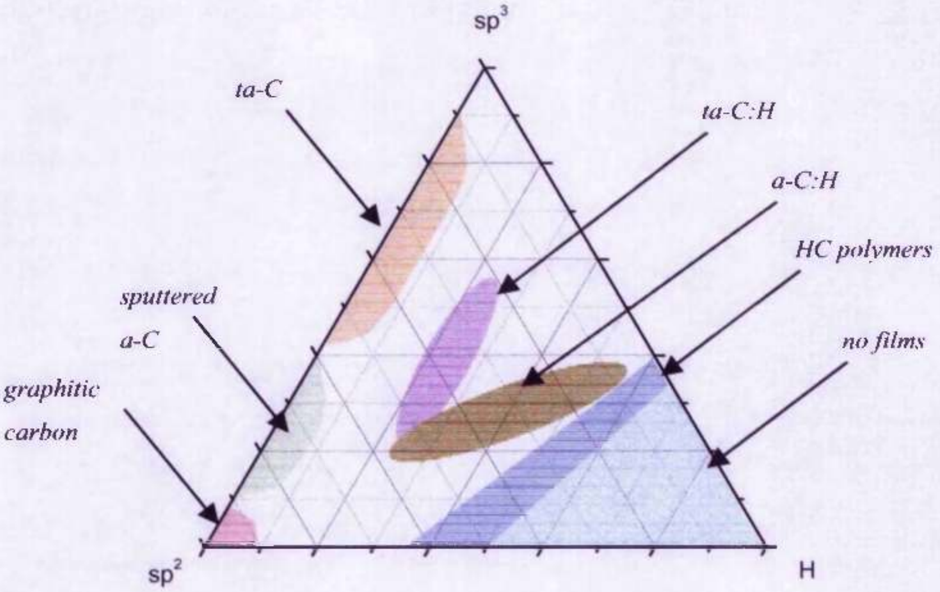

Figure 2-3: Ternary phase diagram of amorphous carbon.

2.2 Field emission mechanism

Electron field emission is the extraction of electrons from a semiconductor or metal through a vacuum barrier. It differs from thermionic emission in that the electrons tunnel through the vacuum barrier rather than surmounting it. In general, as the electric field increases, the barrier becomes narrower thus increasing the probability of electrons tunnelling through the barrier. The emission process is mainly dependent on the workfunction of the material, field enhancement and the applied electric field.

2.2.1 Fowler-Nordheim Theory

The quantum mechanical theory for field emission is given by the Fowler-Nordheim model. Emission of electrons occurs by a tunnelling process through a vacuum barrier and typically a local field of 2000-3000 V/μm is required. The quantum mechanical theory of field emission was first described by R. H. Fowler and L. Nordheim in 1928 [4] and is based on the free-electron theory of metals. The Fowler-Nordheim (F-N) theory describes the potential energy of an electron on the vacuum side of the metal-vacuum interface approximated by $E_F + \phi - (e^2/4x) - (eFx)$, where the four important terms are (in order) the Fermi energy, the workfunction, the classical image potential and the potential due to an external electric field respectively. e is the electronic charge, x is the distance from the metal surface and F is the local field. Figure 2-4 illustrates the band diagram of a metal emitter under the influence of an applied electric field.

The F-N theory leads to a simplified equation that describes the emission current and electric field in terms of the work function of metal as;

$$J = \frac{AF^2}{\phi}\exp\left(-\frac{B\phi^{3/2}}{F}\right) \qquad \textit{Equation 2-1}$$

where,

J is the current density (A/cm^2)

F is the local electric field (V/cm)

ϕ is the workfunction of the metal (eV)

$A = 1.54 \times 10^{-6}$ and $B = 6.87 \times 10^7$ are constant

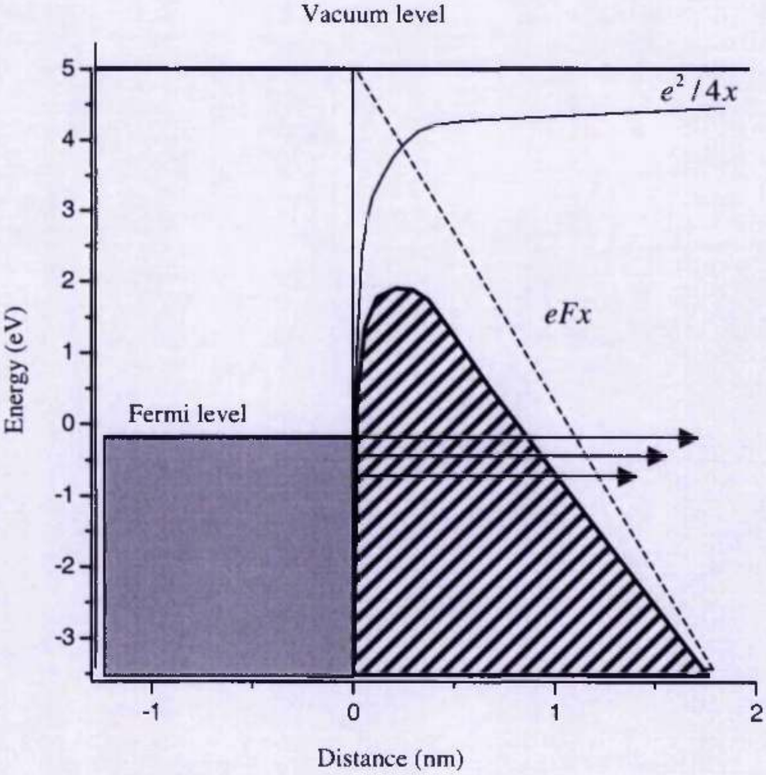

Figure 2-4: Band diagram of a metal-vacuum interface.

The expression explains that the emission of electrons does not require electrons to possess enough energy to surmount the vacuum potential barrier. Instead, because the electron's wave function is spread out in space, there exists a finite probability that the electron can tunnel through the barrier and be emitted into the vacuum. F-N theory is derived from the Fermi-Dirac statistics to determine the energy distribution of electrons striking a metal surface and then resolved for the Schrödinger equation to calculate the amount of electrons tunnelling through the barrier at that given energy. The emission current is then calculated by the integration of the product of both functions over all energies. Therefore, the emission current is dependent on the effective barrier, ϕ and the local electric field, F.

The F-N theory expression for the potential "seen" by an electron escaping from a metal is valid for flat and clean metal surfaces. However, to reduce the required applied electric field for electron emission, atomically sharp metal structures like the Spindt tips [5] are required to create electric field crowding effect. This intensification of electric field at pointed structures requires changes to the F-N equation to accommodate a field enhancement factor, β. The local field is now a product of β and the applied electric field (E). ($F = \beta E$ and $\beta \geq 1$). The enhancement factor can be estimated using a simple electrostatic model with some simplification [6,7].

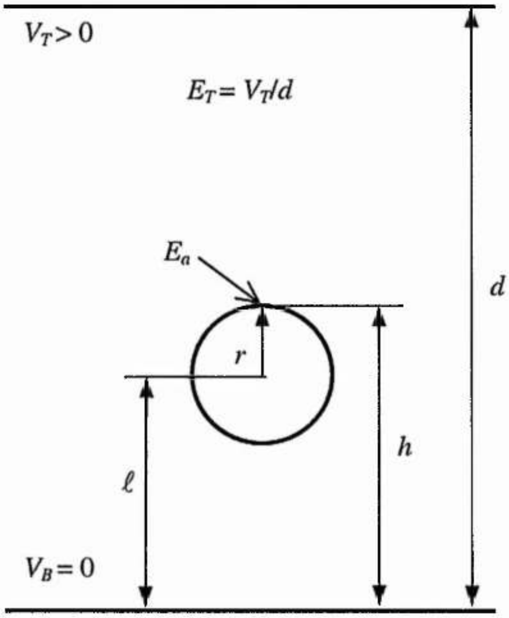

Figure 2-5: Floating sphere field emitter model.

Assuming that a sphere is floating between two infinite parallel planes, the potential of the bottom electrode (V_B) is equal to zero and the potential at the top electrode (V_T) is greater than zero. The sphere has a radius (r), height (h) and $\ell = h - r$ as illustrated in Figure 2-5. The distance (d) between the two electrodes is assumed to be much greater than h. Therefore, the above model can be solved mathematically using two main components of the charge distribution:

1) The dipole strength at the centre of the sphere is given by $p = 4\pi\varepsilon_0 r^3 E_T$
2) A uniform charge distribution of density $\varepsilon_0 E_T$ on the electrode.

where, ε_0 is the permittivity of free space and E_T is the microscopic field between the electrodes.

The field enhancement factor (β) on the apex of the sphere can be calculated using the following:

$$\begin{aligned}\beta &= E_a / E_T = (E_T + E_0 + E_Q + E_{im}) / E_T \\ &\approx 3.5 + \ell / r\end{aligned}$$ *Equation 2-2*

Where, the apex field (E_a) is the sum of E_T, the electric field at the centre of the sphere (E_0), the field contribution (F_Q) due to a charge Q and the field contribution (F_{im}) due to an image charge Q_{im}. The following equations give the meaning of each term:

$$E_0 = 2E_T$$

Equation 2-3

$$\begin{aligned} E_Q &= Q/4\pi\varepsilon_0 r^2 = [2\ell^2/r(2\ell - r)]E_T \\ &\approx \left[\frac{\ell}{r} + \frac{1}{2} + \frac{1}{8}\left(\frac{r}{\ell}\right)\right]E_T \end{aligned}$$

Equation 2-4

$$\begin{aligned} E_{im} &= -Q/4\pi\varepsilon_0(2\ell + r)^2 \\ &\approx \left[-\frac{1}{4}\left(\frac{r}{\ell}\right)\right]E_T \end{aligned}$$

Equation 2-5

However, it is commonly to see $\beta = h/r$ quoted in the literature. In the case of a carbon nanotube emitter, the application of 10 V/μm on an emitter of h = 1 μm and r = 5 nm (a typical dimension of a multi-walled carbon nanotube) will results in approximately a local field of 2000 V/μm on the apex of the tube.

To analyse the field emission data, it is common to rearrange the F-N equation into;

$$\ln\left(\frac{I}{E^2}\right) = \left[\ln\left(\frac{A\alpha\beta^2}{\phi}\right)\right] + \left[\left(\frac{-B\phi^{3/2}}{\beta}\right)\left(\frac{1}{E}\right)\right]$$

Equation 2-6

Examples of the curves from the above equation are shown in Figure 2-6, which compares the field emission from different transition metal carbides that are operated in identical conditions in an ultra-high vacuum field electron microscope. [8] The linear nature of these curves suggests the tunnelling process dominates the electron emission. In principle, the slope in each case should be proportional to ($\phi^{3/2}/\beta$). Therefore, with the workfunction of the material known, the enhancement factor can be extracted. The y-intercept from the curve will be proportional to [ln ($A\alpha\beta^2/\phi$)] from which the emission area (α) can be estimated.

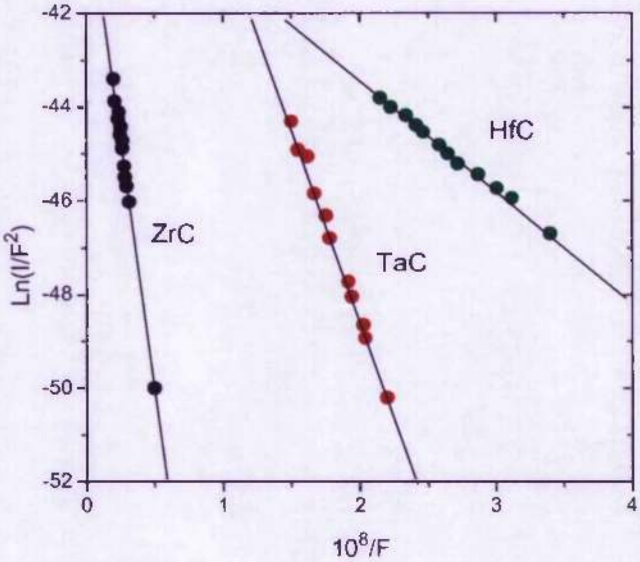

Figure 2-6: Fowler-Nordheim plots of field emission from HfC, TaC, and ZrC. The workfunction ordering of these three carbides, lower for shallower slope, has been verified by thermionic workfunction measurements. Data reproduced from Mackie *et al.* [8].

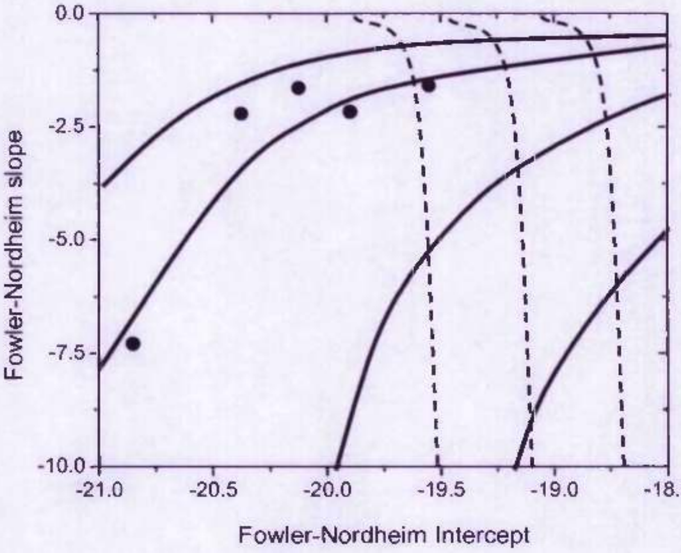

Figure 2-7: Fowler-Nordheim slope vs. intercepts plot. The solid line and dashed line corresponds to a family of curves with constant β and ϕ respectively. Data reproduced from Mackie *et al.* [8].

Thus, for any combination of ϕ, α and β, the slope and y-intercept from the F-N plot can be extracted. Figure 2-7 illustrates a family of curves corresponding to constant ϕ (dashed lines) and a family of curves corresponding to constant β (solid lines). Therefore, the F-N slope and

F-N y-intercept (S-K F-N) plot will be able to determine the corresponding variations of a series of different measurements. Note that the solid circles in Figure 2-7 correspond to a series of data that maintain a constant β while the F-N intercept varies. This suggests that either the workfunction or the emission area is changing. The variation in the data points also suggests that the current density is changing.

2.2.2 Hot electron induced emission

Field emission from carbon thin films has been observed at relatively low electric fields. Although the emission characteristics generally follow the F-N type curve, the barrier height extracted from the F-N plot usually results in an unrealistic value. Indeed, barrier heights as low as 0.05 eV have been observed by these analyses. The actual barrier heights from these films are in the range of 2.5-4 eV based on contact potential measurements. Therefore, it has been proposed that for certain types of films, the real cathode for emission lies at the back contact that is controlled by the substrate. In this model, the carbon film acts as a space charge interlayer, where sufficient field penetration results in a significant band bending from the vacuum surface, right to the substrate. This result in hot electrons induced through the back contact by surmounting the heterojunction formed between the silicon substrate and semiconducting carbon film. Interestingly, carbon films that exhibit this phenomenon usually have film thickness dependence, where an optimum thickness will results in the lowest threshold field.

Bayliss and Latham [9] first proposed a hot electron emission model based on the electron emission from metal-insulator-vacuum micro emission regimes. Amaratunga and Silva [10] later refined this model using a semiconductor model with nitrogenated a-C:H films and n^{++}-Si. These hot electrons are assumed to be generated by a penetrating electric field within the "interlayer", because of band bending. Hot electrons are accelerated through the "interlayer" where they gain energy from the field and exit into vacuum by virtue of the band bending at this back heterojunction. Figure 2-8 shows the possible band diagram of a space charge induced hot electron emission process.

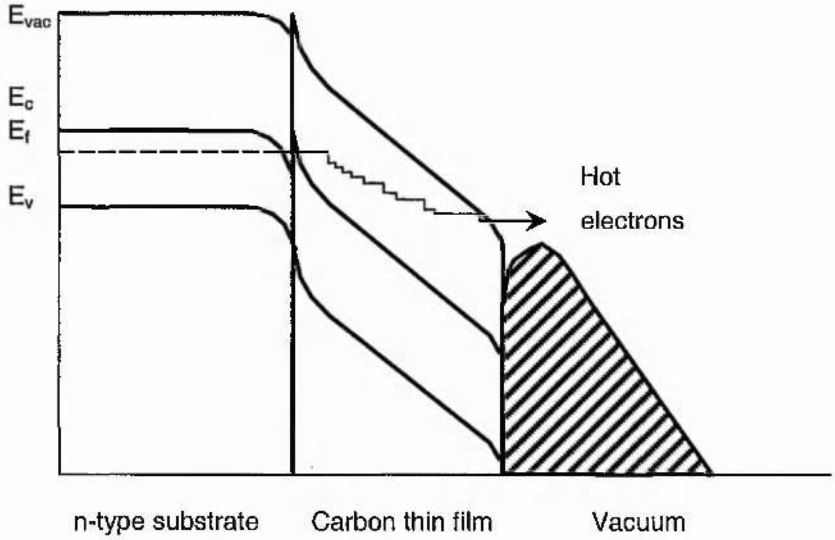

Figure 2-8: Band diagram of a space charge induced hot electron model.

2.2.3 Negative Electron Affinity

When the (111) surface of diamond is terminated with hydrogen, it is well known that the surface can possess negative electron affinity (NEA). [11] Electrons at the conduction band minimum can then escape from the diamond without an energy barrier at the surface other than from surface dipoles. This allows for electron field emission at very low fields since electrons only need to overcome surface barriers such as dipoles. In the early studies, there has been great effort to understand and characterise this special property of diamond and to focus on low electron affinity materials. As low threshold electron emission is observed from graphitic materials and carbon nanotubes, NEA is not the main pre-requisite for field emission in these carbon based cathodes. Figure 2-9 shows the energy level of a positive and negative electron affinity. The main limitation of using diamond as an electron source is that diamond is a wide band gap material (5.5 eV). There is limited electron supply at the conduction band which means that electrons have to be injected over a large barrier (4 eV) from the back contact. [12] Instead, nano-crystalline diamond films are found to be better field emitters than diamond. The grain boundary within the nano-crystalline diamond creates a conducting path that allows electrons to be transported to the vacuum front surface. [13]

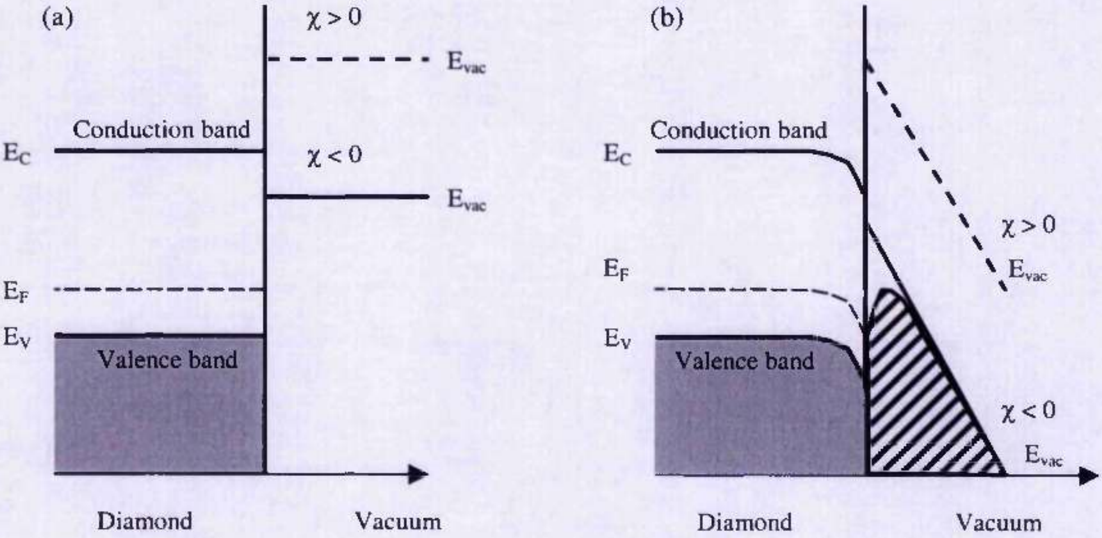

Figure 2-9: Band diagram of a NEA and PEA energy level, (a) represent the diamond surface without electric field and (b) under the influences of an applied field.

2.2.4 Field Enhancement from Carbon Structures

Field emission from carbon-based materials can be dependent on the carbon bond hybridisation. Especially field emission properties of diamond-like amorphous carbon (DAC) and tetrahedral amorphous carbon (TAC) have been shown experimentally to have a direct relationship between the amount of sp^3 and sp^2 concentration. In case of the influence of the sp^2 bonding, the clustering of the sp^2 phase has played an important role in terms of low emission threshold fields. Earlier reports have shown the field emission threshold field to be dependent on the sp^3 concentration. However, later work realised that high sp^3 concentration itself is not sufficient for this but the variation of the sp^3 and sp^2 concentration plus the sp^2 cluster size may contribute to the origin of low threshold field emission in DAC [14] and TAC [15,16].

In the case of nano-crystalline diamond, Robertson[17] proposed field enhancement at the surface because external field lines focus on charges trapped at the grain boundary defects. Ilie *et al.* [16] estimated the optimum size for sp^2 cluster size in ta-C to be 1-10 nm determined from Raman spectroscopy. The sp^2 phase can contribute to the field enhancement and is a result of a conductive sp^2 cluster around the resistive sp^3 matrix.

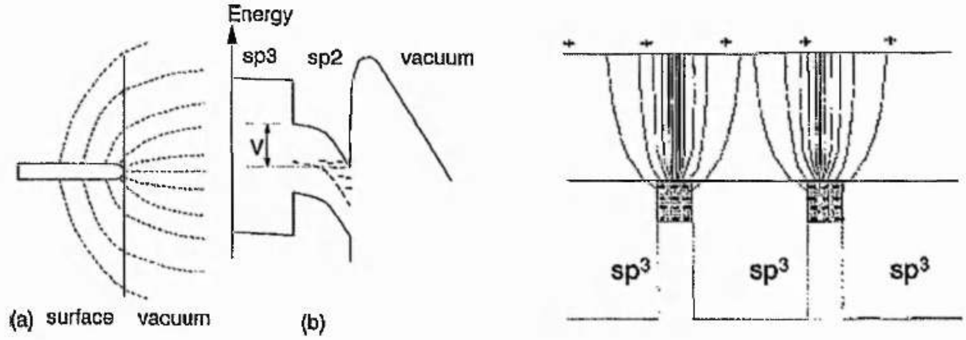

Figure 2-10: Band diagram with a sp^2 cluster and vacuum interface, reproduced from Ilie *et al.* [15,16].

It is proposed that the field is concentrated around high-aspect ratio filamental nanostructures enhancing the electrons penetrating the barrier at the vacuum. The band diagram in figure 2-10 is for field emission from a filament-type sp^2 cluster perpendicular to the film/vacuum interface, creating a negative space charge in the film. Once more, space charge arguments [10] are needed in order for the electrons to gain high enough energy to escape from the amorphous carbon. However, the amount of field penetration into the TAC carbon film does not go below a few nanometres due the field line termination at the more conductive sp^2 clusters. Therefore, a filamentary explanation for the field enhancement can be limited in the case of films with high sp^2 concentrations. Carey *et al.* [18] explained the enhancement from sp^2 phases based on a proximity effect as a result of two conductive spheres surrounded by a more insulating dielectric. In this work, it was proposed that the conductive sp^2 clusters found near the film surfaces dominate emission giving rise to high "internal" or "bulk" field enhancement. By having the graphitic clusters in close proximity and surrounded by the insulating sp^3 matrix, this electrostatic effect can generate high localised field concentration. Using the calculation from Chaumet and Dufour [19], two spheres with the conductivity of gold can generate a field enhancement of up to 400. Having more than 2 clusters together can also generate further field enhancement. Figure 2-11 shows the field distribution and calculations of the field enhancement as proposed by Chaumet and Dufour [19]. It is also worth noting that, with increasing sp^2 concentration in the films better electric connectivity in the bulk of the thin film results. This will then allow electrons to replenish those being emitted.

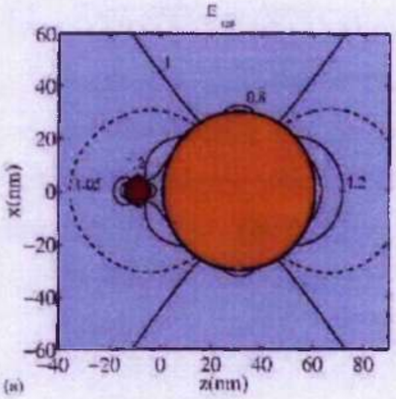

Separation (nm)	**Dielectrics ($\varepsilon_2 = 2\varepsilon_1$)**	**β in Conductors (Au)**
5	2.1	56
3	2.3	127
1	2.5	406

Figure 2-11: Field enhancement from two conductive spheres. Table shows the enhancement calculations (β) for different separation distance, reproduced from Chaumet and Dufour [19].

2.3 Field emission from carbon based material

Carbon-based materials are very attractive candidates to replace the present Spindt tip technology. Various types of carbon based materials such as diamond, tetrahedral amorphous carbon (TAC), diamond-like amorphous carbon (DAC), polymer-like amorphous carbon (PAC) and carbon nanotubes have been shown to exhibit field emission at low applied electric fields of the order less than 40 V/μm. This opens up the prospect of using thin film technology that could simplify the manufacturing process of cold cathodes. The advantages of carbon based materials also include the unique properties such as chemical inertness, rigid mechanical properties and resistance to contamination. Other possible applications of field emission also include microwave amplifier, cathodes for electron beam sources and x-ray sources. Figure 2-12 shows the gated structure of the different type field emitters.

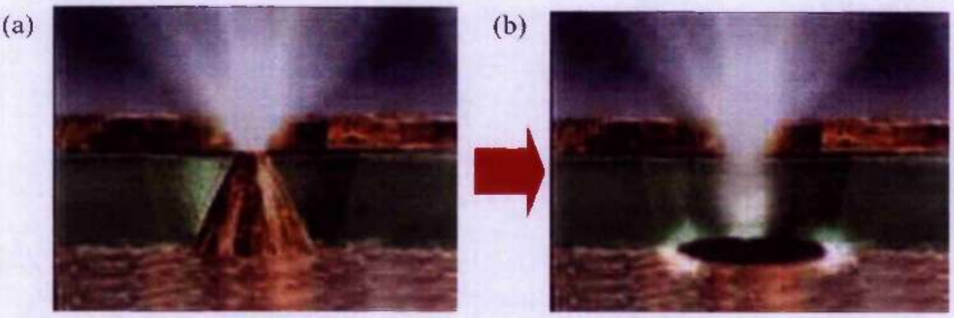

Figure 2-12: Field emission emitter using (a) Spindt tip technology and (b) thin films technology.

2.3.1 Tetrahedral Amorphous Carbon Films

The field emission properties of TAC are usually illustrated with the changes in deposition ion energy. By altering the ion energy during deposition, different fractions of sp^3/sp^2 concentrations and electronic properties can be achieved. The variation of threshold field is shown in Figure 2-13. The threshold field of TAC films is seen to be minimum at around 100 eV for the data Satyanarayana *et al.*[20] and Cheah *et al.*[21] and this was explained by the high sp^3 concentration present in the films deposited with the specified ion energies. It was proposed that the sp^3 region possesses much lower electron affinities as compared to the sp^2 region. Therefore, lower emission threshold fields could be obtained from the high sp^3 films. Figure 2-14 shows the comparison of the threshold field with sp^3 fraction (measured by EELS) for the TAC films. The alteration of the TAC films to achieve high sp^3 concentration was motivated by the low electron affinity of diamond. Therefore, TAC films with high sp^3 concentrations were thought to be ideal field emitters with low vacuum barriers at the front surface. However, laser ablated TAC films were observed with low sp^3 (high sp^2) concentrations and low emission threshold fields [22]. Carbon nanotubes that are high sp^2 containing material have also been reported to possess excellent field emission properties. This indicates that a high sp^3 concentration is no longer the pre-requisite for low field electron emission.

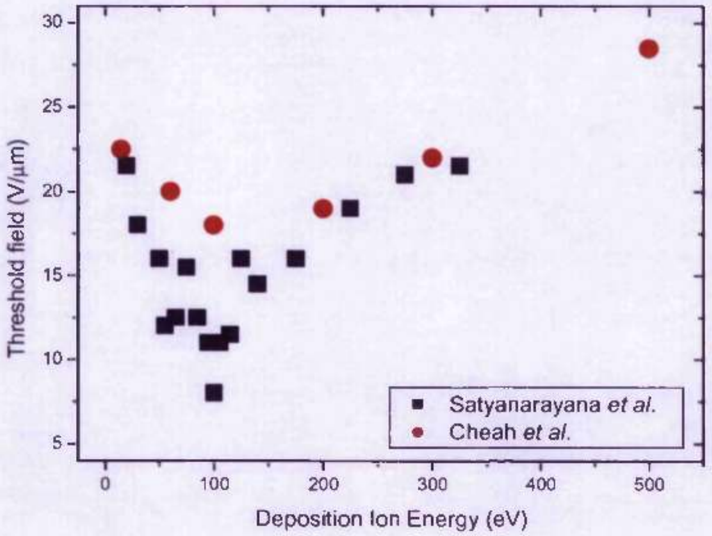

Figure 2-13: Variation of the threshold field of TAC films as a function of the deposition ion energy. Reproduced from Satyanarayana *et al.* [20] & Cheah *at al.* [21].

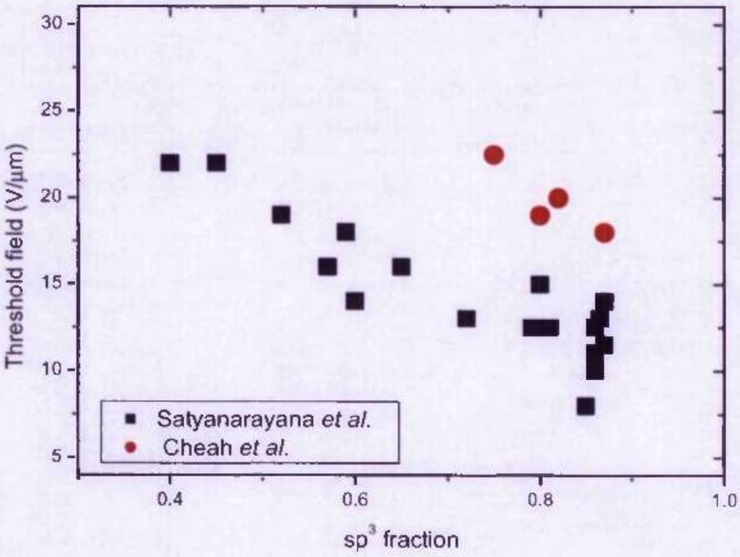

Figure 2-14: Variation of threshold field as a function of the sp^3 fraction. Data reproduced from Satyanarayana *et al.* [20] & Cheah *at al.* [21].

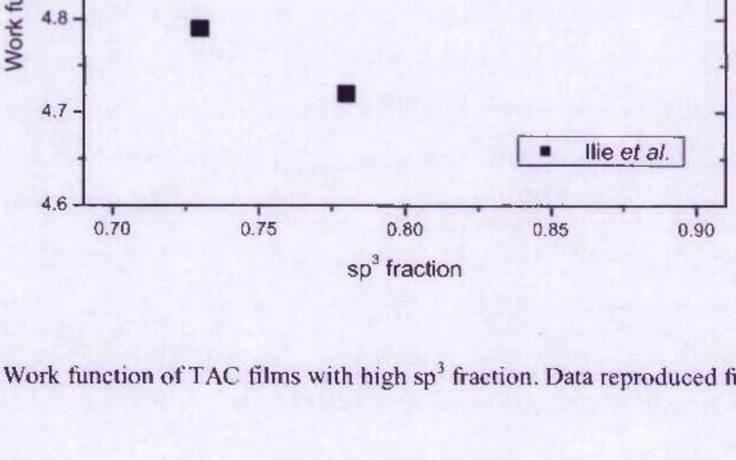

Figure 2-15: Work function of TAC films with high sp^3 fraction. Data reproduced from Ilie *et al.* [23].

Recently, data by Ilie *et al.* [23] shows that the work function measurements from these materials are in fact in the order of 4.7 to 5 eV which suggests that TAC films do not possess low electron affinity (~2.5 to 3 eV) and hence other mechanisms are responsible for the low emission threshold field. Figure 2-15 shows the TAC work function from Kevin probe measurements as a function of the sp^3 fraction. The high work function from highly sp^3 TAC films shows that the local field for electron emission is in the order of 1-5 x 10^3 V/μm.

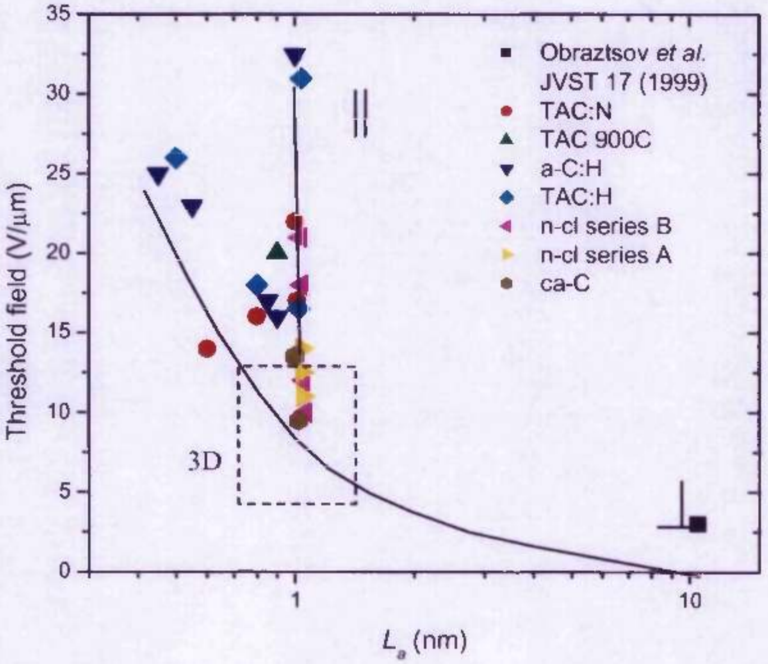

Figure 2-16: Emission threshold field as a function of the Raman in-plane correlation length L_a for various classes of carbon films. Data reproduced from Ilie *et al.* [16].

Ilie *et al.* [15,16] later suggests that the sp^2 clustering within the TAC films are more important that the sp^2 content which is based on field enhancement model proposed by Carey *et al.* [18] which gives high fields due to carbon's inhomogeneous nature. The study of the sp^2 microstructure using visible Raman spectroscopy shows the presence of a Raman *D* peak at ~1350 cm^{-1}, which is indicative that the sp^2 phase is clustering into aromatic rings. Relating the two carbon peaks in Raman of I(*D*)/I(*G*) to the in-plane correlation length (L_a), as discussed by Schwan *et al.* [24], the optimum cluster size is obtained. However, in the initial work by Ilie *et al.*[15], the optimum L_a was reported to be 0.2 nm which is too small to be considered as a sp^2 aromatic ring cluster. Ilie *et al.* later refine the argument that the optimum cluster size lies within range of 1-10 nm. [16] Figure 2-16 shows the variation of threshold field as a function of L_a. It can be seen that the material with a larger cluster size exhibit a lower threshold field. It was proposed that in order to obtain low threshold fields, the orientation of the sp^2 cluster needs to be perpendicular to the axis of the applied field. Also in Figure 2-16, for the film with the sp^2 clusters parallel to the axis of the applied field, the observed threshold field is much higher.

2.3.2 Diamond-like Amorphous Carbon

Diamond-like Amorphous Carbon (DAC) films are those with significant sp^3 bonding component which may contain hydrogen (a-C:H) or be hydrogen free. Good examples are those deposited on the driven electrode of an rf-PECVD system. Figure 2-17 shows the variation of threshold field and Tauc gap of a series of films deposited as a function of the negative self-bias. (Definition of Tauc gap and negative self-bias will be explained in the Chapter 3.3.1 and 3.1.2 respectively). The negative self-bias was developed across the plasma sheath in the range of 50 to 265 V, at a fixed chamber pressure of 200 mTorr.

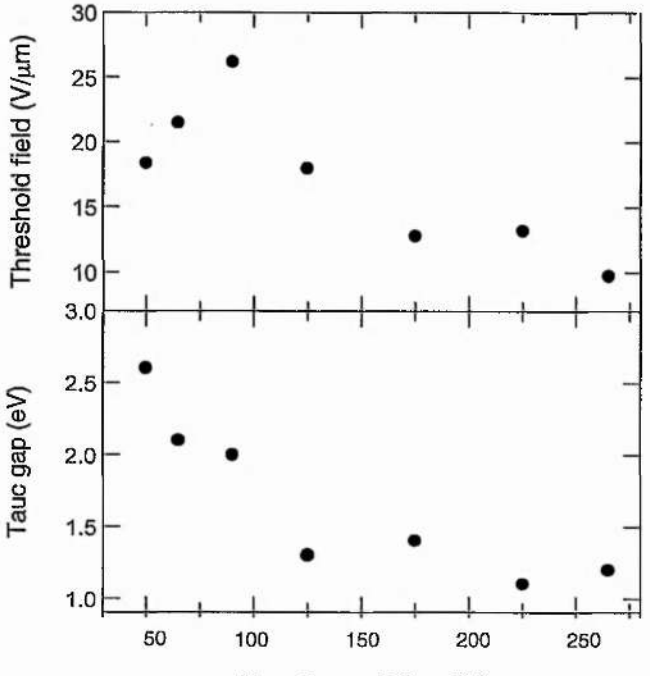

Figure 2-17: Variation of threshold field and Tauc gap as a function of the negative self-bias.

It can be seen in Figure 2-17 that there are two regimes in the field emission threshold field. Just before the negative self-bias of 100 V, the threshold fields rise from 18 to 27 V/μm and thereafter it falls to 8 V/μm at 256 V negative self-bias. The Tauc gap that is related to the sp^2 concentration shows that as the self-bias increases, the films get more graphitic. When the films become less diamond-like and more graphitic, the threshold field starts to decrease. The properties of polymeric amorphous carbon (PAC) films that are deposited at low negative self bias voltages (> 100 V) will be discussed in the next section.

2.3.3 Polymer-like Amorphous Carbon

The polymer-like amorphous carbon (PAC) films are usually associated with low defect densities in the bulk. In terms of field emission properties, a high initiation field is required before emission. Interestingly, these films are observed to have large field penetration where the back contact at the film substrate interface is important. Film thickness dependence was also observed during field emission. Shown in Figure 2-18 is the variation of threshold field as a function of film thickness for DAC (self-bias of –90 V and -256 V) and PAC film.

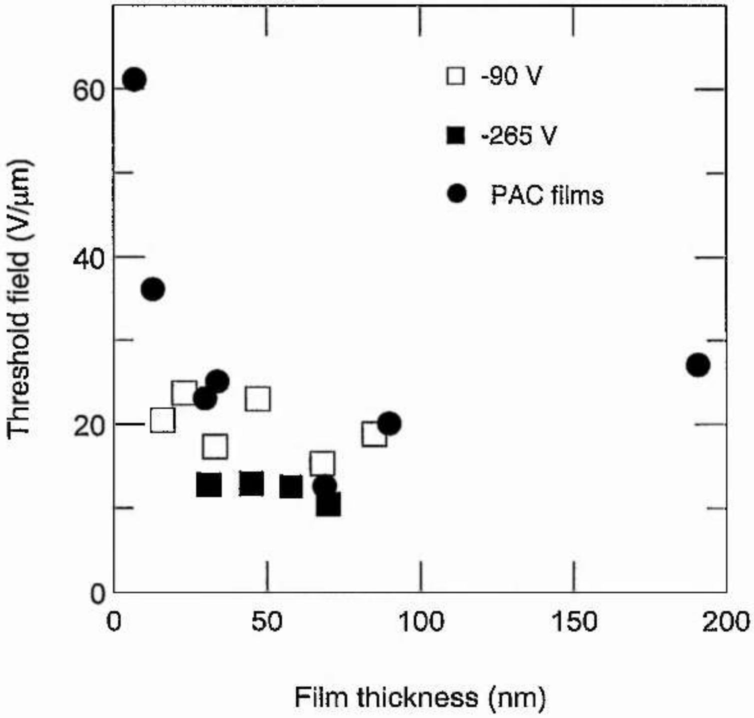

Figure 2-18: Variation of threshold field as a function of film thickness for films with self-bias of -90 V, -256 V and polymeric films. Data reproduced from Carey *et al.* [18].

The thickness dependence effect is only observed with the PAC with low defect density. Films deposited at high self-bias are usually more defective and the field penetration into the films is minimum. The mechanism proposed to explain the field emission properties of PAC are associated with the hot electron effects, induced by the large field penetration into the film resulting band bending at the back surface.[25] Basically, the solution to Poisson's equation for charge redistribution at the back heterojunction will give a higher electric field at this interface than the remaining bulk PAC film.

2.3.4 Graphite-like Amorphous Carbon

The graphite-like amorphous carbon (GAC) films are films with a high sp^2 concentration. There are a few publications showing field emission from these films with low threshold fields. These are usually nano-composites films with the nano size graphitic component embedded in the amorphous carbon matrix.

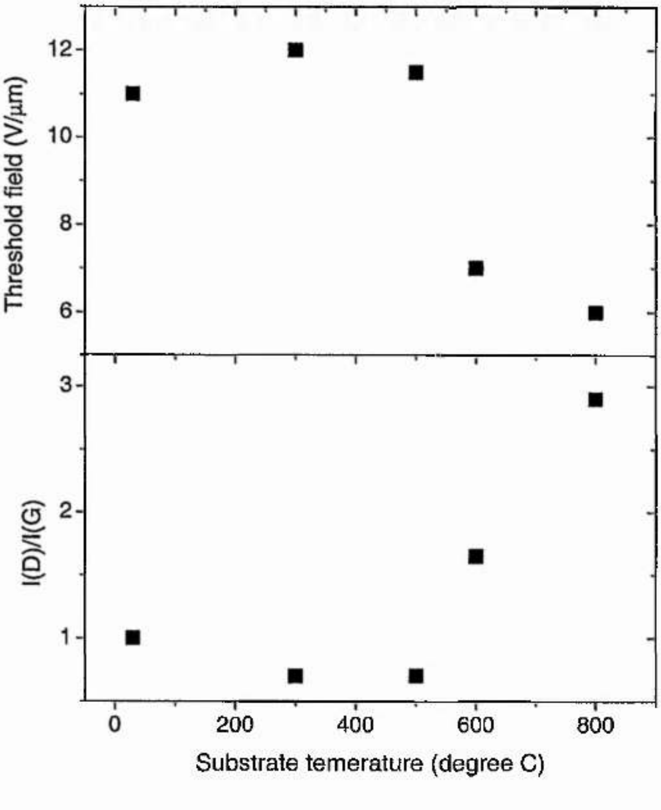

Figure 2-19: Variation of threshold field and I(D)/I(G) as a function of substrate deposition temperature. Data reproduced from Baek *et al.* [26].

One method to increase the graphitic component within amorphous carbon films is to alter the deposition. In the work by Baek *et al.* [26] the GAC films are deposited in rf Plasma-enhanced CVD (rf-PECVD) with different substrate temperatures. The increase in substrate temperature increases the graphitic concentration measured by Raman spectroscopy. Figure 2-19 shows the field emission threshold field and I(D)/I(G) intensity ratio (Raman measurement) as a function of the substrate temperature. It can be seen that the increase in temperature results in an increase in I(D)/I(G) and reduction of threshold field from 12 to 6 V/μm. This result is in agreement with the analysis from Carey *et al.* [18] and Ilie *et al.* [16] where the sp^2 concentration and size determines the threshold field.

In the work by Obraztsov *et al.*, [27,28] the GAC films were deposited by a chemical vapour deposition technique. These comprise of graphite platelets oriented predominantly by the graphite basal planes along the substrate surface. Emission threshold fields as low as 1.5 V/μm have been reported. [28] Obraztsov *et al.* proposed an emission based on the inhomogenity of the GAC film [28] as shown in Figure 2-20. It was proposed that the diamond-like region possess low electron affinity, and that this allows the diamond-like material at the front surface to form a lower barrier for electron to tunnel through from the graphite-like regions. However, for this model to be valid, low electron affinity from these CVD carbon films need to be verified.

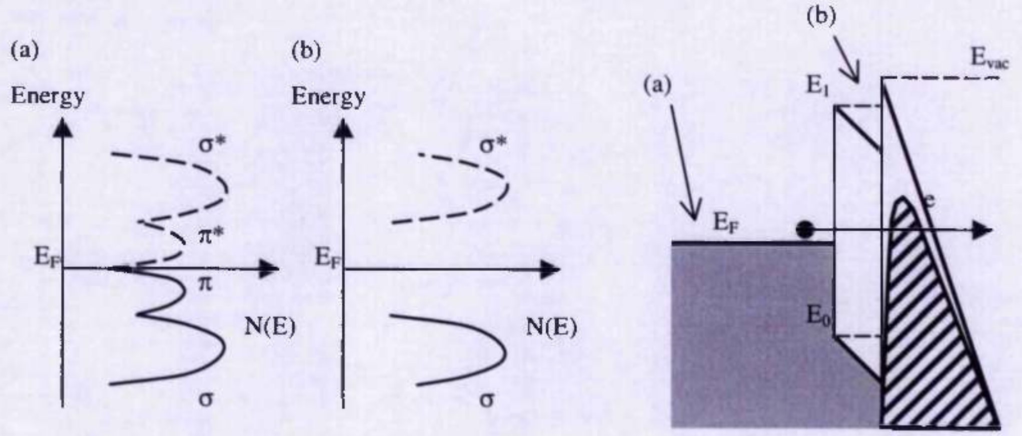

Figure 2-20: Schematic diagrams of DOS for bulk graphite (a) and for carbon atoms located at the surface of the film (b). Schematic representation of the field emission mechanism, reproduced from Obraztsov *et al.* [27,28].

This model is very similar to the "bulk interlayer" model [10]. There are also reports that try to increase the sp^2 concentration within the GAC films by producing metal-containing amorphous composite films. In the work by Chen *et al.* [29] nickel was incorporated into ta-C films. Later Lau *et al.* [30] shows that Co incorporated within films reduces the threshold field from 7 V/μm for ta-C to 1 V/μm from a-C:Co films.

However, in spite of the high sp^2 concentration observed from these GAC films resulting in a low threshold field, there are possibilities that these nanostructed films contain carbon nanotubes that may be the origin of the low threshold fields.

2.3.5 Carbon Nanotubes

Field emission from carbon nanotubes (CNT) has attracted attention among other carbon-based materials. Indeed, low threshold fields and high current densities have been observed from CNTs. They are graphitic threads with a radius of a few tenths of a nanometre and lengths up to a few microns. They are considered as one of the most promising field emitters and very easy to produce in large quantities. To understand the field emission properties of CNTs, one can consider three fundamental types of tubes. [31] They are shown in figure 2-21, (a) capped Multi-walled CNT (MWNT) (b) open cap MWNT, and (c) bundles of single-walled CNTs (SWNTs).

Figure 2-21: TEM images of (a) MWNT with a capped end, (b) MWNT with an open end, (c) bundle of purified SWNTs. Data reproduced from Saito *et al.* [31].

The current versus applied voltage characteristics for the three kinds of nanotubes are shown in Figure 2-22 together with the F-N plots. It can be seen that the structure of these nanotubes affects the field emission characteristics. In the case of the open end MWNT, lower applied voltages are required for electron emission. In contrast, a much higher voltage is required for the capped MWNT. The summary of the field emission properties is shown in Table 2-1.

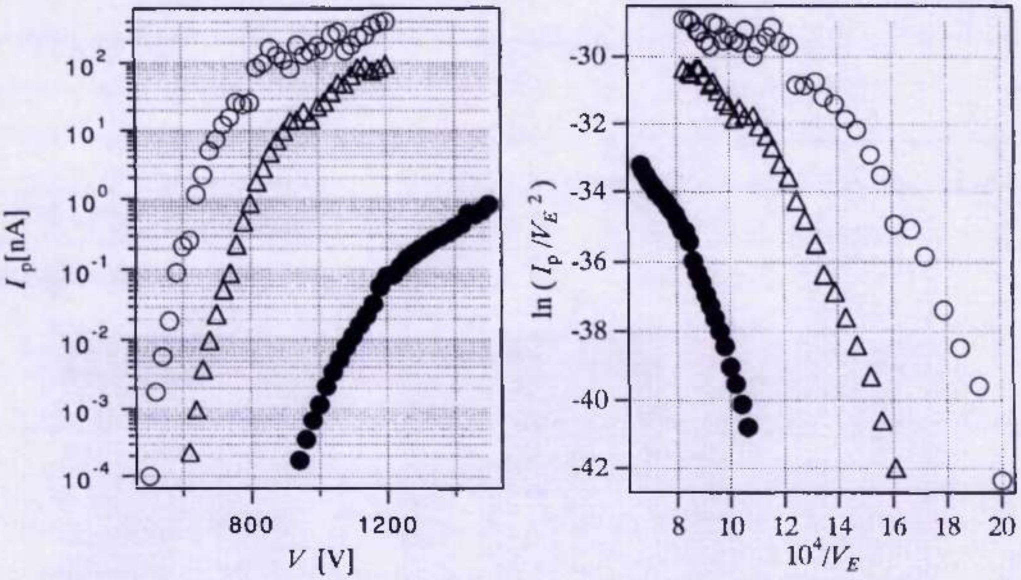

Figure 2-22: Current vs. Voltage characteristics and (b) F-N plots for a capped (●), and open MWNT (○), and bundle of SWNTs (△). Data reproduced from Saito *et al.* [31].

Carbon nanotubes	Threshold Voltage *	Saturation Current (nA)	Maximum current Density (x 10^6 A/cm^2)
Capped MWNT	900-1000	0.5-3	~1
Open MWNT	500-600	400-900	~100
SWNTs	600-700	50-300	~10

* Threshold voltages represent tip voltages at which currents measured by the probe hole exceed 0.1 pA. The emitter and electrode distance was kept at 60 mm. Since emission current was measured by the 1 mm probe hole, the properties come from single tubes for MWNTs and from one bundle for SWNTs.

Table 2-1: Summary of the three kinds of nanotubes. Data reproduced from Saito *et al.* [31].

It can be seen that the open MWNT have very similar threshold voltages as the bundle of SWNTs, this suggests that the field emission properties of these three types of nanotubes are strongly dependent on the tip structure. The linear curves obtained from the F-N plots also suggest that the emission mechanism is mainly due to tunnelling of electrons through the vacuum barrier which is considered a front surface dominated emission process. It is important to note that the electronic states in these nanotubes can also vary at the apex (from the bulk) of the tube, as shown by STM studies [32].

The other important factor to consider in the emission properties of CNTs is the effect of electric field screening. This is the electrostatic effects causing the electric field to be screened away from the neighbouring nanotubes. The work from Teo *et al.* [33] has compared the effects of field screening from samples with different CNT densities. The SEM images in Figure 2-23 shows three different types of CNT films, (a) dense film, (b) sparse films and (c) arrays of CNT.

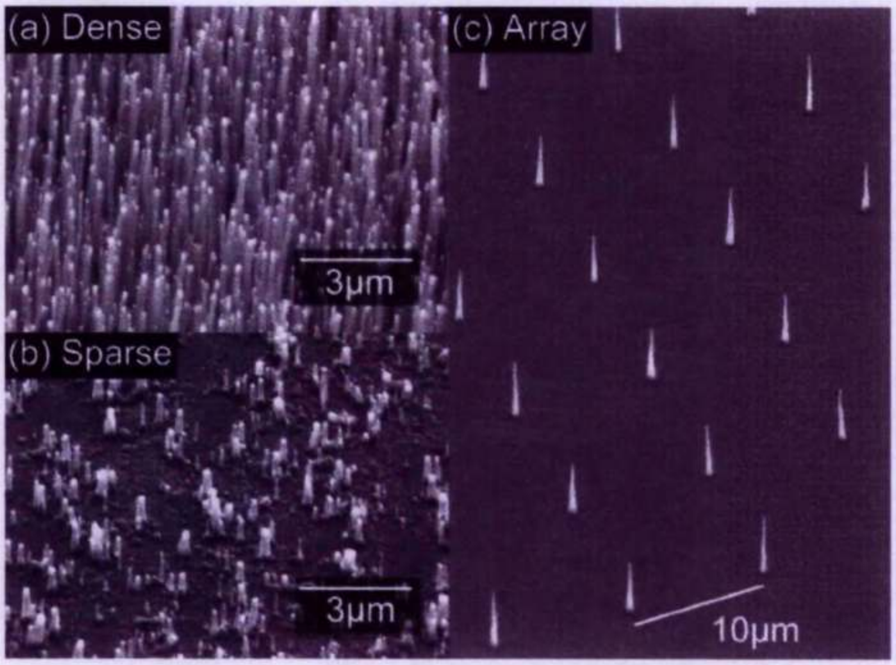

Figure 2-23: SEM images of (a) dense, (b) sparse and (c) arrays of CNT, reproduced from Teo *et al.* [33].

It can be seen in Figure 2-24 that the variation of the emission current as a function of the applied field varies with the different types of film. The dense film with CNT located close together exhibit the highest threshold field, while the lowest threshold fields are found for the arrays of CNT film. This result suggests that the separation distance of the CNTs is very important in the field emission properties. Ideally, the separation distance would be twice the distance of the height of the CNT [34].

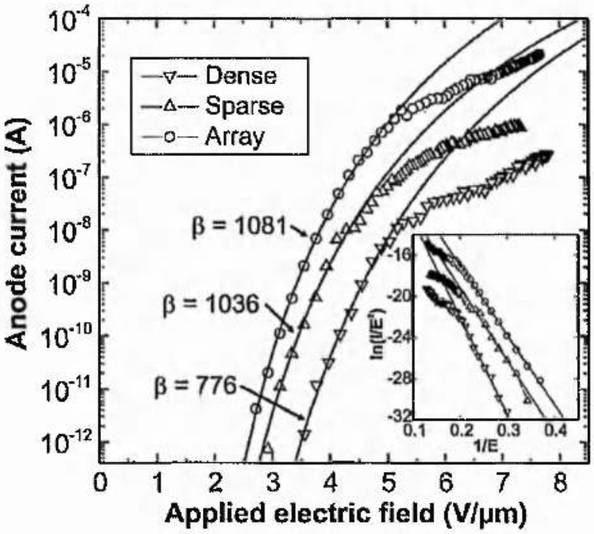

Figure 2-24: Current vs. applied electric field for a) dense, (b) sparse and (c) arrays of CNT , reproduced from Teo *et al.* [33].

Emitter	E_{to} (V/μm)	E_{thr} (V/μm)	J_{max} (A/cm^2)	Remarks	Ref.
MWNT	n.a.	~15	10	Very dense film	35
Arc MWNT	n.a.	20	0.1		36
Arc MWNT	7.5	10	0.4	Open tubes in epoxy	37
SWNT	n.a.	4-7	4		38
CVD MWNT	4.8	6.5	0.1-1		39
Graphitic fibres	2.1	n.a.	0.2		40

Table 2-2: Comparison of different types of CNT. E_{to} and E_{thr} are the turn-on and threshold fields needed to produce a current density of 10 μA/cm^2 and 10 mA/cm^2 respectively. J_{max} is the maximum current density obtained without the destruction of the emitter.

A short review of the reported field emission characteristics from nanotubes is shown in Table 2-2. In general, the observed threshold fields are comparatively lower than for other forms of carbon based materials. The threshold fields are as low as 1 V/µm (for a current density of 10 µA/cm^2) and turn-on fields are around 5 V/µm (for a current density of 10 mA/cm^2). Typically, CNTs are capable of producing high current density up to a few A/cm^2 at applied fields below 10 V/µm. Table 2-2 also reveals that there are no conclusive influences on the synthesis techniques and field emission properties. Two important influences on the field emission properties are, 1) the intrinsic structural and chemical properties of the individual CNT (such as the diameter and surface treatment of the tubes, and the open or closed cap at the apex of the tube). 2) the density and orientation of the tubes.

2.4 Summary

In summary, we have looked at the field emission mechanism and properties from different types of carbon-based materials. Indeed, there are large differences in the synthesis of the material and their field emission mechanisms. Despite several studies in the literature trying to unify the field emission mechanism from these carbon based materials, there are still areas in which need better understanding. The field emission process can be summarised from Figure 2-25.

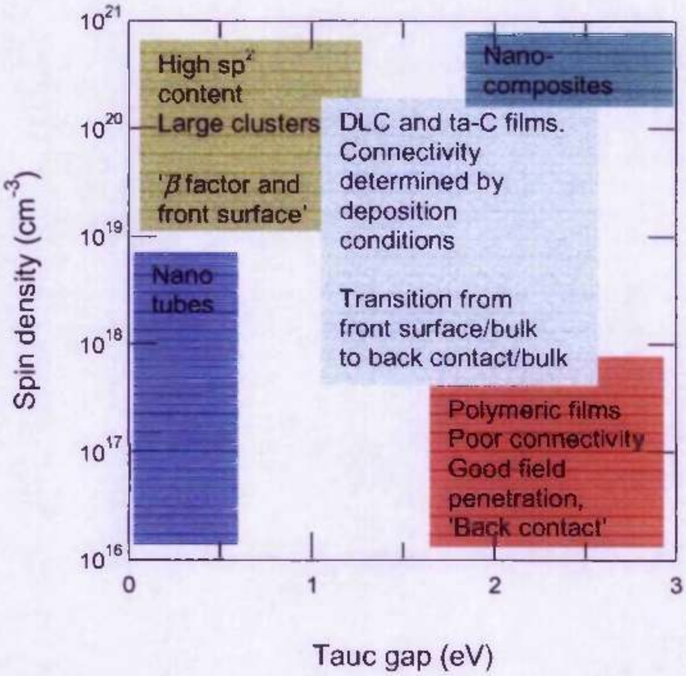

Figure 2-25: Variation of spin density as a function of carbon based material with different Tauc gap.

Where the spin density measured by electron paramagnetic resonance measurements is used to probe the amount of field penetrations into the material and the Tauc gap indicates the graphitic content. In this case, high spin density indicates that there is low field penetration and low Tauc gap indicates high sp^2 concentration. It can be summarised that the field emission mechanism in carbon-based materials are controlled by the type of composite within the films especially the types of hybridising. Therefore, resulting in the front or back contact type of emission. It is also important to note that there are discrepancies from the different proposed models and there is no strong agreement in the possible model that can be universally applied.

We have also discussed the excellence field emission properties from CNT, indeed, CNT have shown low threshold fields and high current density from many authors. However, there are needs to control the field emission properties in the two areas discussed, the structural properties and the density and orientation of the CNT films.

Chapter 3

3 Experimental Techniques

In this section, the growth of amorphous carbon thin films and preparation of carbon nanotube-polymer composite films will be described.

3.1 Thin film deposition

Two types of thin film deposition techniques will be discussed in this section. Amorphous carbon (a-C) thin films are deposited using the Ion Beam Assisted Deposition technique and hydrogenated amorphous carbon (a-C:H) thin films deposited using a radio-frequency Plasma Enhanced Chemical Vapour Deposition technique.

3.1.1 Ion beam assisted deposition technique

The a-C films were deposited by an Ion Beam Assisted Deposition (IBAD) technique using two 3 cm diameter Kauffman ion sources. Shown schematically in Figure 3-1, IBAD is a thin film vacuum deposition process that combines conventional evaporative deposition with low energy ion bombardment. Prior to deposition of the film, the substrate can be ion sputtered to clean and to improve adhesion of the film. During deposition, it can be ion bombarded to alter the film microstructure.

A high-purity graphite target (99.99%) is sputtered by different noble gas ions at a beam voltage of 1500 V, using a total beam current of 90 mA. Films were prepared separately with Neon, Argon and Krypton gases introduced in both Kauffman sources. Simultaneously, a 75 V assisting beam (ion bombardment) containing the ions, bombards the growing film. This enabled independent control of the deposition species and the ion flux used to transfer momentum to the growing film surface. The substrate holder allows the substrate temperature to be heated up to 1000 °C. This removable holder also allows easy transfer of the samples to ultraviolet/x-ray photoelectron spectroscopy (UPS/XPS) analysis systems.

All films were prepared at 150 °C applying an ion beam assisting energy in the range of 0 to 800 eV.

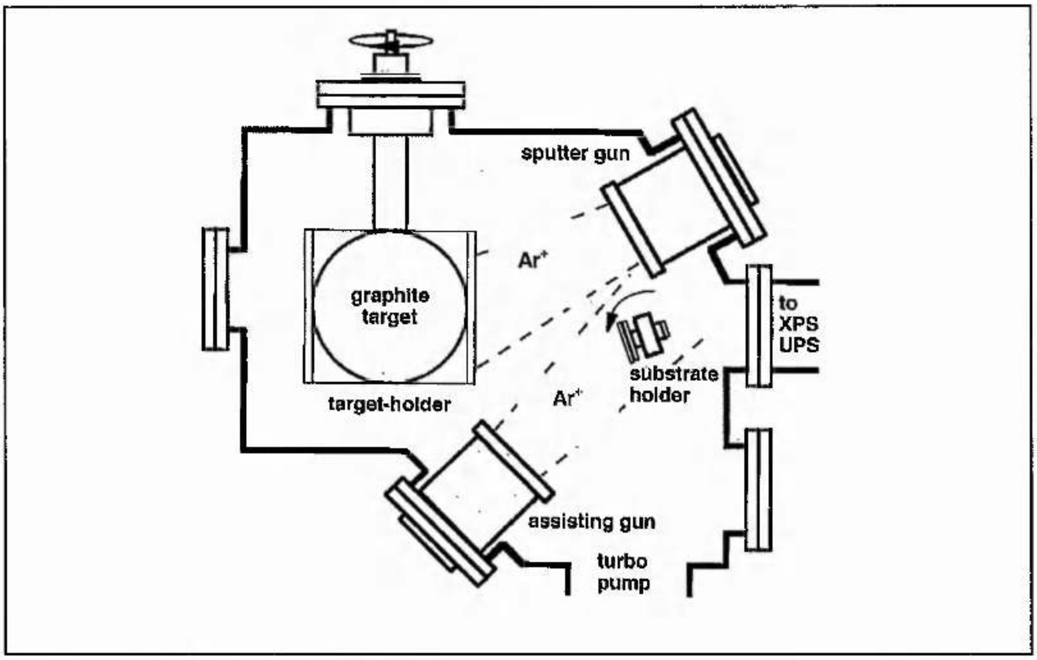

Figure 3-1: Schematic view of the IBAD chamber equipped with two 3 cm Kaufman ion sources, a graphite target and a heated substrate holder. In this setup, Ar is used in both ion sources.

A probe biased at –30 V was placed at the position of the substrate to measure the assisting ion intensity arriving at the sample. The carbon flux was calculated from the deposition rate when no assisting beam is present. The total deposition pressure was varied depending on the gas mixture at 2.5 x 10^{-2} to 1.2 x 10^{-1} Pa. The base pressure of the chamber was pumped by a 450 *l*/s turbomolecular pump at about 2 x 10^{-5} Pa.

Ion bombardment is the key factor controlling film properties in the IBAD process. As in ion implantation, the ions impart substantial energy to the thin film/substrate interface. This achieves the benefits of localised heating (which generally provides a denser, more uniform film) without significantly heating the substrate material and degrading bulk properties. The ions also interact with the growing thin film, driving them into the substrate and producing a graded material interface, which enhances adhesion.

These films have been prepared by Dr. R.G. Lacerda in the Universidade Estadual de Campinas, Brazil.

3.1.2 Radio-frequency plasma enhanced chemical vapour deposition technique

The a-C:H films are grown using an industrial standard Plasma Technology DP800 radio-frequency plasma enhanced chemical vapour deposition (rf-PECVD) system. The schematic view of the system is shown in Figure 3-2. The radio frequency-glow discharge PECVD deposition technique allows low process temperatures, between 30 °C and 250 °C, and is therefore compatible with a large variety of substrates. In this work, films are deposited at room temperature on silicon and Corning 7059 substrates for electrical and optical measurements. The deposition pressure is maintained at 200 mTorr controlled by an automatic throttle valve. The system uses a capacitively coupled rf power source operating at 13.56 MHz. There are two parallel electrodes in this system, where the top is the driven electrode and the bottom is the earthed electrode. With the effects of the rf power source, the plasma is created due to the electrons breaking away from the host atoms in a gas present in the chamber. This plasma consists of ionized radicals, electrons and ions. Samples can be place on either electrode during depositions depending on how much ion-bombardment is desirable for the process at hand. At an rf frequency of 13.56 MHz, the more heavy ions have too much inertia to respond to the instantaneous electric field, unlike the more mobile electrons. This creates a time averaged negative DC self-bias close to the driven electrode. This negative bias is often called self-bias, since it is not externally applied but created by the asymmetry of the system. The self-bias between both electrodes is measured by a voltmeter between the plates, with a filter circuit to remove the rf components.

Films are formed using a CH_4/He and CH_4/Ar plasma. The addition of Helium or Argon to the methane plasma can greatly affect the film's properties and deposition rate. In the case of He, the excitation energy of metastable He atoms and the ionization energy of He atoms are larger than the ionization potential of CH_4 molecules. [41,42] The flow rate of methane and helium were in the ratios of 30:75 standard cubic centimeters per minute (sccm). This ratio was chosen so that there will not be too large a difference in ionization potential between the helium atoms and methane molecules and also there is no significant reduction in the deposition rate. Argon addition was found to have different effects to helium. When added to methane, it enhanced the fragmentation and varies the diamond-like properties of the a-C:H films,[43] therefore changing the sp^3/sp^2 ratios.

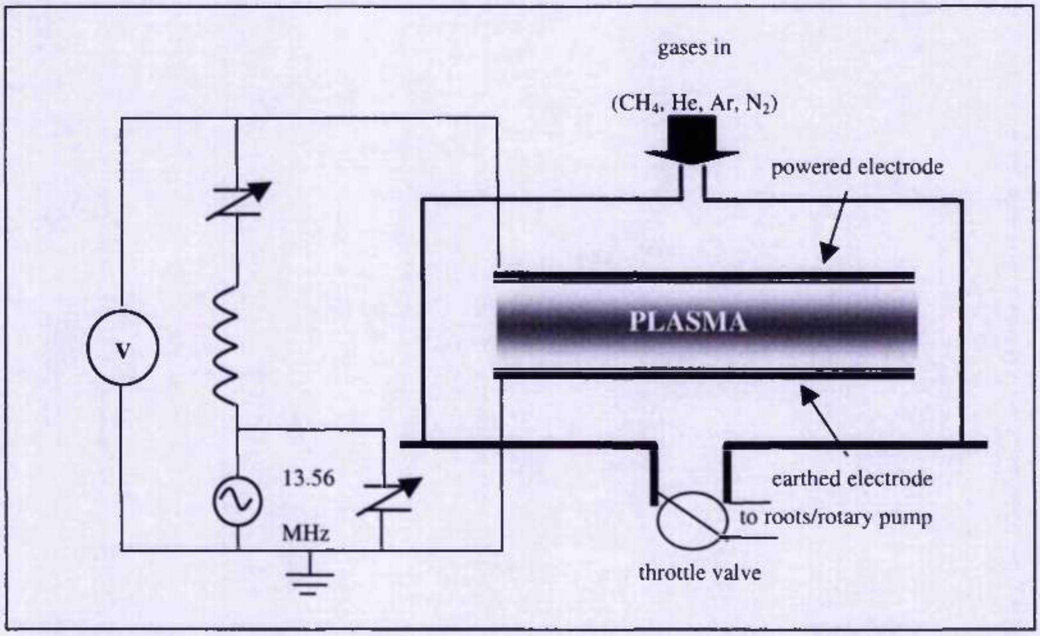

Figure 3-2: Schematic view of the DP800, rf-powered at 13.56 MHz. Substrates can be placed at both the top or bottom electrodes.

Varying the self-bias can result in more energetic ions impinging upon the electrode and substrate. This results in films that are more defective and usually with higher C-C sp^3 bonds.[44] However, when the C^+ ion energy is much high than 100eV, they tend to form into a natural form which is the C-C sp^2 graphitic states. These effects of changing the self-bias results in a series of variations in the optical band gap, refractive index and field emission properties.

3.2 Carbon nanotube-polystyrene composite preparation

A conventional plasma arc-discharge technique was used for the synthesis of multi-walled carbon nanotubes (MWNT). Two types of MWNT were synthesised, boron doped MWNT (BMWNT) and undoped MWNT. In this technique, two graphite rod electrodes of 5-20 mm diameter separated by about 1 mm were set up (shown in Figure 3-3). The electrodes were biased at 20-25 V resulting in a DC current flow of 50-120 A. The arc was operated at 500 torr Helium with a flow rate of 5-15 m*l*/s for quenching purposes. When an arc is formed, carbon deposit forms in the negative electrode, the length of the positive electrode also starts to decreases. No catalyst is required in this technique and MWNTs were found in bundles in the inner region of the cathode deposit. The inner region where MWNTs were found has a maximum temperature of 2500-3000 °C.

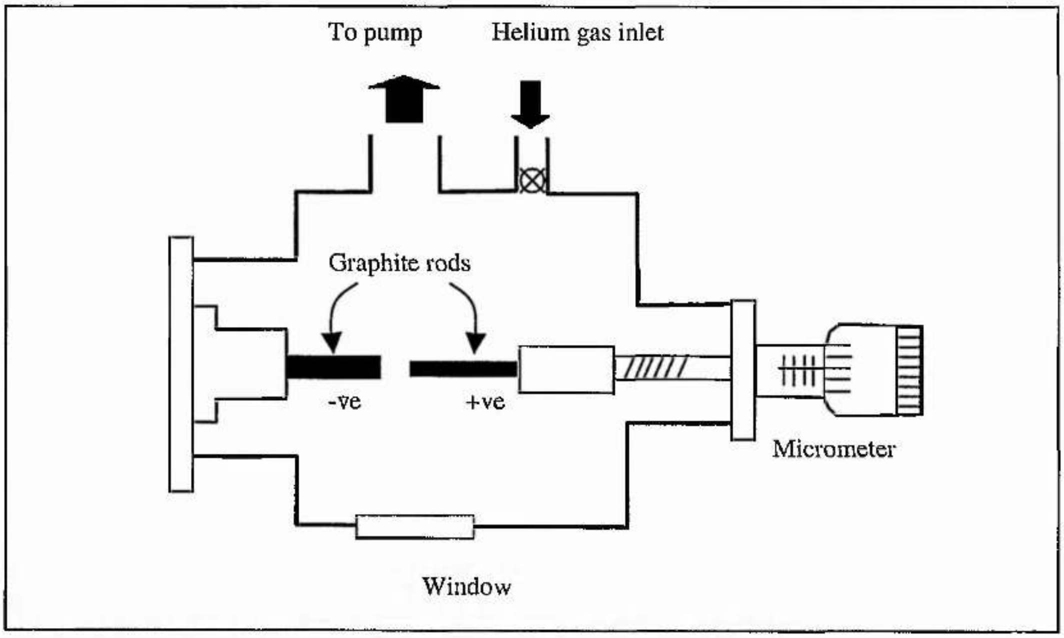

Figure 3-3: Arc discharged system for carbon nanotubes synthesis.

These nanotubes were subjected to a series of purification steps, by micro-filtering and mild oxidation to remove the polyhedral particles and the amorphous carbon coating. However, transmission electron microscopy (TEM) revealed that carbon particles are still present, albeit in low concentrations, compared to those unoxidized material. Polymer composites were produced by mixing the appropriate MWNT with a solution of polystyrene in toluene in various ratios (i.e 12.5, 2.5, 5 %, carbon to polymer, by weight). The carbon-containing polymers were then ultra-sonicated for 10 mins, before transferring into a Petri dish. The dish is then finally subjected to a vacuum to remove the toluene in a 10^{-2} torr vacuum. The final MWNT-PS films are produced by a hot-pressing technique at 100 °C.

3.3 Thin film characterisation

A series of characterisation techniques are required before the films can be tested for field emission. The film composite, thickness, optical density, electronic structure and surface morphology need to be determined.

3.3.1 Ellipsometry

Ellipsometry is an optical technique that uses polarised light to probe the dielectric properties of a sample. Measurements were carried out on a-C:H/silicon samples. This method is called the nulling technique. The optical setup (shown in figure 3-4) is constituted by a 1mW helium-neon laser operating at 632.8 nm monochromatic sources with an incident angle of 70° to the sample, a Transitronics manual rotating polarizer, a compensator (a quarter wavelength plate for example), an analyzer and a photomultiplier tube. The polarization is linear after the polarizer. It is elliptical after the compensator which is orientated to obtain a linear polarization after reflection on the sample. The analyzer is then orientated to extinguish the beam. The orientation of the polarizer P, of the compensator C and of the analyzer A allow one to obtain the ellipsometric parameters of the sample from:

$$\tan\psi \exp(j\Delta) = -\tan A * \frac{\tan C - \tan(P-C)}{1 + j\tan C \tan(P-C)}$$ *Equation 3-1*

Dedicated software was used to calculate the refractive index and film thickness. The thickness measurement was confirmed by a Sloan Dektak IIA profilometer. Further details are described elsewhere.[45]

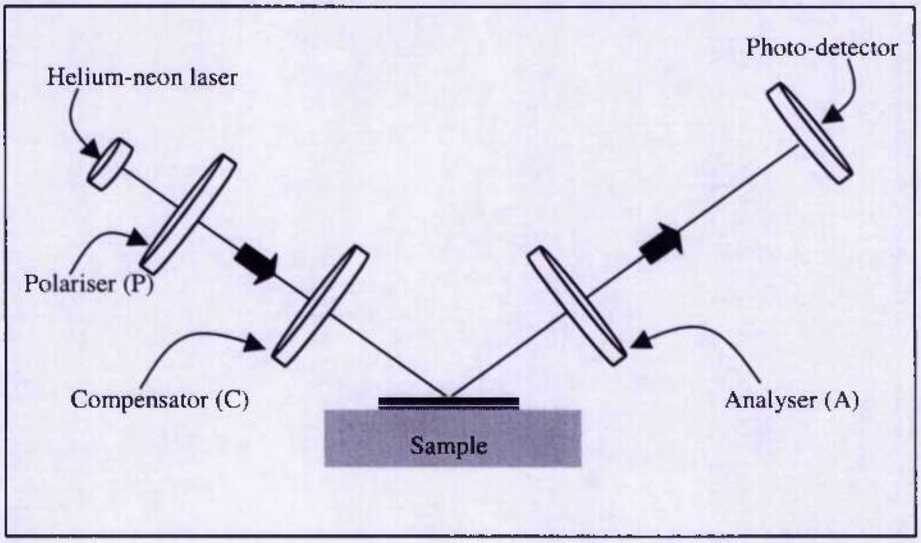

Figure 3-4: Schematic of an ellipsometer.

3.3.2 Optical absorption spectroscopy

The optical band gaps of a-C:H films are obtained by the measurement of the optical transitions between valence band electrons and conduction band electrons. This technique required the a-C:H film to be on a glass substrate in order to measure the optical absorbance. Transmittance of the sample is measured using a Camspec M330 spectrophotometer from 190-990 nm. The spectrometer used a deuterium ultra violet light source for wavelengths from 190- 350 nm and an incandescent light source for wavelengths from 350-990 nm. The wavelength was varied using a variable diffraction grating and the transmitted light was detected using a photodiode.

Using the data acquired, the following equation was used to calculate the absorption coefficient:

$$I = I_0 \exp(-\alpha d) \qquad \textit{Equation 3-2}$$

where, I is the intensity at a particular wavelength and d is the film thickness. I_0 is the control measured from a virgin corning glass (7059) substrate. α is determined as the absorption coefficient at a particular wavelength.

Quantifying of the optical band gap of the a-C:H films are difficult due to the presence of band tails in the amorphous states. There are two common methods used in obtaining the optical band gap from the absorption data. The first method determines the E_{04} optical band gap[46] by defining the edges of the optical band gap as the energies at which the absorption coefficient falls below the value of 10^4 cm^{-1}. The second method assumes that the density of states is parabolic in shape and therefore is it possible to extrapolate a band gap value. This is known as the Tauc band gap derived by Tauc [47].

3.3.3 Intrinsic stress measurement

Stress measurements were taken from a-C films deposited on 4 x 25 x 0.4 mm^3 (111) c-Si bars, by determining the radius of curvature of the film/substrate composite. An apparatus based on the detection of a He-Ne laser was used for this purpose. The curvatures of the film substrate structures were determined by the bending beam method using the system sketched in Figure 3-5. The use of two laser beams allows static measurements, i.e., without any mechanical movement. In addition, it substantially reduces the time spent on each measurement, making it possible to continuously acquire data as a function of temperature.

The stress of a thin film, deposited on a substrate, which has a length that is much greater than its width and thickness, is given by the modified Stoney equation,[48]

$$\sigma = \left[\frac{E_s}{1-v_s}\right]\left(\frac{t_s^{\,2}}{6t_f}\right)\left(\frac{1}{R}-\frac{1}{R_0}\right) \qquad \text{Equation 3-3}$$

where *E*, *v*, and *t* are the Young's modulus, Poisson's ratio, and thickness respectively. The superscripts *s* and *f* refer to substrate and film. R_0 and R are the radii of curvature of the substrate before and after the film is deposited.

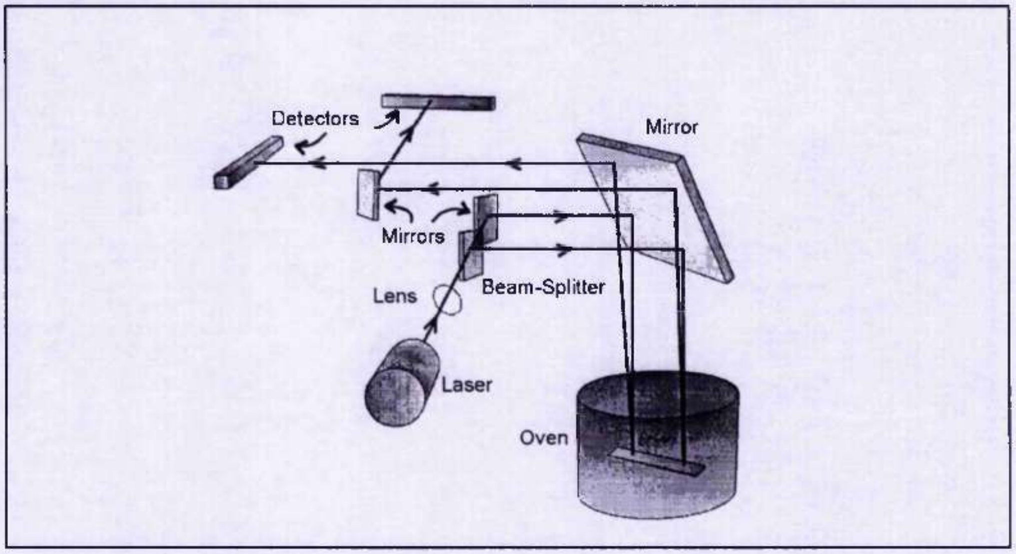

Figure 3-5: Setup of a optical curvature measurement system.

3.3.4 Photoelectron spectroscopy

Photoelectron spectroscopy utilizes photo-ionization and energy-dispersion analysis of the emitted photoelectrons to study the composition and electronic state of the surface region of amorphous carbon samples. This technique is sensitive to oxygen contamination and therefore in this work, the spectroscopy is conducted within the deposition chamber to prevent contamination. This technique can be subdivided according to the source of exciting radiation into:

- X-ray Photoelectron Spectroscopy (XPS) - using soft (200-2000 eV) x-ray excitation to examine core-levels.

- Ultraviolet Photoelectron Spectroscopy (UPS) - using UV (10-45 eV) radiation from discharge lamps to examine valence levels.

Photoelectron spectroscopy is based upon a single photon in/electron out process and from many viewpoints this underlying process is a much simpler phenomenon than the Auger process. The energy of a photon is given by the Einstein relationship:

$$E = h\nu \qquad \textit{Equation 3-4}$$

where h is Plank's constant (6.62×10^{-34} J s) and ν is the frequency (Hz) of the radiation

In XPS, the photon is absorbed in the amorphous carbon matrix, leading to ionization and the emission of a core (inner shell) electron. By contrast, in UPS the photon interacts with valence levels of the amorphous carbon matrix, leading to ionisation by removal of one of these valence electrons. The kinetic energy distribution of the emitted photoelectrons can be measured using any appropriate electron energy analyser and a photoelectron spectrum can thus be recorded. The process of photo-ionization can be considered in several ways. One way is to look at the overall process as follows:

$$A + h\nu \longrightarrow A^{+} + e^{-} \qquad \textit{Equation 3-5}$$

where A is the element/material being examined when irradiated with an x-ray of energy $h\upsilon$. Conservation of energy then requires that:

$$E(A) + h\nu = E(A^{+}) + E(e^{-}) \qquad \textit{Equation 3-6}$$

Since the electron's energy is present solely as kinetic energy (*KE*) this can be rearranged to give the following expression for the *KE* of the photoelectron :

$$KE = h\nu - (E(A^{+}) - E(A)) \qquad \textit{Equation 3-7}$$

The final term in brackets, representing the difference in energy between the ionized and neutral atoms, is generally called the *binding energy* (*BE*) of the electron - this then leads to the following commonly quoted equation:

$$KE = h\nu - BE \qquad \textit{Equation 3-8}$$

An alternative approach is to consider a one-electron model along the lines of the following illustration shown in Figure 3-6.

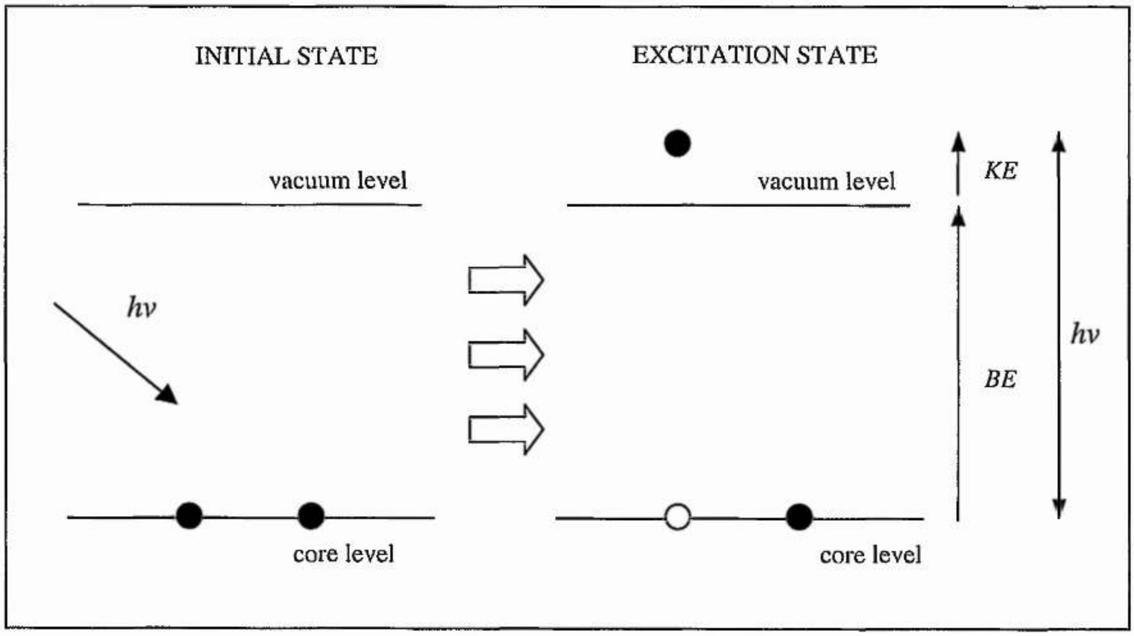

Figure 3-6: Excitation of photoelectrons from the core level electrons.

BE is now taken to be a direct measure of the energy required to just remove the electron concerned from its initial level to the vacuum level and the KE of the photoelectron is again given by Equation 3-8.

3.3.5 Electron-energy-loss spectroscopy

Electron energy loss measurements were performed on a Philips CM20 transmission electron microscope (TEM) at 100 keV, fitted with a Gatan imaging filter parallel EELS detection system. The samples were prepared for microscopy by "peeling" off the thin film on silicon substrates with $HF:HNO_3:H_2O$ (1:8:4) etching solution and placed on a Cu gride. The carbon K-edge spectra as well as the low-loss spectra were collected for each sample. The π^* peak at 285 eV of the carbon K-edge was fitted by a Gaussian curve, and its area normalised to he area of σ^* edge in the window 284-310 eV. A C_{60} sample was used as a reference for the absolute sp^2 bonding concentration. The sp^2 ratio was obtained using:

$$sp^2 \text{ ratio} = \frac{\left[\dfrac{area(\pi^*)}{area(\pi^*+\sigma^*)}\right]_{sample}}{\left[\dfrac{area(\pi^*)}{area(\pi^*+\sigma^*)}\right]_{reference}} \qquad \textit{Equation 3-9}$$

The plasmon energy is derived by fitting the energy-loss function to a single plasmon peak. The low-loss energy spectrum in EELS is proportional to the energy-loss function, $\mathrm{Im}(-1/\varepsilon)$ where ε is the complex dielectric function. Using the Drude model [49], ε can be expressed as:

$$\varepsilon(E) = 1 - \frac{E_p^2}{E^2 + iE\Gamma} \qquad \textit{Equation 3-10}$$

therefore,

$$\mathrm{Im}\left(\frac{-1}{\varepsilon(E)}\right) = \frac{E_p^2 E\Gamma}{\left(E^2 - E_p^2\right)^2 + \left(E\Gamma\right)^2} \qquad \textit{Equation 3-11}$$

where Γ is the full width half maximum (FWHM) of the loss peak and E_p is the plasmon energy:

$$E_p = \hbar\left(\frac{n_e e^2}{\varepsilon_0 m^*}\right)^{1/2} \qquad \textit{Equation 3-12}$$

where n_e is the valence electron density, ε_0 is the vacuum dielectric function and m^* is the electron effective mass.

3.4 Microscopy techniques

3.4.1 Scanning electron microscopy

Scanning electron microscopy (SEM) was used for direct examination of the film surfaces. By scanning with an electron beam that has been generated and focused by the operation of the microscope, an image is formed in much the same way as a television. The SEM allows a greater depth of focus than the optical microscope. For this reason the SEM can produce an image that is a good representation of the three-dimensional sample. The SEM uses electrons instead of light to form an image. A beam of electrons is produced at the top of the microscope by the heating of a metallic filament. The electron beam follows a vertical path through the column of the microscope. It makes its way through electromagnetic lenses that focuses the beam towards the sample. Once it hits the sample, other electrons (backscattered or secondary) are ejected from the sample. Detectors collect the secondary or backscattered electrons, and convert them to a signal that is sent to a viewing screen similar to the one in a standard CRT, producing an image. Figure 3-7 shows the setup of the SEM system.

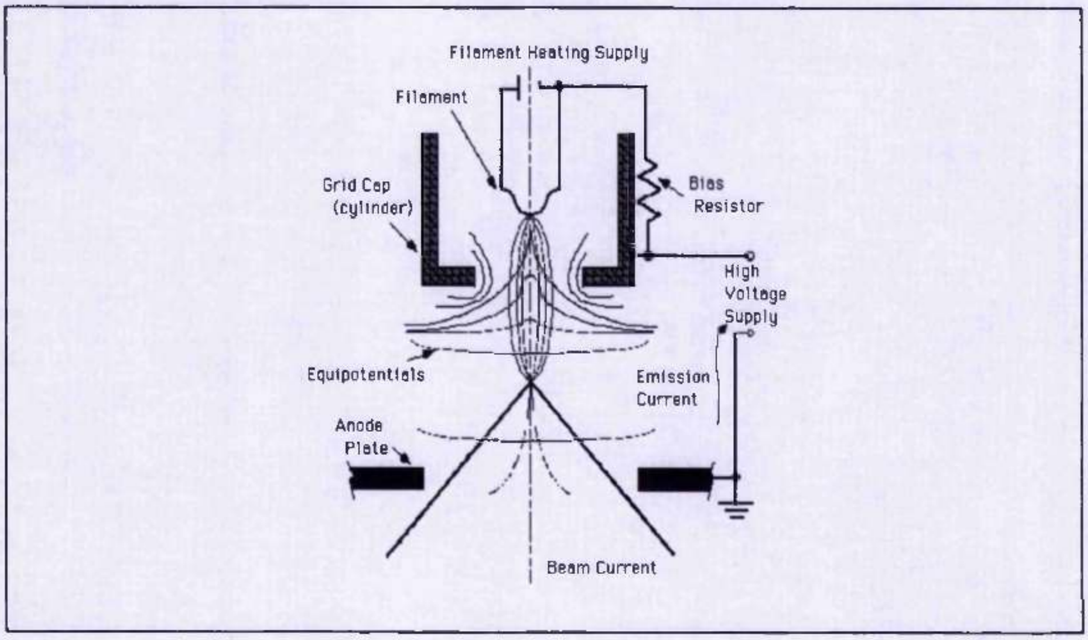

Figure 3-7: Setup of the SEM system

3.4.2 Scanning probe microscopy

This technique consists of two types of measurements, Atomic Force Microscopy (AFM) and Scanning Tunnelling Microscopy (STM). The system is a Multimode scanning probe microscopy by Digital Instrument III A System. This is a stationary probe technique, where the sample is scanned back and forth beneath the probe. The samples are mounted to a round 1.5 cm metal disk magnetically attached to the top of the scanner tube. As the scanner moves back and forth, the sample moves with it. This allows the probe to extract information from the sample surface. Figure 3-8 shows the setup of the system.

To investigate the topography across the sample, the AFM scanner was attached. This gives the image of the sample surface and the surface roughness can be extracted. When a STM scanner is attached, the topography of the surface electronic states using a tunnelling current, that itself is dependent on the separation between the probe tip and sample can be measured.

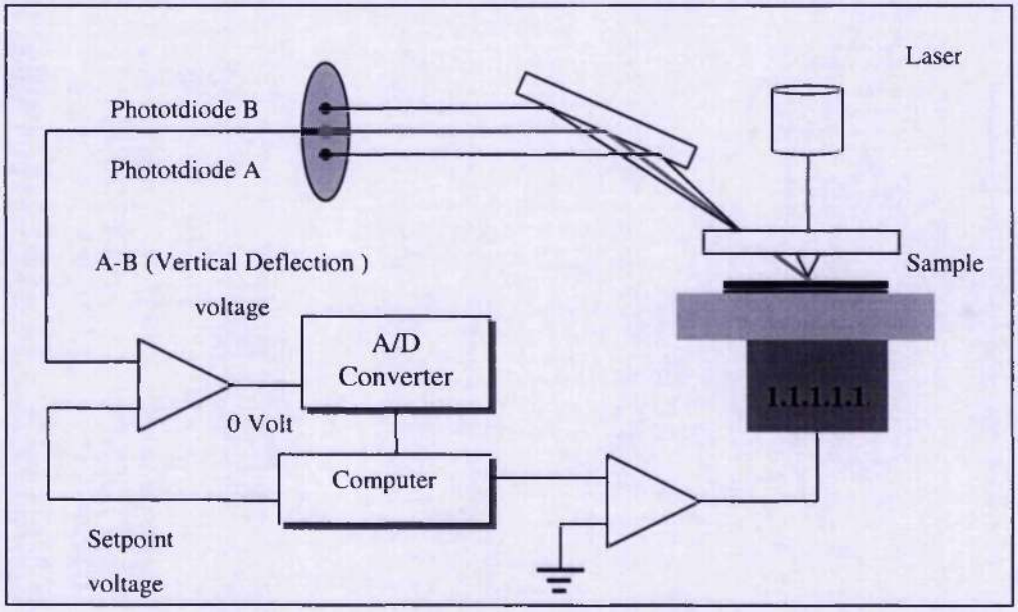

Figure 3-8: Setup of the Scanning Probe Microscopy system.

3.5 Field emission characterisation

To study the field emission characteristics of a particular material, four main factors need to be considered; the field emission threshold field, current density, emission site density and also field emission lifetime.

3.5.1 Probe measurements

In this technique, an external voltage was applied between the anode and emitter over a vacuum gap. The field emission characteristics were measured using a sphere-to-plane geometry, where the anode is a 5mm diameter stainless steel ball bearing. The experimental setup is shown in Figure 3-9.

The position of the anode can be adjusted via a Vacuum Generator HPT translator. This allows a field emission map of the sample. The chamber is pumped down to a vacuum better than 5 x 10^{-6} torr using the standard rotary-diffusion pump system. The power supply and multimeter are connected to a computer through an IEEE card. This allows the applied voltage and emission current measurement to be controlled via the computer. The vacuum gap is controlled by a stepper motor where each individual step is increased with an increment of 2.5 μm. The applied field in this technique is determined by the division of the applied voltage over the separation distance. The threshold field is determined by the electric field at which 1 nA of emission current is observed. For each sample, measurements were made at 5 or more different positions. This allows a mapping of the uniformity of the sample. The applied voltage is controlled by the computer. The voltages were increased from 0 - 2200 V or where a maximum emission current of 3 x 10^{-5} A is observed.

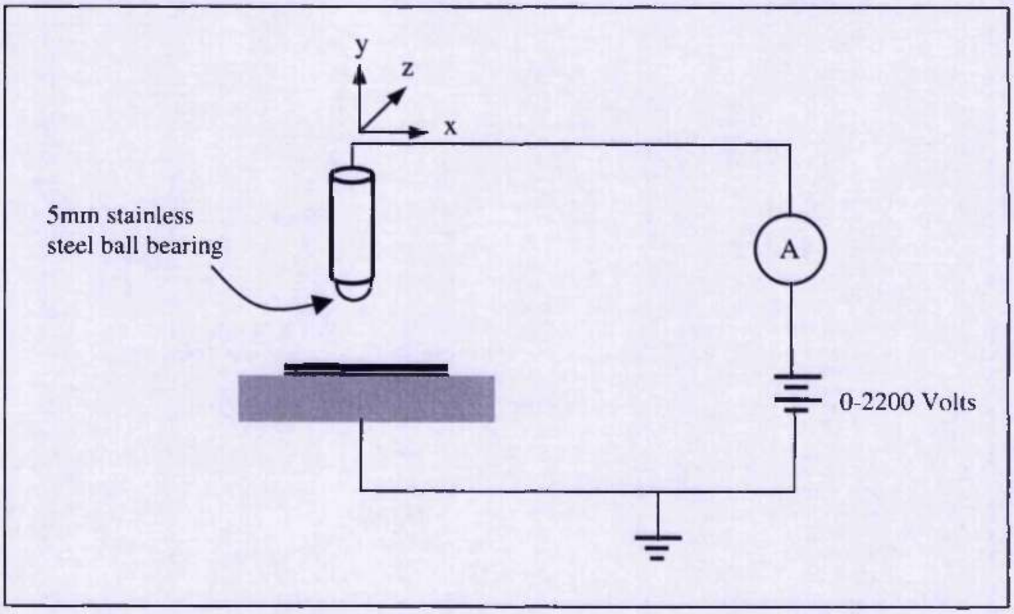

Figure 3-9: Probe setup of the field emission testing system.

3.5.2 Planar measurement / site density maps

In order to test the field emission characteristics in a larger area than the probe measurements, a planar configuration is setup. An Indium-Tin-Oxide (ITO) coated glass replaced the ball bearing in the probe setup. In order to determine the distance between the anode and emitter, a polyterafuoroethylene (PTFE) insulator with a known thickness is used as a separator. The measured emission current was divided by the tested area to give the current density. The tested area is determined by the size of the PTFE, usually from 5 mm^2 to 35 mm^2.

In order to investigate the site density, an additional CCD camera is placed on top of the sample. Also the anode is replaced with a phosphor/ITO/glass slide. When the phosphor comes in contact with the emitted electrons, light is produced. This technique is similar to the current density measurement but gives information on where the emission spots are formed. Figure 3-10 shows the setup of mounting the sample.

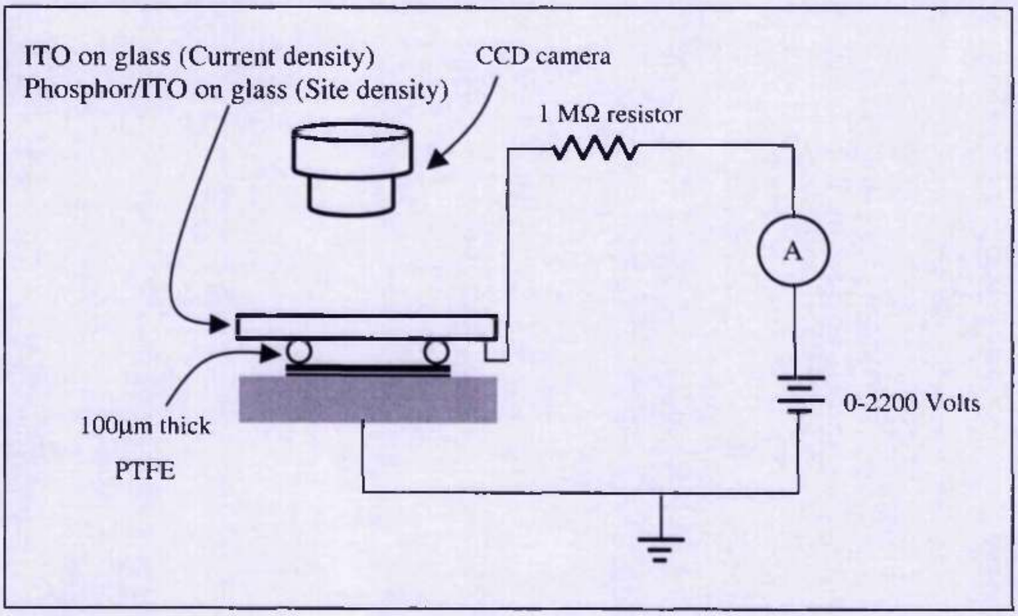

Figure 3-10: Planar setup of the field emission system, the CCD camera is installed to allow capturing of the emission sites.

3.5.3 Comparison of planar and probe measurements

In the planar setup, the samples are tested over a larger area. It has the advantage of obtaining a lower threshold field (E_{th}) as compared to probe technique. Table 3-1 compares the threshold fields of a-C films measured by both the planar and probe technique in the literature. It can be seen that field emission measurements using an ITO/glass slide as an anode (planar method) produces threshold fields that are on average about 7 V/μm. On the other hand, probe technique results in threshold fields in the range of about 20 V/μm. The planar setup usually measures over an area of 10 mm^2 which means that the emission characteristics will be dominated by the emission sites with the lowest threshold fields (or higher β). Also, addition field enhancement can come from the edge effects of the PTFE insulator. As for the probe measurements, the emission is measured over a much smaller localised area and therefore probes individual emission sites which are subjected to a smaller, more the tense threshold field.

Threshold field	**Anode used**	**Gap**	**a-C film deposition**	**Ref.**
6 V/μm	ITO/glass	60 μm	Filtered cathodic arc (-100 V)	[50]
8 V/μm	ITO/glass	50 μm	rf-PECVD (-100V)	[51]
7 V/μm	ITO/glass	100 μm	rf-PECVD (-100V)	[52]
22 V/μm	2 μm W probe	10 μm	Pulsed laser deposition (5 J/cm^2)	[53]
20 V/μm	5 mm Stainless steel probe	40 μm	rf-PECVD (-100V)	[25]
16 V/μm	100 μm Cu probe	80 μm	MPCVD	[54]

Table 3-1: Comparison of E_{th} of various a-C films measured with planar and probe technique.

The main limitation of planar measurements is the possibility of a leakage current caused by the PTFE insulator under very high-applied voltages. Therefore, careful selection of applied voltage is necessary and care should be taken not to place any spacers on the emitting surface to prevent short circuiting. Interestingly, the difference in threshold fields observed in both techniques indicates that the field emission characteristics from a-C films are localised and are in agreement from the "spotty" site density.

Chapter 4

4 Physically-based device simulation

Physically-based device simulators predict the electric characteristics that are associated with specified physical structures and bias conditions. This is achieved by approximating the operation of a device onto two or three dimensional grids, consisting of a number of grids called nodes. By applying different sets of differential equations, derived from Maxwell's laws (onto this grid), it is possible to simulate the transport of carriers through a structure. This means that the electrical performance of a device can now be modelled in DC, AC or transient modes of operation. This software can also be used to simulate quantum effect of semiconductors based on classic analysis.

4.1 Silvaco simulation software

Figure 4-1 shows the type of information that flows in and out of the Atlas device simulator. Firstly, the problem to be simulated was defined by either a text file that contains the commands from Deckbuild, or a structure file that defines the structure from Devedit. The relevant physical models were included into the simulator after the consideration of the required equations to be solved. Finally, the bias conditions for which the electrical characteristics are to be simulated were incorporated into the simulator.

The Atlas simulator solves the defined problem/structure by considering each case as a set of fundamental equations that link together the electrostatic potential and the carrier densities within the simulation domain. These equations have been derived from Maxwell's laws and consist of Poisson's equation, and the continuity equations. Poisson's equation relates variations in electrostatic potential to local charge densities. The continuity equations describe the way that the electron and hole densities evolve as a result of the transport processes, generation processes and recombination processes.

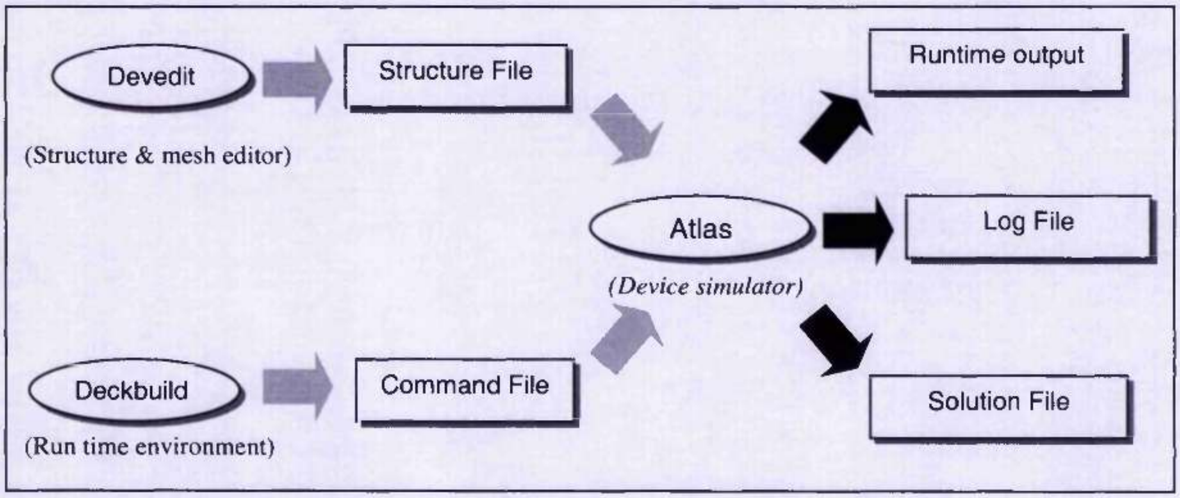

Figure 4-1: Flow of the information going in and out of the Atlas simulator.

There are three types of output files from the simulator. The run time output determines the progress of simulations running, and this is where error warnings message appear. Log files store the summaries of electrical output information, and solution files store the values of solution variables within the device. The output files can be viewed by Tonyplot which provides the visual solution of the device behaviour.

4.2 Specifying material properties

All materials are split into three classes: conductors, semiconductors and insulators. Each class has a set of default parameters that can be altered. For semiconductors, parameters such as electron affinity, band gap and density of states can be determined.

Amorphous materials are modelled by defining a set of defects states within the bandgap of a material. The defect state is a combination of exponentially decaying band tail states and Gaussian distributions of mid gap states.[55] The defects statement is as follow:

```
Defects     nta=1e21 ntd=1e21 wta=0.033 wtd=0.049 \
            nga=4.5e15 ngd=4.5e15 ega=0.62 egd=0.78 wga=0.15 wgd=0.15 \
            sigtae=1e17 sigtah=1e-15 sigtde=1e-15 sigtdh=1e-17 \
```

siggae=2e-16 siggah=2e-15 siggde=2e-15 siggdh=2e-16

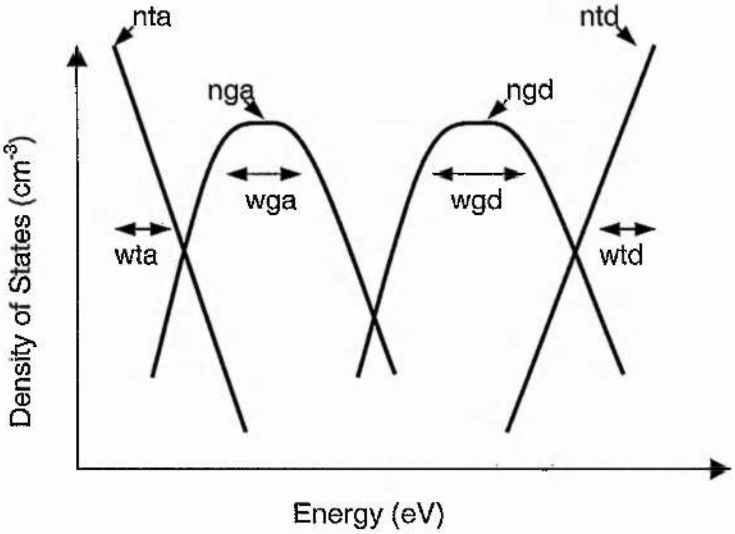

Figure 4-2: Density of states of the defects energy.

The density of states of the defined material is shown is Figure 4-2. The values are given in the Silvaco examples for the TFT experiment.

4.3 Field emission simulation models

The two main field emission mechanisms modelled in the simulator are the Fowler-Nordheim tunnelling and hot carrier injection. The Fowler-Nordheim equation expresses tunnel current density through the vacuum as:

$$J_{FN} = A_{FN} E^2 \exp -\frac{B_{FN}}{E} \qquad \textit{Equation 4-1}$$

where,

E is the magnitude of the electric field

$A_{FN} = 1.82 \times 10^{-7}\ \mathrm{CV^{-2}s^{-1}}$

$B_{FN} = 1.90 \times 10^{8}\ \mathrm{V/cm}$

In this model, the Fowler Nordheim constants are different to those in Equation 2-1 because the work function is fixed at 2 eV. A_{FN} and B_{FN} can be varied to the work function of the simulated material. During the simulation, each electrode-insulator and semiconductor-insulator interface is divided into discrete segments that are based upon the mesh. For each segment, the Fowler-Nordheim current is calculated as described above. This current is then added to a segment on the electrode-insulator boundary.

The hot carrier injection current is calculated using the 'lucky' electron model [56]. Like the Fowler-Nordheim model, each segment calculates the injected current into that segment. The total current is then the sum of all of the discrete values. The formula calculates the injected current contributed from every node point within the semiconductor according to:

$$I_{inj} = \int\int P(x, y) \left|\vec{J}(x, y)\right| dx\, dy \qquad \text{Equation 4-2}$$

where $\vec{J}$ is the carrier current density, and

$$P(x, y) = P_{\phi B} P_1 P_2 / \lambda_r.$$

$$P_{\phi B} = 0.25\left(\frac{E_{\|}\lambda}{\phi_B}\right)\exp\left(-\frac{\phi_B}{E_{\|}\lambda}\right)$$

$$P_1 = \exp\left(-\frac{y}{\lambda}\right)$$

$$P_2 = \exp\left(\sqrt{\frac{E_{\circ}}{E_{\perp}}}\right)$$

$$\phi_B = \phi_{Bo} - \beta\sqrt{E_{\perp}} - \eta E_{\perp}^{2/3} - \Delta\psi(x, y)$$

where:

$P(x, y)$ is the total probability

$P_{\phi B}$ is the probability of acquiring sufficient momentum to surmount barrier ϕ_B.

P_1 is the collision-free travel to the barrier peak.

P_2 is the probability of the scattering in vacuum.

λ is the scattering mean free path.

λ_r is the redirection scattering mean free path.

ϕ_{B0} is the barrier height for electrons (3.2V).

$E_{\parallel}$ is the electric field parallel to the current flow.

$E_{\perp}$ is the electric field perpendicular to the thin film/vacuum interface.

y is the distance to the thin film/vacuum interface.

4.4 Other Models

There are other models that are also included in the simulation

FLDMOD -	specifies a lateral electric field-dependent model.
BBT.STD -	specifies a standard band-to-band tunnelling model.
E.BENDING -	specifies that electron band bending will be taken into account for electron injection.
BGN -	specifies band-gap narrowing.

These models are included to allow changes in the band energy. The interface between the a-Si thin film and vacuum are subjected to possible band bending according to the Space Charge Induced Band Bending model [10]. The use of the above models is required whenever the F-N and HEI models are used.

Chapter 5

5 Field emission properties of polymer-like amorphous carbon thin films

5.1 Introduction

Low macroscopic field emission from a-C films with no distinct surface protrusions has been disputed and discussed by the scientific community. The field emission mechanism from a-C films to account for this phenomenon is still unclear. However, the field emission characteristics of a-C films are strongly influenced by many parameters such as sp^2/sp^3 ratio in the films, surface morphology and bonding configuration. Recent reports suggested that non-surface geometrical enhancement could be a proximity effect from the conductive sp^2 clusters within the films. This phenomenon has been used to explain the unusually low emission thresholds seen in many atomically flat a-C films. The dielectric inhomogenities are the result of having more conductive sp^2 clusters surrounded by an insulting sp^3 matrix. [18] Raman spectroscopy indicates that sp^2 clusters of the order of 1–10 nm range can improve the field emission properties by facilitating emission. [16] It has been proposed that by reducing the separation distance between these nano-conductive clusters, a higher field enhancement can be achieved within the thin films.[18]

5.2 Effects of Argon dilution

Hydrogenated amorphous carbon (a-C:H) thin films have been widely studied in recent years due to possible applications in coatings and field emission cathodes.[57] Among the various methods used to deposit a-C:H films, rf-plasma enhanced chemical vapour deposition (rf-PECVD) is the most widely accepted process. Using a CH_4 plasma, the films are deposited from rf glow discharge of hydrocarbon gases, generally diluted with a noble gas. Depending on the deposition conditions such as dc self-bias, films vary from soft polymer-like amorphous carbon (PAC) to more diamond-like amorphous carbon (DAC). To date there have been numerous reports from these materials on field emission at low macroscopic electric fields.[58,10] However, in DAC films and tetrahedral amorphous carbon (TAC), the emission is likely to be influenced by the barrier at the film surface/vacuum interface due to the degree of defects within the films microstructure. The defect density which is associated with the more conductive sp^2 clusters within the film, is usually several orders of magnitude > 10^{18} cm^{-3}.[18] This effectively results in the screening of the applied field to a thin surface layer within the film. Therefore, large internal electric fields to accelerate the electrons at the back contact were deemed to be improbable. The sp^2 content within the DAC is important to understand the field emission results.

Identifying and controlling the properties important for field emission is crucial in designing bespoke emitter cathodes. This can be achieved by control of the plasma conditions which dictate deposition conditions and thus produce a wide variety of a-C:H films. One possible way to pursue this investigation is to study the effects of diluting methane with noble gases such as argon. This may pinpoint the physical properties of the films as a function of plasma chemistry for different CH_4/Ar ratios. Earlier studies [59,60] have shown that Ar-dilution effectively changes the plasma chemistry and produced films which are harder. This variation was attributed to the higher degree of structural order of the sp^2 lattice. In most cases, films with a stronger graphitic character have been observed, due to the larger number or size of the carbon sp^2 units.

5.2.1 Experimental detail

a-C:H films were deposited on the driven electrode of a Plasma Technology DP800 capacitively coupled radio frequency (13.56 MHz) plasma enhanced chemical vapour deposition (PECVD) system. The negative d.c. self bias voltage was set at -200 V with reference to ground for all depositions. The silicon and glass substrates were deposited with different flow ratios determine by $\frac{CH_4}{CH_4 + Ar}$ with ratios from 10% to 100%. Pressure during growth was kept constant at 200 mTorr, with the flow rate of CH_4 and Ar varied in the chamber. Film thicknesses were determined using ellipsometry and are in the range of 80 nm to 110 nm. Optical bandgaps were measured using a UV-visible spectrometer. The field emission characteristics of these films were determined by a planar-to-sphere geometry setup

[25], with a 5 mm stainless steel ball bearing anode suspended 40 μm above the film surface. The samples were tested in vacuum better than 4 x 10^{-6} mbar and conditioning cycle of the FE characteristics were observed in all the films [61]. The threshold field (E_{th}) is determined as the macroscopic electric field when an emission current of 1 nA is recorded. Electron energy loss measurements were performed on a Philips CM20 transmission electron microscope (TEM) at 100 keV, fitted with a Gatan imaging filter parallel EELS detection system. A C_{60} sample was used as a reference for the absolute sp^2 bonding concentration. The sp^2 concentration was obtained using the same method employed by Fallon *et al.* [62]

5.2.2 Thin films characterisation

The increase of the deposition rate with increasing methane concentration is shown in Figure 5-1(a). The introduction of Ar changes the deposition mechanism, inducing changes in the physical and chemical bombardment on the film surface as well as the plasma temperature and thus its properties. As the relative methane concentration in the chamber is increased with decreasing percentage of Ar, the deposition rate increase from 3 nm/min to 28 nm/min. The negative self-bias is kept constant at -200 V for all the depositions. The effect of having less Ar in the chamber reduces the sputtering effects cause by the Ar^+ bombardment during the growth process. It should also be noted that by having a noble gas such as Ar mixed in with CH_4 tends to increase the energy distribution of the plasma and thus the ionisation of carbon radicals [63]. Therefore, by observing an increase in the growth rate with decreasing Ar it would be expected that a softer film with a more polymeric component with higher C-H bonding would be obtained. This would then tend to lower the refractive index too. Figure 5-1(b) illustrates the variation of the refractive index against the methane concentration. The refractive index fell from 3.2 at 10% $CH_4/(CH_4+Ar)$ to 2.1 at 100% methane. This signifies an expected densification of the films at high Ar concentration, due to the higher ionisation of the plasma as well as higher Ar^+ densification due to bombardment on the surface of the a-C:H film during the growing process. H could also be preferentially sputtered as the displacement threshold is much lower for H than it is for carbon. This results in the films having a higher carbon/hydrogen ratio in the films with lower (CH_4/CH_4 +Ar) ratio.

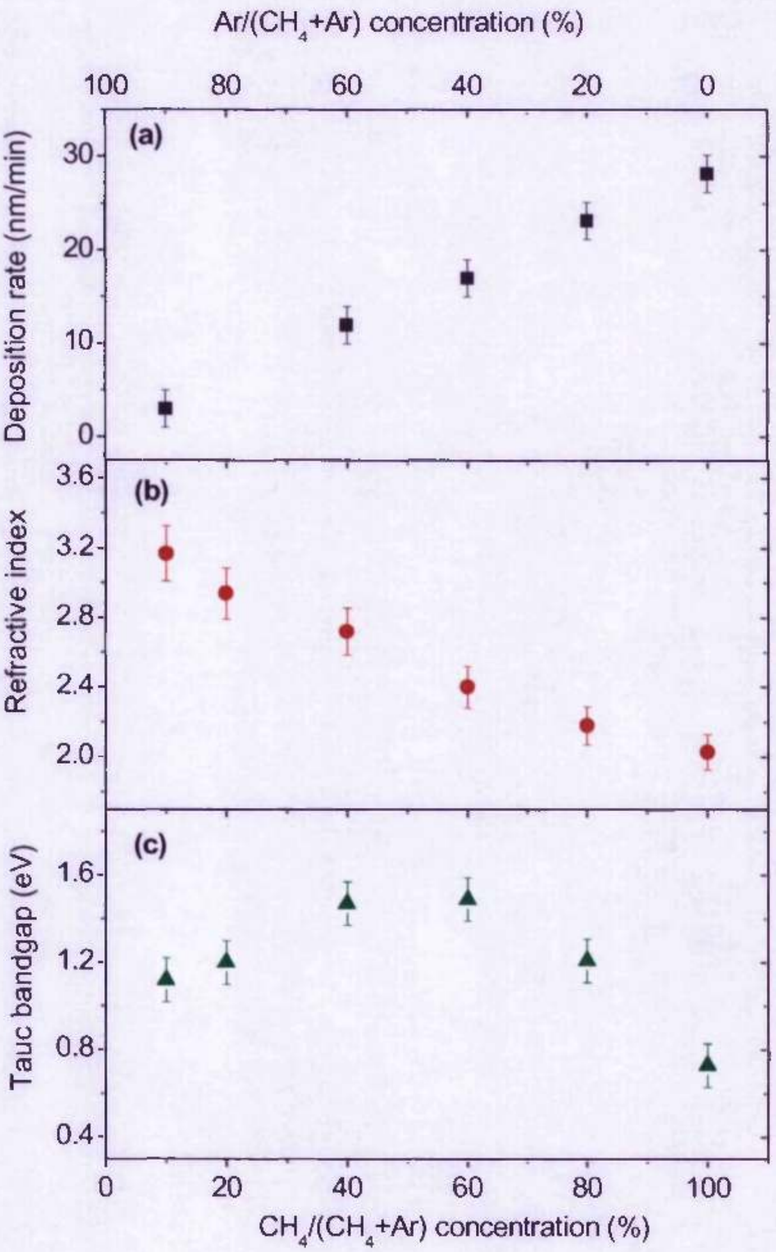

Figure 5-1: Variation of the (a) deposition rate, (b) refractive index and (c) Tauc bandgap as a function of the CH_4 concentration for films deposited at 200 mTorr and -200 V self bias.

Changing the plasma chemistry also results in modification of the optical Tauc bandgap. The Tauc bandgap is a useful parameter to characterised the π states in the a-C:H films. It gives a measure of the sp^2 cluster size in the a-C:H films. The π and π^* bonds form the band edges and therefore control the optical bandgap. As shown in Figure 5-1(c), the Tauc bandgap increases from 1.1 eV to 1.5 eV as the Ar concentration is decreased due to the more polymeric nature of the films. However, after 60% $CH_4/(CH_4+Ar)$ ratio, the Tauc bandgap fell to 0.7 eV at 100% methane plasma. This implies a significant increase in the size of the π state clusters in the films.

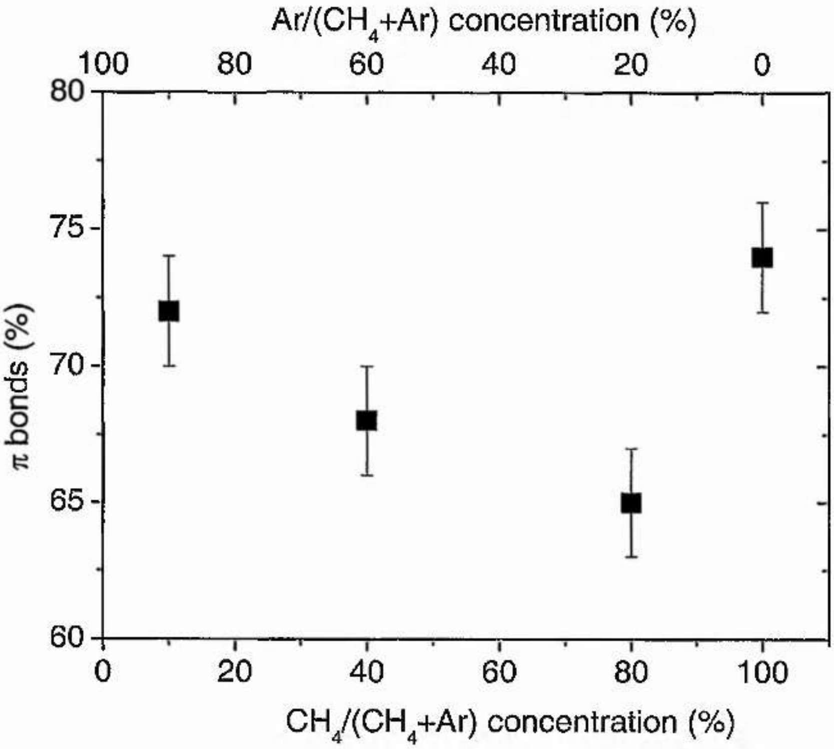

Figure 5-2: EELS measurements of the π bond concentration as a function of the CH_4 concentration.

The π bonding content is determined by the number of sp^2 bonds in the a-C:H films as the sp^3 sites do not contain any π bonding. Therefore, measuring the π bonding is an efficient method in probing the sp^2 concentration within the a-C:H films. Using EELS, the measured π bonding concentration is shown in Figure 5-2. The π bond concentration was initially 71% at a $CH_4/(CH_4+Ar)$ ratio of 10%, as the Ar concentration is reduced in the plasma, the π bond concentration fell to 68 % and 64.5% with 40% and 80% $CH_4/(CH_4+Ar)$ ratio respectively. However at 100% $CH_4/(CH_4+Ar)$ ratio, the π bonds concentration increases to 74 %. This result shows that a high concentration of Ar in the plasma could induce the formation of π bonding in the films either due to variations in the plasma chemistry or due to higher percentage of Ar^+ bombardment or amorphisation. This result can also be used to explain the variation observed in the Tauc bandgap measurements.

5.2.3 Field emission analysis

The field emission results on the other hand show an interesting and unexpected correlation to the π bond hybridisation. Figure 5-3 shows the variation of the threshold field for the films deposited with different methane concentrations. At a $CH_4/(CH_4+Ar)$ ratio of 10%, the threshold field is initially at 21 V/μm, and as the $CH_4/(CH_4+Ar)$ ratio increases to 60%, the threshold field increases to a maximum of 34 V/μm. However, when the $CH_4/(CH_4+Ar)$ ratio is set at 100%, the threshold field fell back to about 25 V/μm. It is important to note that this result suggests that the strong correlation in the π bonds and Tauc bandgap may also be related to the field emission results. It is interesting to note that the observed trend is opposite to that obtained for TAC films,[64] where the emission threshold field is controlled by the sp^3 content rather than sp^2. However, this result is consistent with those reported for a-C:H films [65] and sputtered TAC [66], indicating that sp^2 concentration in the a-C:H films plays an important role for field emission. It also suggests that the field enhancement mechanisms that appear in the different a-C films may be related.

The variations in the electron threshold fields can be explained by the changes in the sp^2 content. The reduction in sp^2 content results in an increase in the threshold field. However, the effects of the sp^2 clusters in the field emission mechanism can be explained by the proximity effects of these clusters. This would require the conductive sp^2 clusters to be very close to each other near the film surface. They also need to be embedded in a more insulating sp^3 matrix. The size and number of these sp^2 clusters also need to be optimised in order to achieve sufficient field enhancement. Another advantage of having these conducting clusters is that they can provide an effective means to replenish emitted electrons from the back silicon substrate.

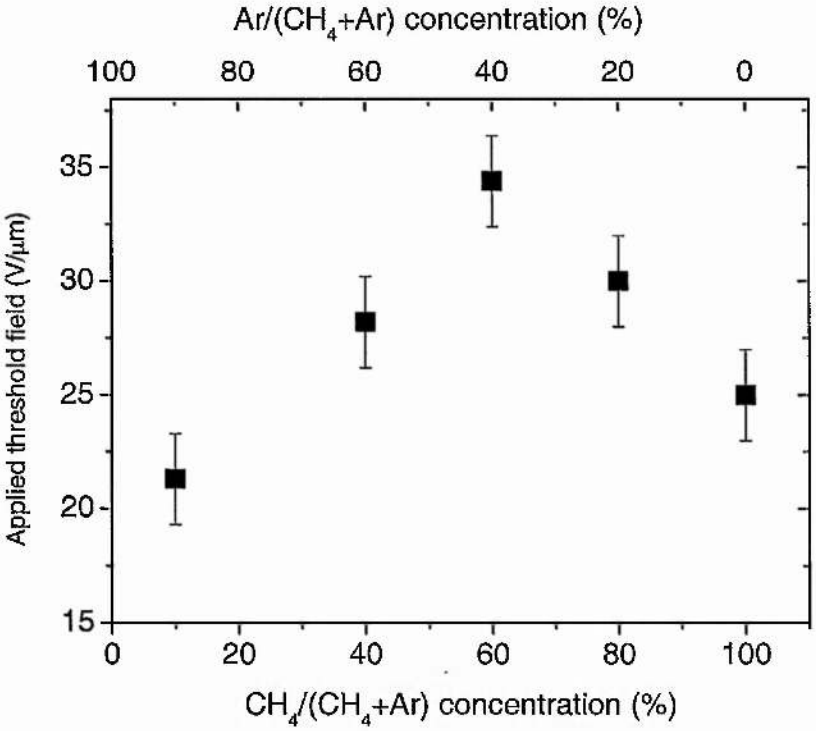

Figure 5-3: Variation of the threshold field against the CH_4 concentration.

5.2.4 Summary and discussions

The field emission threshold and Tauc bandgap is plotted versus the π bond concentration in Figure 5-4. It can be seen from the data that the films with the highest sp^2 concentrations and thus the lowest Tauc bandgaps have a lower threshold field than the films with a higher Tauc bandgap (and lower sp^2 concentration). This indicates the importance of the size and concentration of sp^2 sites in the films. To investigate the sp^2 cluster size, more detailed analysis such as Raman spectroscopy needs to be performed. However, in the work by Carey *et al.*[14], it has been shown that the threshold field from a-C:H films decrease as the Tauc gap decreases. It was proposed that the narrowing in the Tauc gap is related to the increase of the sp^2 cluster size. This was further supported by the electron paramagnetic resonance measurements. In order to explain the lower threshold field observed in the highly Ar diluted films, the key factor is likely to lie in the plasma chemistry during the growth process. In the film with high Ar dilution (90% Ar/(CH_4+Ar)), the bombardment from the Ar^+ is more intense. This would result in the sp^2 clusters being smaller and more fragmented than the films with 100% methane plasma during growth. We believe that the bombardment effects by the Ar^+ causes the smaller clusters to be placed closer to each other. This would further increase the field enhancement between the clusters and therefore give a lower threshold field. Simulation studies on the conductive spheres have shown that by reducing the separation distance of the spheres from 15 nm to 1 nm, one can increase the field enhancement factor from 10 to 23.[67] This field enhancement could therefore decrease the threshold field further.

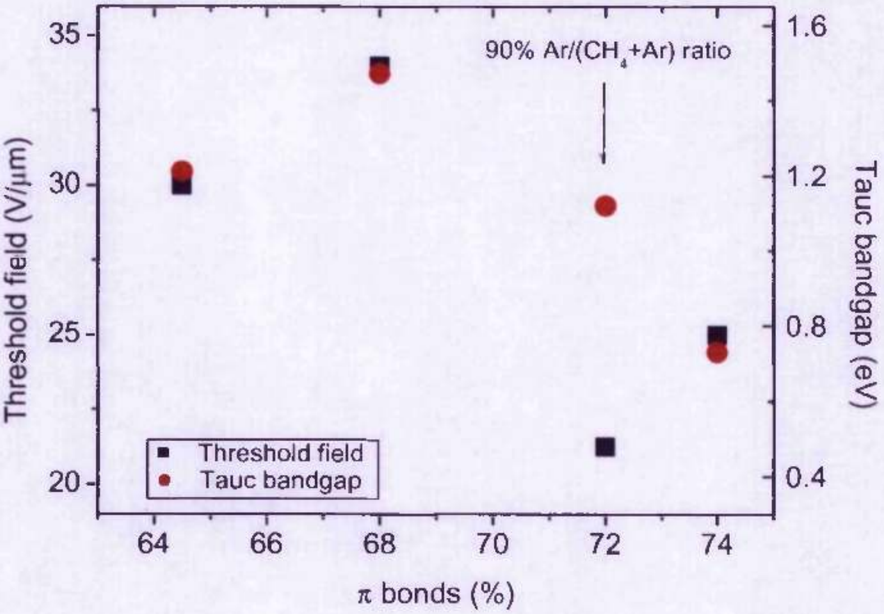

Figure 5-4: Variation of (a) threshold field and (b) Tauc bandgap as a function of the π bond concentration.

Another important point to note is the fact that the decrease in the threshold field is offset from the decrease in the optical gap by a definite sp^2 content. It could point to the fact that before the formation of larger sp^2 clusters that decrease the bandgap there is an ordering of the sp^2 sites as observed in the ion implantation [68] as well as annealing of TAC films [69].

In summary, the field emission properties from different Ar dilution a-C:H films were studied. The changes in the sp^2 concentration have been observed to control the emission threshold fields. The field enhancement which is controlled by the sp^2 content has been explained due to proximity effects. The effect of having a high Ar dilution brings the conductive clusters closer together which results in a lower threshold field for field emission. Similar phenomena have been observed in the ordering of sp^2 states before the onset of graphitisation in the TAC films.

5.3 Field emission from nitrogenated amorphous carbon

The field emission properties of nitrogen incorporated a-C:H (a-C:H:N) films are investigated in this section. In section 5.2, the effects of Ar dilution concluded that sp^2 concentration plays an important role in electron field emission. Since a-C:H:N films are usually associated with high sp^2 concentration or/and n-type doping, it is interesting to investigate its field emission properties as a function of nitrogen content. There has been evidence which shows that nitrogenation of a-C:H results in n-type doped a-C:H films. [70,71] However, excessive graphitisation by including nitrogen can remove the doping effect, especially when bandgaps collapse towards 0 eV. In this section, the effects of nitrogenation on graphite-like amorphous carbon is investigated.

5.3.1 Experimental detail

These films were deposited on the cathode electrode of a glow discharge system in a methane and nitrogen atmosphere. The substrate temperature was kept below 100 °C at a chamber pressure of 90 mtorr and the bias voltage was maintained at –800 V. The use of this condition was motivated by the field emission results from highly graphite-like amorphous carbon. [14] Incorporation of nitrogen was obtained by controlling the nitrogen gas content in the chamber during deposition. These films are deposited on silicon substrates and the film thicknesses were about 1 μm measured by a Dektak profilometer. EELS and FTIR were used to determine the relative nitrogen concentration in the films. Both techniques give similar nitrogen concentration.

Figure 5-5 shows (a) the film resistivity and (b) deposition rate of these films. The deposition rate decreases from 1 to 0.08 nm/s as the N content increases from 0 to 7 at. % respectively. Two effects can explain this; increases in N_2 gas in the chamber dilute the methane gas during deposition and N acts as a sputtering agent during deposition. The film resistivity measured by a four-point probe indicates that the increase in N content results in the decrease of the sheet resistivity. This can be attributed to either n-type doping effect or the increase in sp^2 concentration. The optical Tauc gap of these films did not vary with N content and is generally about 0.5 eV. Therefore, the decrease in film resistivity is likely to be due to the increase in graphitisation.

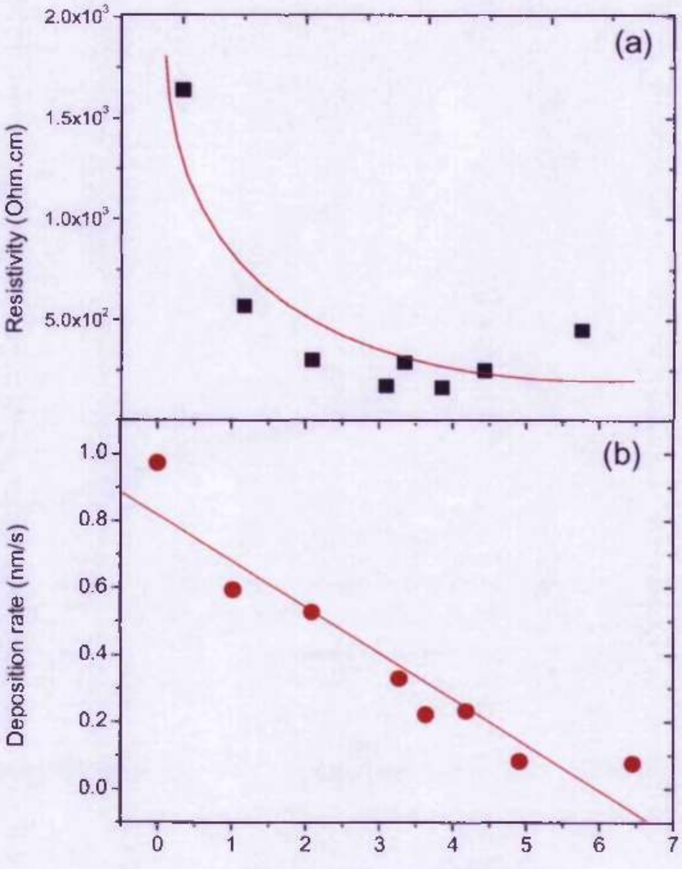

Figure 5-5: Film resistivity (a) and deposition rate (b) as a function of the Nitrogen concentration. A fit to this data based on (a) a quadratic data set and (b) a linear data set is shown.

5.3.2 Raman spectroscopy analysis

Micro-Raman spectroscopy was conducted at room temperature in a backscattering configuration. Figure 5-6 shows the Raman spectra of the a-C:H:N deposition with different N concentrations. The spectra is composed of two carbon related peaks, a *G* peak at ~1560 cm^{-1} and *D* peak at ~1350 cm^{-1}. The intensity of the *D* peak is related to the presence of sp^2 sites in six fold aromatic rings and the *G* peak is sensitive to all sp^2 sites including aromatic rings and olefinic chains.

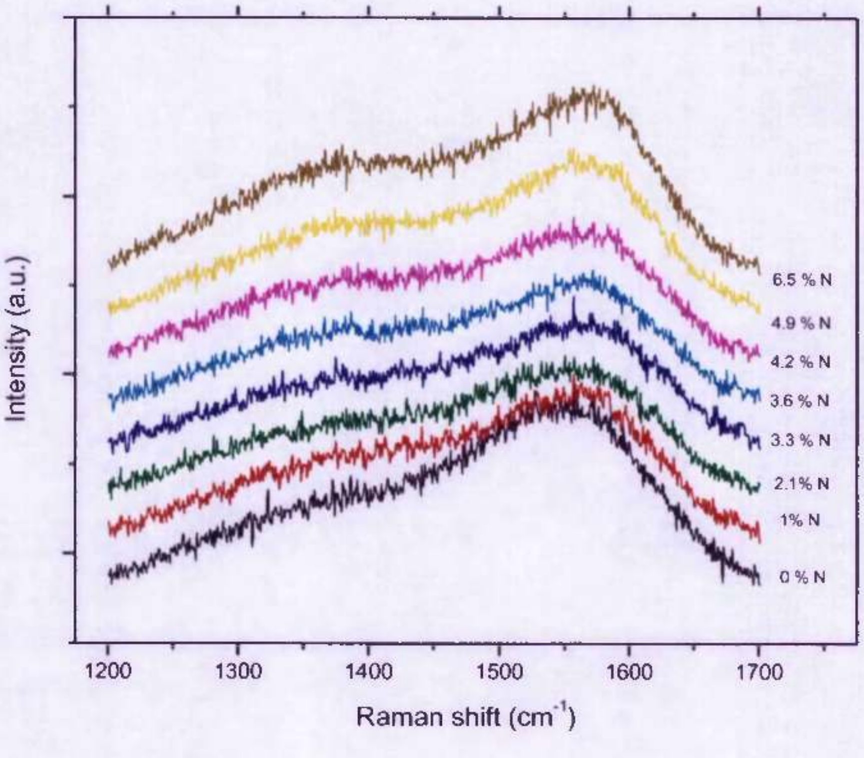

Figure 5-6: Raman spectra for a-C:H:N deposited with different Nitrogen concentrations.

Figure 5-7 shows the variation of (a) shifts in the *D* peak position, (b) *D* peak full width half maximum (FWHM), (c) shifts in the *G* peak position and (d) *G* peak FWHM. Shifts in the peak position are usually associated with the structural change in the sp^2 sites for both *G* and *D* peaks. The narrowing of FWHM can be interpreted as the increase in sharpness of peak intensity. It can be seen from Figure 5-7 (a) that there is no significant changes in the *D* peak position and in Figure 5-7 (b) that there is no significant changes in the *D* peak FWHM. This implies that increase in N content did not induce large variation in the sp^2 six-fold aromatic ring configuration. In Figure 5-7(c), the *G* peak shift is more significant as the peak gradually and significantly increases as the N content increases. Figure 5-7 (d) also shows similar variations in the sharpness of the *G* peak intensity as N content increases. The position of the *G* peak is sensitive to both ring and chain configurations, therefore the Raman spectra suggests that the increase in N content induces structural change in the sp^2 sites mainly involving chain-like configurations.

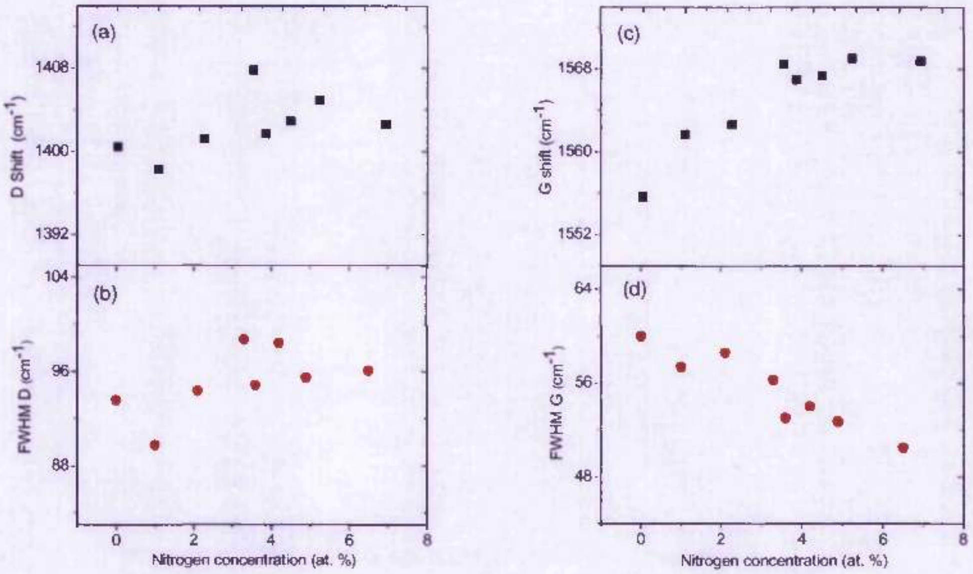

Figure 5-7: (a) shift in the D peak position and (b) FWHM of the D peak, (c) shift in the G peak position and (d) FWHM of the G peak. All variations are as a function of nitrogen.

The Raman results can be quantitatively analysed by studying the ratio of *D* and *G* peak intensity, I(D)/I(G). The I(D)/I(G) ratio is related to the ordering of the sp^2 phase and is not a quantitative measure of the sp^2 fraction. Based on the model proposed by Ferrari and Robertson [72], visible Raman is primarily dependent on the ordering of the sp^2 phase and I(D)/I(G) is related to the sp^2 cluster size. In amorphous carbon, where the disorder is high and carbon cluster size is small, the cluster size is estimated in the range of 1-2 nm. The ratio of I(D)/I(G) can be correlated to the generic in plane correlation length (L_a) of the sp^2

aromatic ring clusters. It was proposed by Ferrari and Robertson that L_a is equivalent to the size of the aromatic clusters. Figure 5-8 shows the variation of (a) I(D)/I(G) and (b) L_a as a function of the N content.

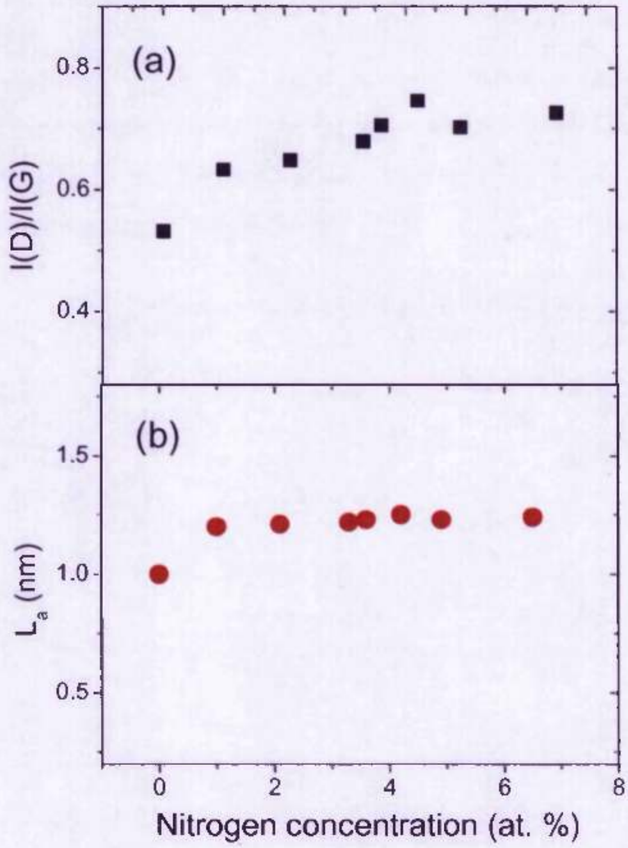

Figure 5-8: Variation of (a) Raman I(D)/I(G) ratio and (b) in-plane correlation length (L_a) of sp^2 aromatic clusters.

It can be seen that as the N content increases from 0 to 7 *at.* %, I(D)/I(G) increases from 0.54 to 0.79. This indicates that there is a structural change induced by nitrogen incorporation. However, the size L_a of the aromatic rings did not vary significantly and remains within 1 to 1.3 nm range. This result shows that the structural change by nitrogen is related to chain like configurations that is in agreement with the previous analysis.

5.3.3 Field emission analysis

The variation of (a) threshold field and (b) π bonds (sp^2 concentration) is shown in Figure 5-9. The sp^2 concentration is determined by EELS measurements as described in the previous section. It is interesting to see that as the N concentration increases from 0 to 9 *at.* %, both the threshold field increases from 18 V/μm to about 32 V/μm and sp^2 concentration increases from 42 to ~ 47 *at.* %. This is different from the results observed in section 5.2, where the threshold field decreases as the sp^2 concentration increases. This result suggests that the variation in threshold field is likely to be affected by the structural change in the sp^2 configuration as well as the "doping" effect. But, in these films, there is the additional "Nitrogen" factor that needs to be considered.

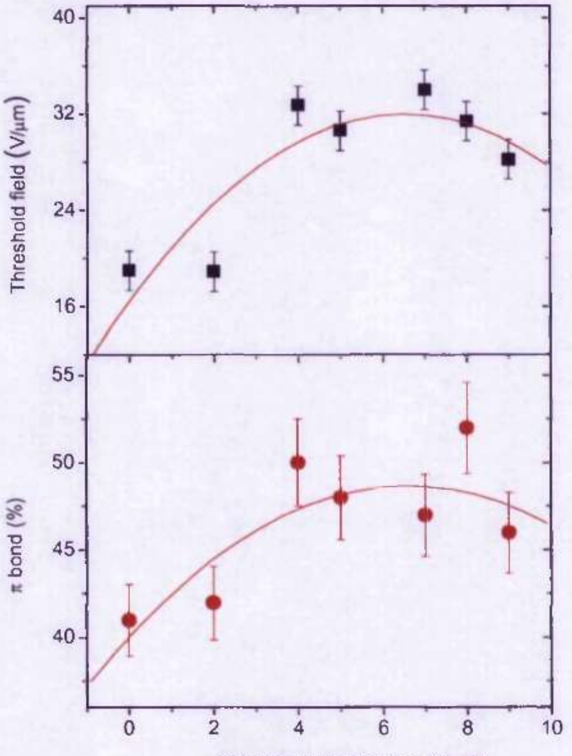

Figure 5-9: Field emission threshold field and (b) sp^2/sp^3 concentration as a function of the N concentration. The solid lines are quadratic fit for the data.

It is interesting to note the decrease (quadratic) in resistivity as a function of nitrogen, despite the band gap remaining constant in these GAC films. What this indicates is that there is competition between doping and sp^2 content states despite the sp^2 size not changing. Field emission on the other hand does not benefit from N inclusion, where the addition of nitrogen gives rise to isolated and smaller sp^2 clusters which result in an increase in the emission threshold fields. In the work by Ilie *et al.* [16] a series of nitrogenated TAC (TAC:N) films were subjected to post-deposition thermal annealing from 50-1000 °C. A clear *D* peak appears at 400 °C and then gradually evolves at higher temperatures. It was proposed that as the temperature increases, gradual clustering of the sp^2 states occurs. This is associated with the monotonic increase of I(D)/I(G) with annealing temperature as the sp^2 content evolves from chain-like to ring-like configurations. The field emission threshold fields were shown to vary with I(D)/I(G).

5.3.4 Summary and discussions

From the proposed field enhancement model using two conductive spheres discussed in Chapter 2, the sizes of these spheres are very important. This suggests that if the sp^2 phase contains a variety of ring-like rather than chain-like configurations, it would be more beneficial to fit this model. Interestingly, it has been proposed that nitrogen incorporation is more likely to induce chain-like configurations due to N acting as a termination stage to the sp^2 phase. This would imply that the conductive sp^2 phase is mainly composed of small chain-like configurations embedded in the sp^3 matrix when N prevents the evolution of large aromatic clusters. Therefore, it would be reasonable to attribute the increase in threshold fields with nitrogen incorporation to the lack of large aromatic sp^2 phase and possibly the nitrogenated a-C:H film being too conductive for there to be field penetration.

5.4 Surface treated amorphous carbon thin films

The field emission properties of a-C:H and a-C:H:N films subjected to C_{60} ion implantation are investigated as a function of ion dose. The aim of this experiment is to study the effects of surface modified amorphous carbon thin films on their field emission properties. C_{60} is an excellent choice as an ion source material. It is a large carbon molecule that is likely to modify the film surfaces on impact rather than penetrating through the carbon thin films.

Results suggest that C_{60} implantation induces a rich conductive sp^2 region at the surface that takes place during the implantation.

5.4.1 Experimental detail

These films are deposited on the earth electrode of a rf-PECVD system. Films are deposited on n-Si substrates at room temperature using feed gases of CH_4 (30 sccm), He (75 sccm) and N_2 (10 sccm). These films are implanted with C_{60} ions at 10 KeV with doses of 7.5×10^{13}, 1.25×10^{14} and 2.65×10^{14} cm^{-2} using a Danfysik ion implanter.

5.4.2 Field emission analysis

The variation of threshold field for a-C:H and a-C:H:N thin films as a function of the ion dose is shown in Figure 5-10.

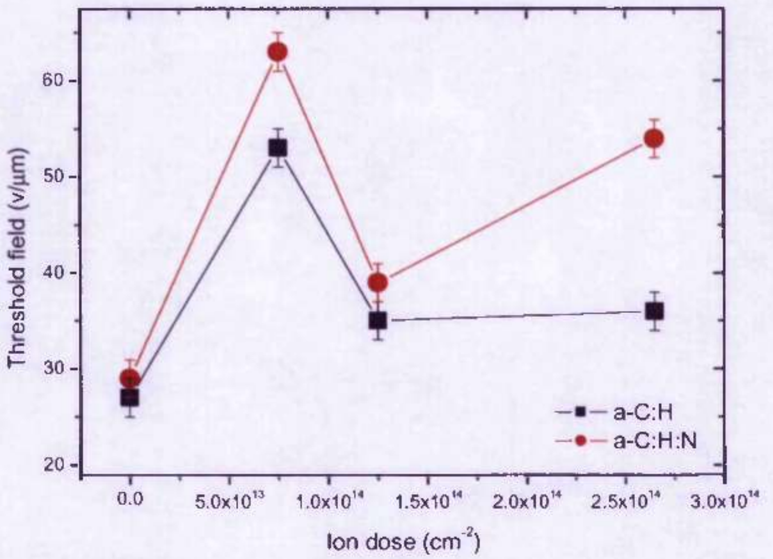

Figure 5-10: Variation of threshold field as a function of C_{60} ion dose for a-C:H and a-C:H:N films. The data at zero dose corresponds to unimplanted films.

The threshold field for the a-C:H film initially increases from 27 to 53 V/μm as the ion dose increase from 0 to 7.5 x 10^{13} cm^{-2}. However, at higher doses of 1.25 x 10^{14} and 2.65 x 10^{14} cm^{-2}, threshold fields decrease to 35 and 36 V/μm respectively. For the nitrogenated films, the threshold fields follow a very similar trend to the non-nitrogenated films. The threshold field initially increases from 29 to 64 V/μm when the ion dose increases from 0 to 7.5 x 10^{13} cm^{-2}, and then decreases to 40 and 53 V/μm at higher doses of 1.25 x 10^{14} and 2.65 x 10^{14} cm^{-2} respectively. Interestingly, the refractive index that is a measure of the density of the films shows a densification of the films at high doses. Figure 5-11 shows that as the ion dose increases to 2.65 x 10^{14} cm^{-2}, the refractive index increases from 1.58 to 1.77. Unfortunately, at the highest dose, the refractive index for the a-C:H:N film cannot be reliably determined due to sputtering that thins the films. The observed refractive index (1.77) at high dose is very close to that of a sp^2 rich graphite (1.8) which suggests that graphitisation of the surface may have taken place.

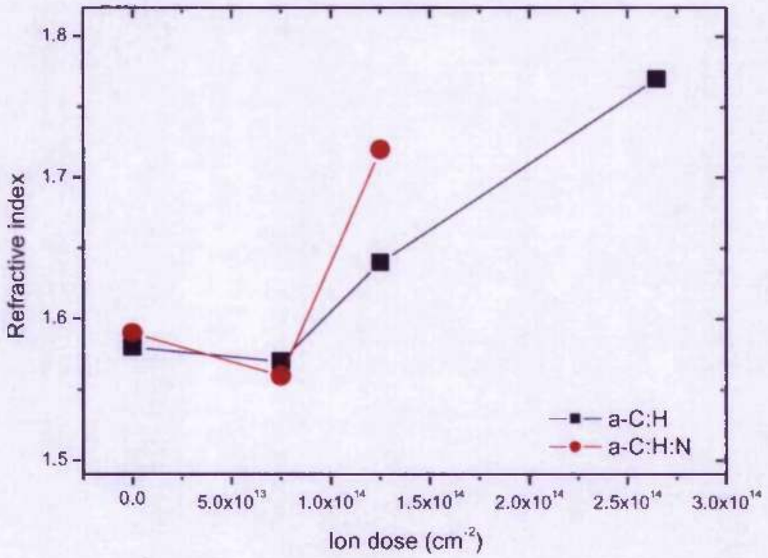

Figure 5-11: Variation of refractive index as a function of C_{60} ion dose for a-C:H and a-C:H:N films. The data at zero dose corresponds to unimplanted films.

5.4.3 Summary and discussions

Molecular dynamic simulations indicate that a 10 KeV C_{60} ion will on average penetrate 3.5 nm into an a-C:H film and will not significantly affect the bulk electronic properties. It is envisaged that the C_{60} on impact will break into sp^2 rich phases that will form on the film surface. This would create a conductive sp^2 rich layer on the surface which screens the electric field and prevents field penetration into the film. Therefore, the field emission characteristics will be similar to that from a flat metal or graphite sheet. It is therefore expected that the field emission threshold will increase after C_{60} implantation. This result is in agreement with the field enhancement model based on inhomogenity of the carbon configuration [18] and the space charge induced band-bending model [10]. By creating a sp^2 rich layer on the surface of the film, the effects of dielectric mismatch are no longer significant, and hence internal field enhancement cannot be efficient. Also, due to field screening at the surface, there is no field penetration into the carbon thin film, hence, hot electron type emission cannot be induced. It is interesting to note that as the ion doses increase to higher doses of 1.25×10^{14} and 2.65×10^{14} cm^{-2}, the threshold fields starts to reduce. This can be explained due to the increase in sputtering on the film surface, and hence a thinner graphitic layer is formed as well as the possibility of ion tracks being formed in the a-C:H thin film. Therefore, a reduced electric field screening.

In summary, we have studied the effects of surface modification by C_{60} implantation. C_{60} ions induce a conductive sp^2 rich layer on the surface upon impact. This results in the increased threshold electric field for electron field emission caused by electric field screening at the film surface.

5.5 Summary

In this chapter, we have looked at the field emission properties of a-C:H films with Ar dilution, N inclusion and surface modification. The main constraint in manipulating the field emission properties is the lack of understanding of the optimum concentration and size of the sp^2 phase. The effects of Ar dilution have shown that by modifying the plasma chemistry, higher sp^2 concentrations and lower emission threshold fields can be obtained. However, N inclusion in a-C:H films shows that even if a high sp^2 concentration can be obtained with nitrogen, the size and configuration of these sp^2 phase is also very important. Small chain configurations do not benefit the electron emission process. Finally, we have shown having a thin sp^2 rich layer on the surface of the a-C:H films does not improve the field emission properties. Results indicate that field screening at the film surface increases the threshold field. Therefore, it can be summarised that the sp^2 plays an important role in the field emission properties in a-C:H films. An optimum configuration in terms of the quantity, size and configuration needs to be provided for the best quality a-C cathodes to be produced.

Chapter 6

6 Field emission properties of nanostructured graphite-like amorphous carbon films

6.1 Introduction

In this chapter we will examine the field emission properties of the a-C films and study the variation of intrinsic stress on the field emission properties. The intrinsic stress is usually accompanied with high film density and can therefore be an important influence on the field emission. High intrinsic stress would result in the carbon sp^2 sites within the film being closer together which may increase the field enhancement due to the proximity effect discussed in Chapter 2.2.4.

6.2 Experimental conditions

The a-C films were deposited by an Ion Beam Assisted Deposition (IBAD) technique using two Kauffman ion sources. Neon, Argon, and Krypton gases were, respectively, introduced in both Kauffman sources, one for the sputtering of a graphite target and the other for the simultaneous assisting of the growing film. This enabled independent control of the deposition species and the ion flux used to transfer momentum to the growing film surface. All films were prepared at 150 °C applying an ion beam assisting energy in the range 0 to 800 eV. After the deposition, the samples were transferred, under vacuum, to the UHV chamber (pressure $<10^{-7}$ Pa) for *in situ* photoelectron spectroscopy measurements (XPS and UPS). No oxygen was detected. The macroscopic density was determined by Rutherford backscattering spectroscopy (RBS). Electron energy loss spectroscopy (EELS) was also performed to obtain the plasmon loss and the concentration of sp^2 sites using a Philips CM 20 microscope with an imaging Gatan PEELS system. Stress measurements were performed using films deposited on c-Si bars, applying an optical bending beam method to determine the radius of curvature of the film/substrate composite [73]. The film thickness was about 100 nm. The field emission (FE) characteristics of these films were determined using a sphere-to-plane technique. The anode in this case is a 5 mm stainless-steel ball bearing separated from the film surface at a gap of 20 μm in a vacuum better than 4 x 10^{6} mbar. Conditioning of the films was observed as reported elsewhere [74], where a relatively high initial electric field is required before further stable measurements are recorded. The threshold field (E_{th}) is defined as the microscopic electric field where an emission current of 1 nA is observed.

6.3 Structural analysis

Amorphous carbon (a-C) has a more complex system than its group IV counterparts such as amorphous silicon since C atoms can exhibit sp^3, sp^2 or sp^1 hybridisations. In the hydrogen free a-C films, the mechanical and electronic properties are very much controlled by the composition of the sp^3 and sp^2 concentrations. It is therefore essential to understand the fundamental presence of both σ and π bonding in the films.

To investigate the degree of sp^2 and sp^3 bonding in these a-C films, structural analyses were performed. Figure 6-1 shows the Raman spectrum of the a-C film prepared with Ar^+ assisted at 400 eV. The spectrum obtained is fitted into two distinct Gaussian contributions; the disorder (D) band (~1340cm^{-1}) and graphite (G) band (~1540 cm^{-1}). The ratio of the two bands, I(D)/I(G) gives the structural information of the sample. All films exhibit a I(D)/I(G) ratio of ~2, this value is higher than the typical value of TAC films of ~0.1.[75] The Raman spectra depend primarily on the ordering of the sp^2 sites but not on the fraction of the sp^2 sites. The I(D)/I(G) ratios can vary even if the sp^2 concentration remains constant since it is proportional to the ordering in the cluster. Therefore, in contrast to TAC films, these films with I(D)/I(G) ratio of ~2 indicate the presence of highly ordered sp^2 clusters.

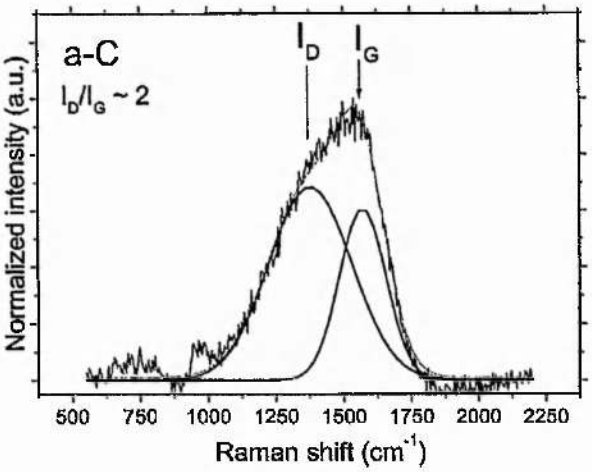

Figure 6-1: Typical Raman spectra of a-C film prepared under argon assisting energy of 400 eV.

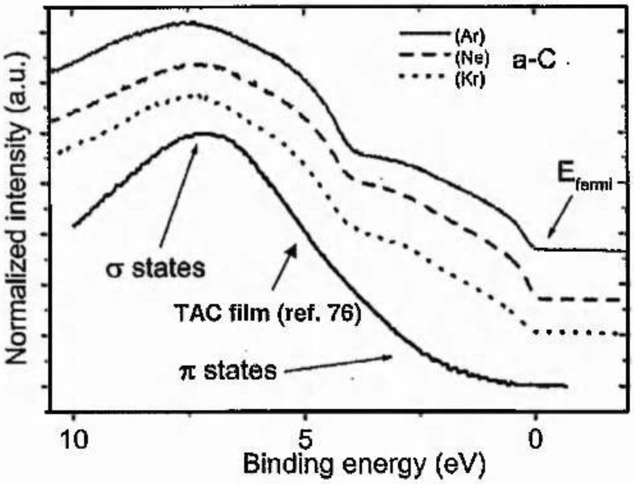

Figure 6-2: Valence band spectra UPS (He II) of a-C films prepared by IBAD using Ne, Ar, and Kr as working gases. The top of the valence band of a TAC film (Ref. 76) is also included for comparison.

Figure 6-2 (relative to the top of the valence band) shows the UPS spectra of films prepared with three different noble gases. A shoulder at the top of the valence band (0-4 eV) is a clear indication of the presence of a high C-C π bond fraction in the films. The absence of a band gap in contrast to TAC shows the predominant presence of sp^2 sites in the material. These characteristics are in agreement with the high values of sp^2 bonds (~ 90%) obtained from EELS, for all samples.

Electrical measurements on the sheet resistivity (R_s) of these films indicate that the films get more conductive when the assisting energy is increased. This trend is observed in all the films with different noble gases. Figure 6-3 shows the variation of sheet resistivity of all the films as a function of the assisting energy with different noble gases. It is important to note that the measured sheet resitivity is similar to that of graphite sheets in the c-axis plane which is about $1 \times 10^{-3}\,\Omega$ cm.

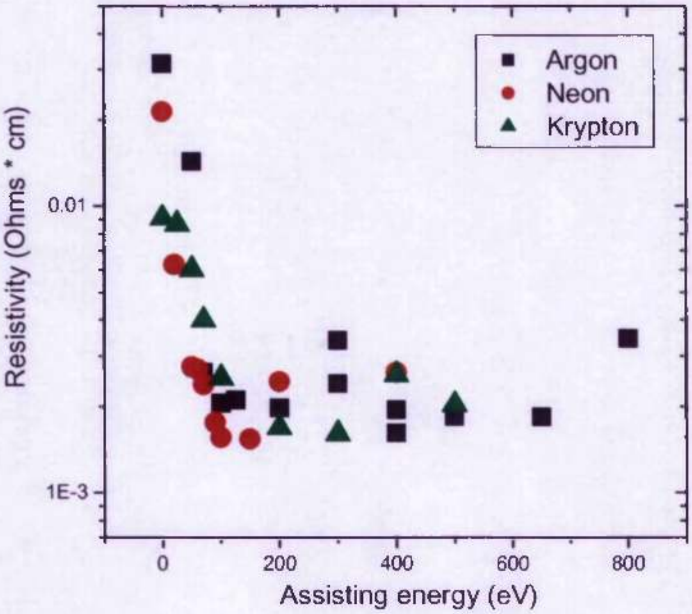

Figure 6-3: Sheet resistivity as a function of the assisting energy for Ar, Neo and Kr assisted films.

6.4 Intrinsic stress and carbon densities

One of the interesting properties of a-C films is that they possess a relatively high intrinsic stress within the material. The mechanisms for generating such a high intrinsic compressive stress has been explained due to the energy of the ion bombardment during the deposition process causing a sp^2 to sp^3 bonds transition when a critical stress of ~5 GPa is maintained within the film. [77,78] The sub-implantation model, which states that in the presence of ion bombardment formation of sp^2 and sp^3 bonds just below the growing surface is now well accepted.[79,80] Also Robertson *et al.* [80] suggested that the origin of stress could be due to the densification of the film by the sub-implantation process. The densification is mainly due to the presence of high sp^3 bonds. Recent studies have shown that it is possible to produce a-C thin films with high sp^2 concentrations that exhibit local density, hardness and intrinsic stress similar to those of TAC films.[81] These have been attributed to the densification of the film during the "knock-on" process of the carbon atoms beneath the surface. The densification of the carbon film occurs in relation with the reduction of the distance between sp^2 clusters. From a tribological viewpoint, high stress is undesirable due to adhesion problems with the substrate. However, it is well known that the electronic properties of carbon-based materials change when the carbon phase is under high pressure/stress. Reports have shown that amorphous carbon under high pressure can result in an increase in the film conductivity. [82] By applying pressure to a material one can modify its electronic properties, e.g., band structure, resistivity, Fermi level. [83,84] It is therefore important to study the macroscopic and microscopic density of the films since they give indications on the densification within the films. The carbon macroscopic density of these films was determined by Rutherford backscattering spectroscopy (RBS). However, in order to probe the local/microscopic density, the plasmon energy was measured by XPS. The plasmon energy peak is a measure of the inelastic scattering of the C 1s electrons before leaving sample. The plasmon energy is related to the mass density assuming a free electron model with the plasmon energy proportional to the square root of the effective valence electron density. The densities obtained by this method are known to overestimate the real value. [85] In this work, we will not be determining the real electronic density but investigating the relative variation of local density to the assisting energy.

The macroscopic density measured by RBS is shown in Figure 6-4. The results show that between 100 to 500 eV, the films have an average density of about 2.3 g/cm^3. This value is relatively lower than highly tetrahedral TAC films that have a reported densities of about 3 g/cm^3. [86] However, this value is similar to graphite that suggests that these films may contain highly ordered graphitic structures. This result also indicates that there is no significant dependence between the assisted noble gases and the curves remain relatively similar. It is important to note that this result is different from those reported by Andre *et al.* which show a decreasing density at 200 eV [87]. This however can be explained by the low values of ion/C flux ratio of <0.2 used in their work [87] compared to ~1.8 in this work. The lower density observed in the lower (<100 eV) and higher (>500 eV) energy can be explained by the presence of voids within the films.

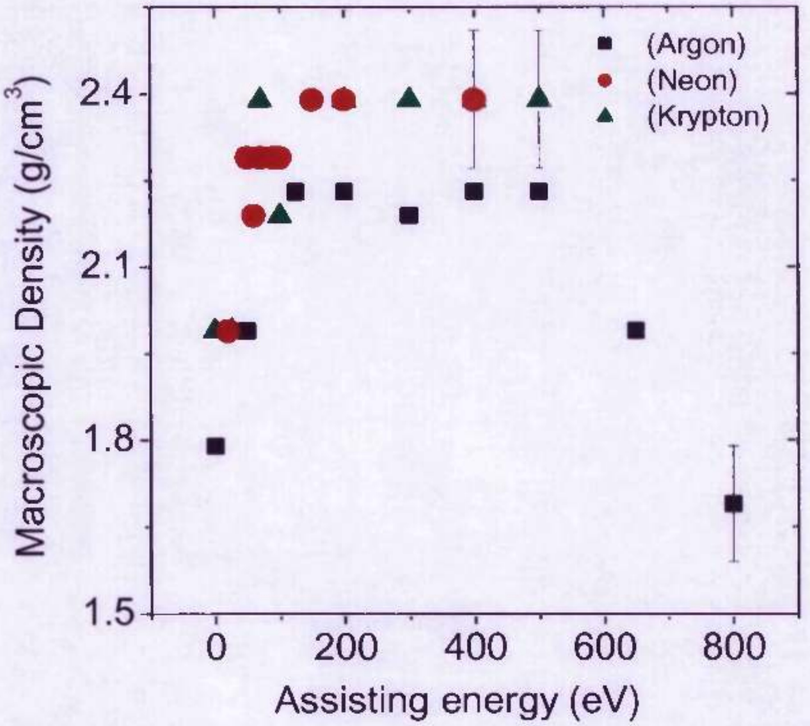

Figure 6-4: Macroscopic density of a-C films as a function of the noble gases assisting energy.

The plasmon energy as a function of the assisting energy which corresponds to the local/microscopic density is shown in Figure 6-5. The plasmon energy increases significantly with an increase in the assisting energy up to 100 eV. For the Ne$^+$ assisted films, maximum plasmon energy of 28.7 eV is observed at 100 eV. However, the maximum plasmon observed for the Ar$^+$ and Ne$^+$ is at 400 eV and 300 eV with plasmon energy of 29.5 eV and 29.1 eV respectively. This indicates a modification to the local density, which is similar to the macroscopic density from RBS.

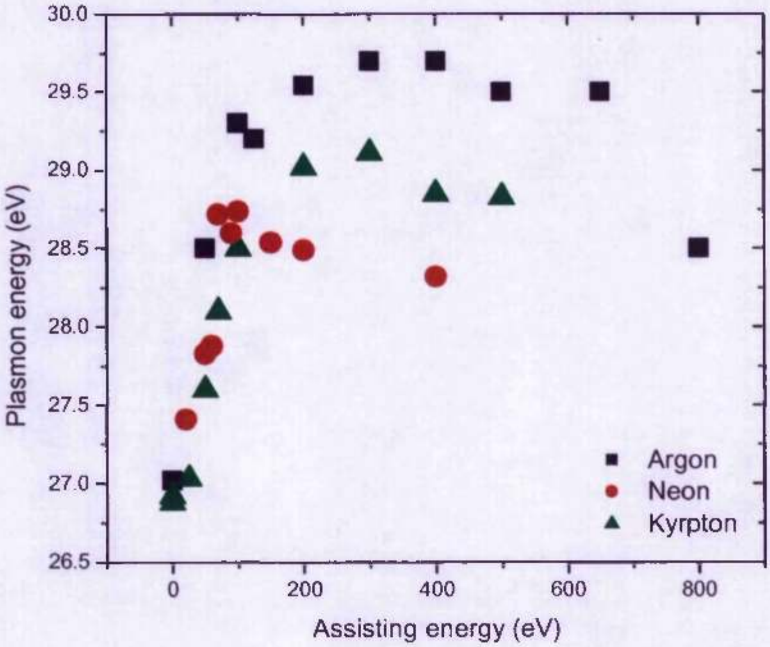

Figure 6-5: Plasmon energy as a function of the assisting energy of noble gases.

The intrinsic stress as a function of the assisting energy is shown in Figure 6-6. The amorphous carbon film shows a variation of the intrinsic stress when different assisting ions are used and there is a dependence of the assisting energy on each species. For Ne^+ assisted films, the intrinsic stress increases as the energy increases up to 100 eV, where a maximum intrinsic stress of 9.1 GPa is observed. At a higher energy the stress value falls to 4.2 at 400 eV. The films deposited with Ar^+ and Kr^+ show a similar trend to that of the Ne^+ assisted films. The intrinsic stress increases to about 13.5 GPa and 11.7 GPa respectively before decreasing at increasing energy.

It is interesting to note that the intrinsic stress and plasmon energy show a similar dependence on the assisting energy. This shows good agreement that the films are made up of a highly compressed carbon network.

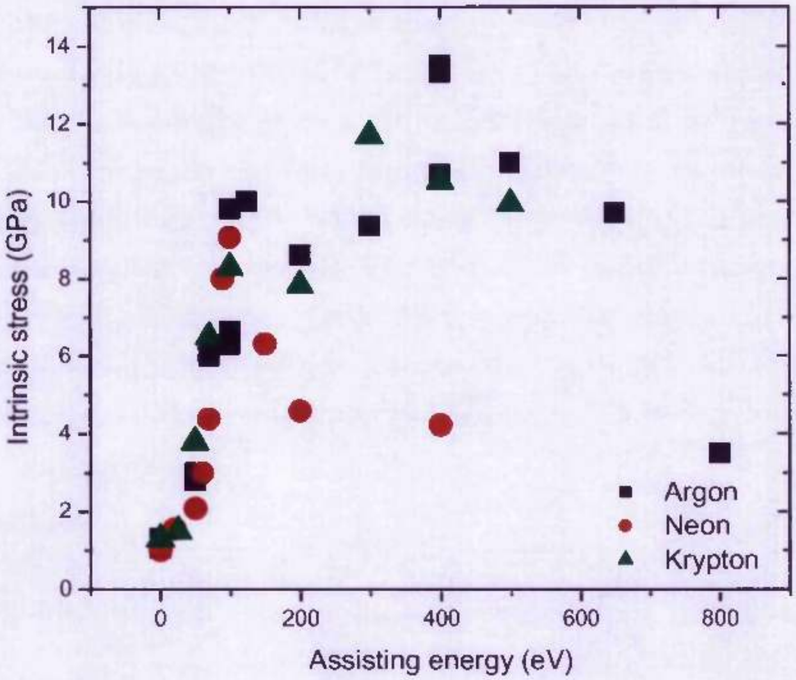

Figure 6-6: Intrinsic stress as a function of the assisting energy.

6.5 STM and TEM investigations

STM measurements were performed for films as a function of the intrinsic stress. The STM measurements are raster scanned across the film surfaces to study the variation in tunnelling current over an area of 5 μm^2. Variations in the tunnelling current can be used to probe the conductivity and also the ease of electrons tunnelling through the barrier. Figure 6-7 shows the STM topography of the samples, (a) 0 eV, (b) 75 eV, (c) 400 eV and (d) 650 eV. Highly conductive nanostructures are observed on the surface of these films. The shape and sizes of these nanostructures are very dependent on the assisting energy of the Ar gas. In the case without assisting energy, the nanostructures are small and randomly located. As the assisting energy increases at 70 eV, the nanostructures become more ordered and bigger. At assisting energies of 400 eV, the density increases and these nanostructures become well aligned. A similar result was reported by Schwan *et al.* for their GAC films when subject to high intrinsic stress.[78] However, with increasing energy at 650 eV, the bombardment of assisting ions are too energetic hence leading to the nanostructures becoming smaller. An analysis of Fig. 6-7 (c) shows that the nanostructures at a high assisting energy are well aligned and dense due to the intense Ar^+ ions introduced during growth. It is possible that the stress within the sp^2 rich segments also causes some of the contrast seen in these films by altering the band structure of the nanostructured graphite. On the other hand, when no assisting is present, Figure 6-7 (a) shows that the formation of these nanoclusters are random, less conductive and smaller when compared to those with assisting energy ion bombardment. The highly conductive nanostructures agrees well with the R_S (0.09 Ω-cm) measurements and also supporting the sp^2 character of the films. It should be noted that highly comparable values of R_s to those of graphite in the disordered nanostructured material adds further credence to the view that electron density increases must be taking place microscopically in the sp^2 rich clusters.

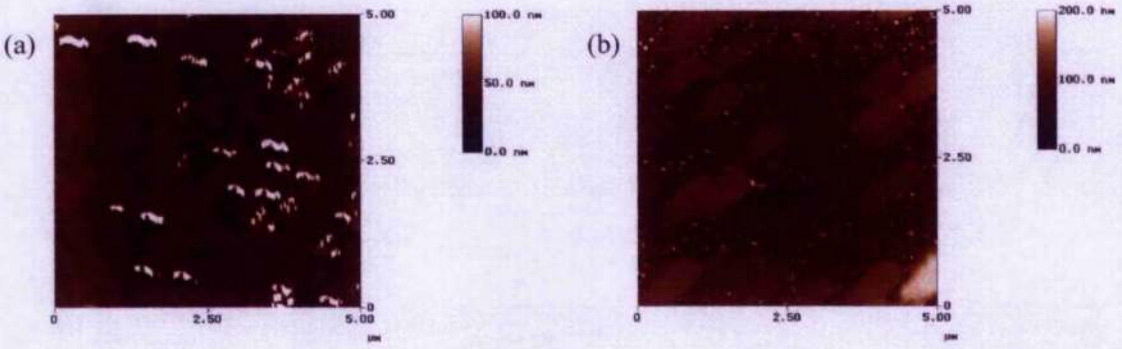

0 eV - 1 GPa

70 eV - 6 GPa

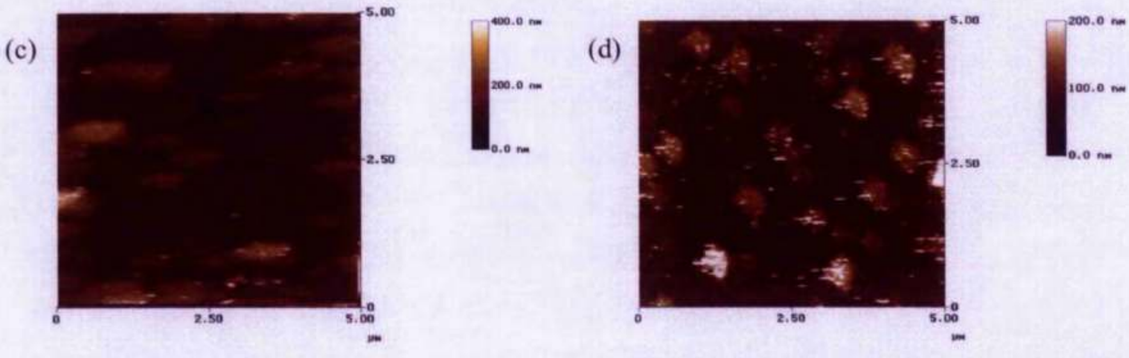

400 eV - 12 GPa

650 eV - 9.7 GPa

Figure 6-7: STM micrographs at ion energies of (a) 0 eV, (b) 70 eV, (c) 400 eV and (d) 650 eV.

Looking at the individual structures in details, the STM images are shown in Figure 6-8 for (a) 0 eV, (b) 400 eV and (c) 650 eV. It is interesting that in Figure 6-8(a) there is no distinct nanostructure found within these islands where the carbon phase are found to be solid and in the bulk. At 400 eV, there are nanostructures of the order of about 70 nm found within the island structure. These ordered nanostructures are closely packed together with a separation distance of a few nanometres. There are also smaller structures that are of the order of a few nanometres. These nanostructures are believed to be the sp^2 type clusters, mainly because they are more conductive than the surrounding. As the assisting energy increases to 650 eV, the nanostructures are found to be larger in dimension and mostly joined together.

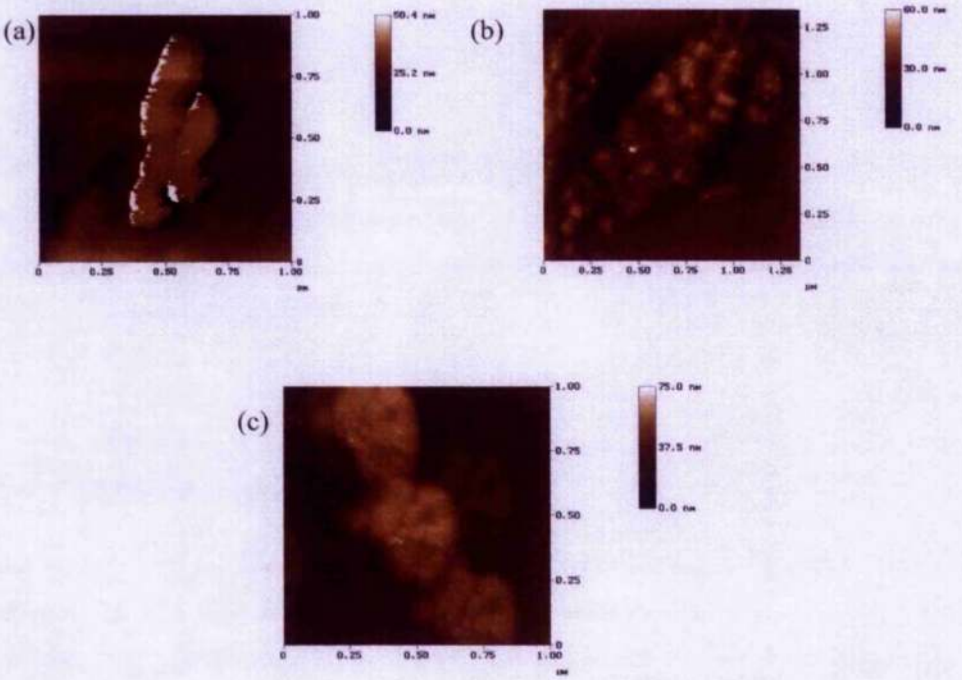

Figure 6-8: STM images of the individual structure of for (a) 0 eV, (b) 400 eV and (c) 650 eV. (see Figure 6-7)

Further TEM results show these GAC films contain crystalline nanostructures embedded in an amorphous matrix. Figure 6-9 shows the TEM images. The interference fringes of 3.2 Å suggest that the crystalline region is composed of graphitic nature, similar to the c-axis of a single crystal graphite plane. Figure 6-9 (b) is a close up view of figure 6-9 (a).

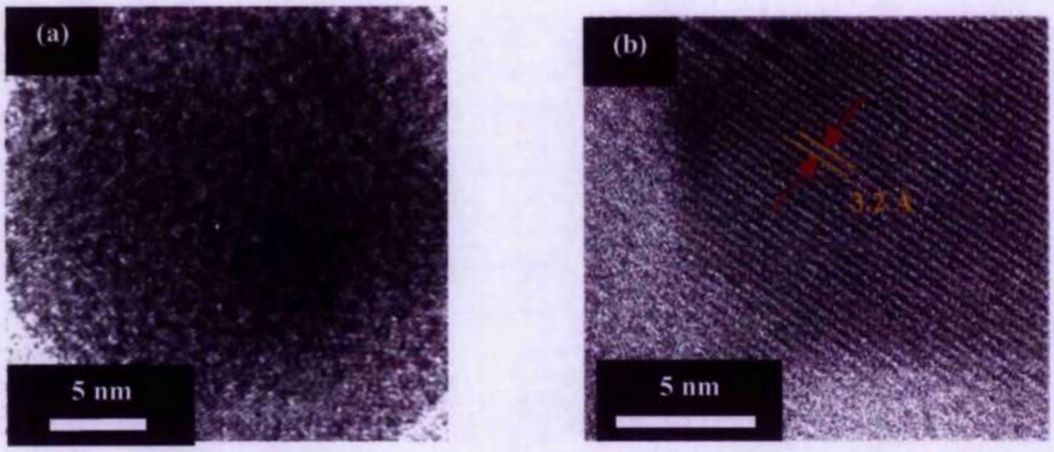

Figure 6-9: HRTEM micrograph of the 400 eV Ar assisted film.

The sizes of these nanostructures from TEM are of the order of about 60 nm in size. This is in agreement to the STM investigation shown in Figure 6-8 (b). This further proves that the films contain highly ordered graphitic nano-structures, whose local electronic properties are very similar to those of graphite.

6.6 Field emission properties

The typical field emission characteristics measured using the probe technique are shown in Figure 6-10. The field emission curve exhibits a conditioning cycle in the initial run, which indicates that conditioning is required before stable measurements can be recorded. This requires the initial run to apply an electric field of up to 14 V/μm before the threshold field is observed at 7 V/μm. The field emission characteristic is analysed using the traditional F-N tunnelling by plotting Ln(I/E^2) vs 1/E. The F-N plot is shown in Figure 6-11, fitting a straight line to the plot indicates that the emission mechanism is mainly based on electron tunnelling through the vacuum barrier.

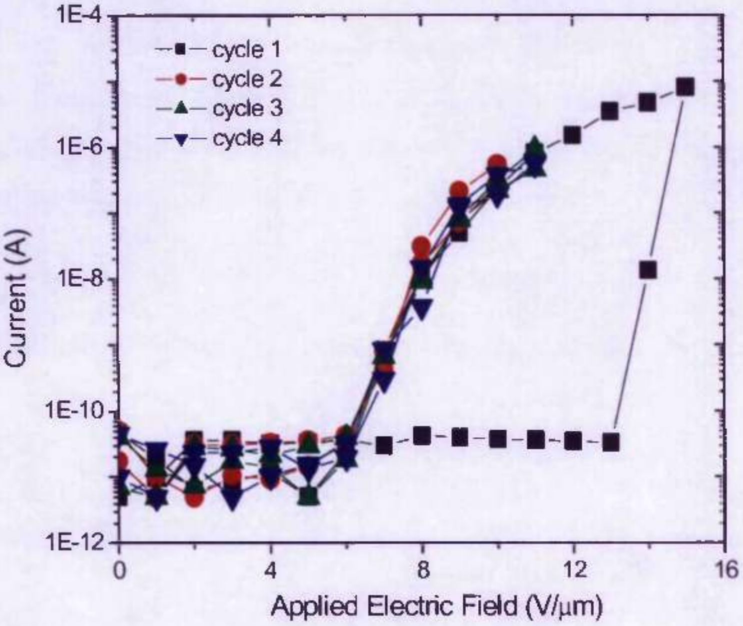

Figure 6-10: Field emission characteristic of a-C film deposited at 400 eV with Ar^+.

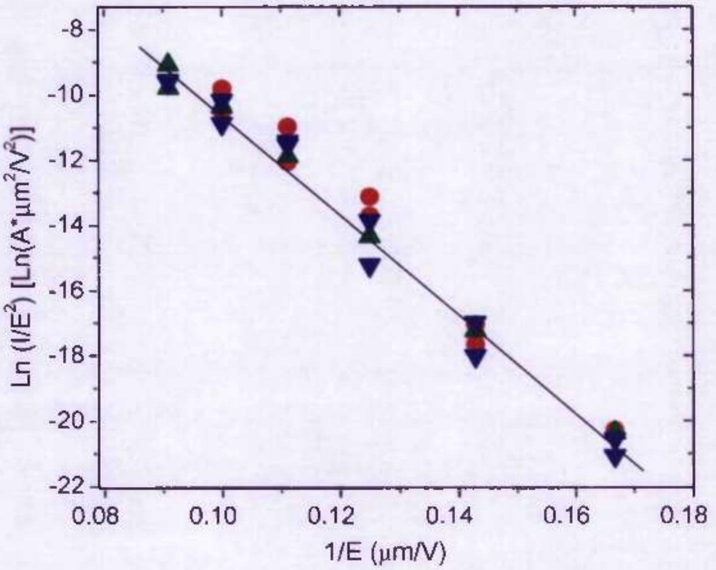

Figure 6-11: F-N plot extracted from Figure 6-6. A straight line fitting indicates the field emission is mainly dominated by F-N tunnelling.

The variations of E_{th} (threshold field) as a function of the assisting energy with different noble gases are shown in Figure 6-12. With no assisting energy, the threshold field reaches a value as high as ~50 V/μm. As the assisting energy increases, E_{th} decreases to values as low as 7 V/μm at an assisting energy of 400 eV (Ar). Further increases in the assisting energy result in the subsequent increase in E_{th} to about 38 V/μm at 800 eV.

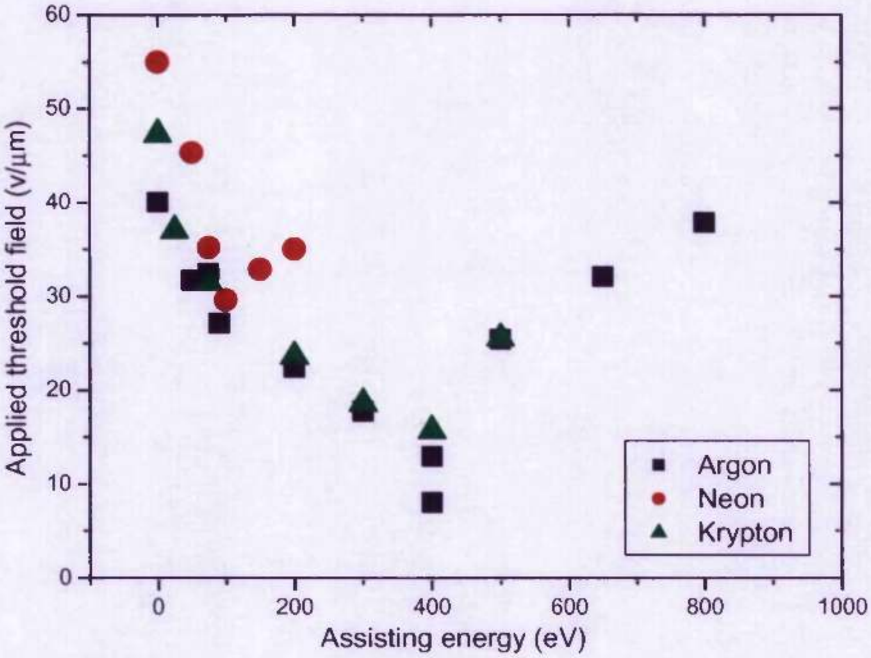

Figure 6-12: Threshold field as a function of the assisting energy for Ar, Ne and Kr assisted films.

The lowest E_{th} is observed in the film with the highest intrinsic stress (~12 GPa) and local electron density (plasmon ~29.5 eV). In addition, the dependence of the E_{th} with the assisting energy is also very similar to the dependence of the assisting energy with the stress of different noble gases. In general, all noble gases show a minimum E_{th} similar to the trend of the intrinsic stress. These results suggest that the intrinsic stress is controlling the field emission characteristics. Two possible effects could be responsible for this phenomenon.

1) Stress induces changes in the electronic structure of the nano-crystalline sp^2 structures. In fact ϕ, the barrier for electron emission at the surface, can be reduced due to "Fermi-level crossing" when the valence and conduction bands overlap.

2) The proximity effects of bringing the sp^2 clusters closer together due to stress could also enhance the emission process. There is also a possibility of both effects to be present in order to achieve the optimum emission characteristics.

For a better understanding of the FE characteristics of these films, surface morphologies have been investigated. Atomic Force Microscopy (AFM) was performed on films grown at 400 eV showing surface protrusions of around 50 nm in height and 150 nm in diameter. Based on the Fowler-Nordheim equation [4].

$$J = \frac{A(\beta E)^2}{\phi} \exp\left[\frac{-B\phi^{3/2}}{\beta E}\right]$$

where ϕ is the effective barrier height and β is the enhancement factor. J is the current density and E is the applied electric field. A and B are constants. Assuming the films have the effective barrier height ϕ of 4 eV (work function of graphite) and $\beta = \frac{h}{r}$, where h is the height of the surface feature and r is the radius, the enhancement factor at a surface can be estimated. Therefore, by calculating β directly from the F-N plot, an enhancement factor of 340 is obtained. However, if you calculate the enhancement factor based on the surface protrusion by using $h = 50$ nm, $r = 75$ nm, (and $\beta = h/r$) a β value of 0.66 is obtained, which is not a realistic value since β should greater or equal to 1. This value is about 500 times less than the calculated value from the F-N plot, assuming the emission is to be controlled by such a mechanism. Thus, since no realistic values can be obtained from surface field enhancement due to protrusions, the low threshold field observed in Figure 6-12 must be associated with a non-geometric field enhancement based possibly on the sp^2 clusters in the structure of the a-C film.

6.7 Simulation of two conductive spheres

We have investigated a system of conductive spheres with different radii embedded in an insulating medium supporting a uniform electric field. The field enhancement resulted from having two spheres in close proximity is shown to be controlled by the separation distance and conductivity of these spheres. This model can be used to explain the high field enhancement factor observed in a-C films during field emission. A model of two conductive spheres by Chaumet *et al.* [19] has been used to explain this close proximity effect. By moving two conductive (conductivity of gold) spheres close to each other at 1 nm an enhancement factor of up to 400 can be achieved. To study this effect, the classical problem of two spheres sitting in an electro-magnetic (E-M) field is studied using E-M simulation codes. Early work by Chaumet *et al.* [19] was based on highly conductive spheres, however, amorphous carbon does not posses such a high conductivity. In fact, a-C films generally posses much lower conductivity. Using Silvaco simulations, the distribution of the electric field around the spheres with different conductivity is studied.

Figure 6-13 corresponds to the electric field distribution between spheres with radius of R_1=5 nm, R_2=30 nm (ratio of 1:6) and separation distance (D_t)=5 nm. Both spheres are Silicon and the supporting medium is vacuum with a dielectric of 1. The spheres are undoped, hence resemble intrinsic semiconductors.

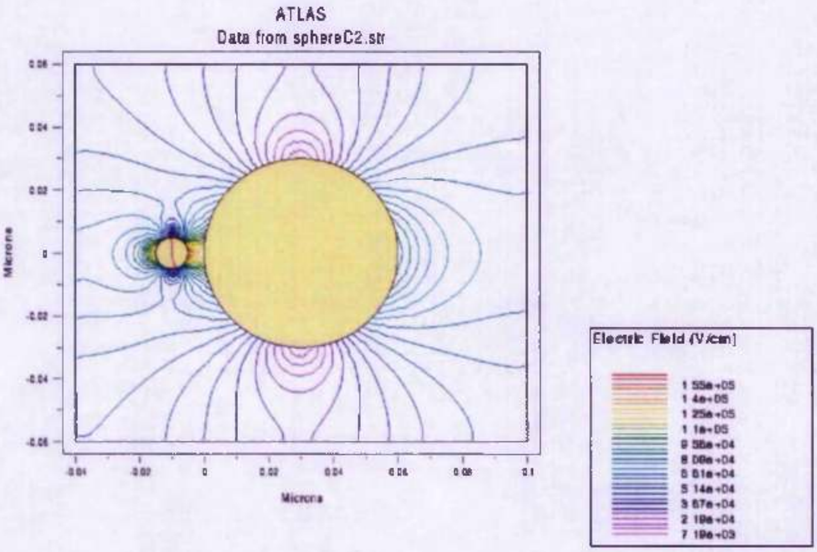

Figure 6-13: The contour lines of the electric field around spheres: R_1=5nm, R_2=30nm and D_t = 5nm. Applied field of 8.6 V/μm and an enhancement factor of 3.5. The maximum field is observed between the two spheres at 29.8 V/μm. The uniform electric field is applied in the X-axis direction.

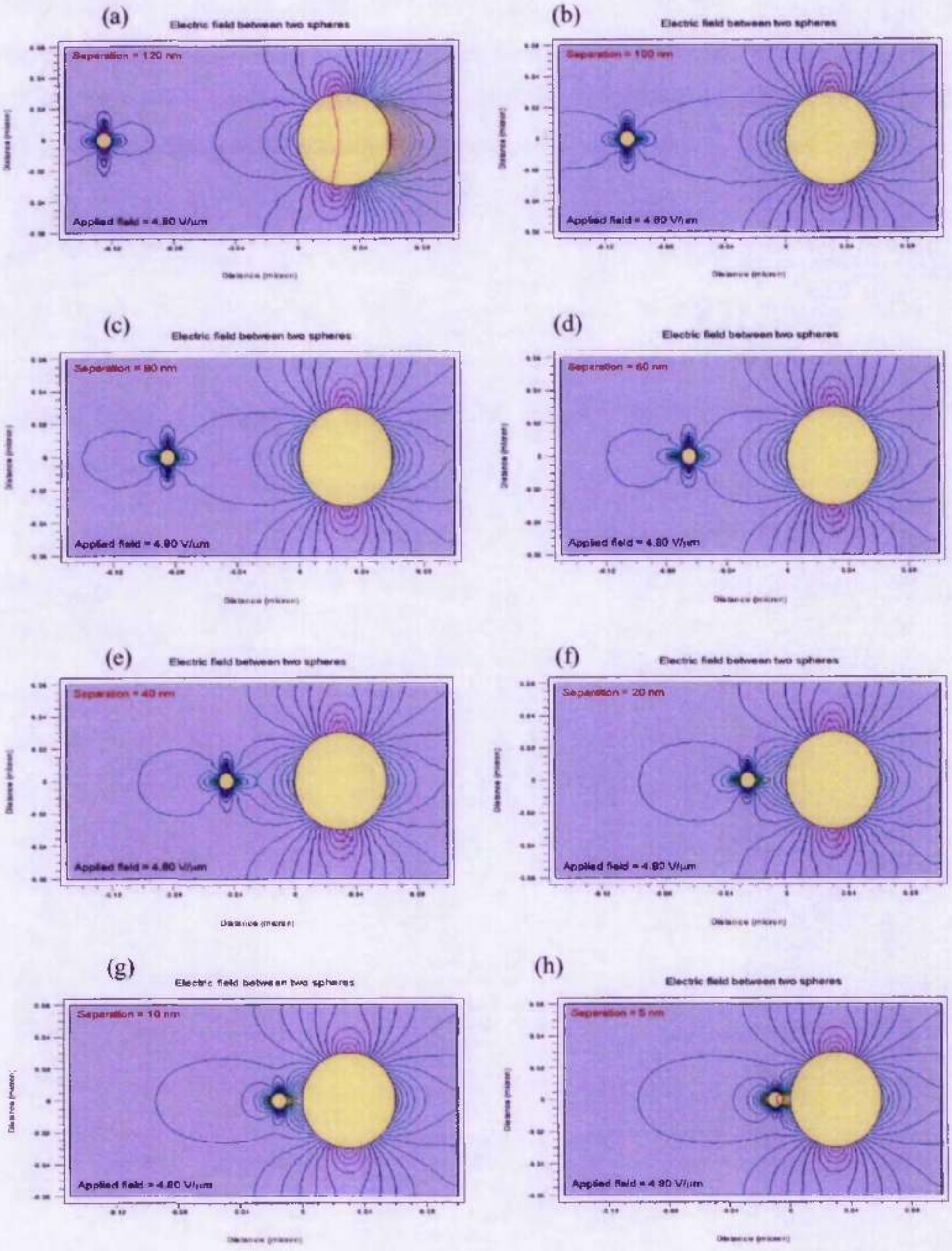

Figure 6-14: The variation of the electric field by reducing the separation distance. (a) 120nm, (b) 100nm, (c) 80nm, (d) 60nm, (e) 40nm, (f) 20nm, (g) 10nm and (h) 5nm. Enhancement factor of 3.5 can be observed when the separation distance is reduced to 5nm.

The applied field is biased across the vacuum in the x-direction, with an applied voltage of 1.2V across the 0.14 μm width of the box. The maximum electric field of 29.8 V/μm was observed in between the two spheres. This corresponds to an enhancement factor of 3.5. The electric field distributions are in agreement to those observed with the work from Chaumet *et al.* [19] Using the sample configuration as above, the D_t was varied from 120nm to 5nm. Figure 6-14 illustrate the effects of the electric field line when the distance is reduced.

The above results are simulated based on a sphere radii ratio of 1:6. In order to increase the enhancement, the sphere radii ratio is increased to a factor of 1:10. In figure 6-15 (c), the enhancement is increased from 3.5 to 4.9 by changing this ratio from 1:6 to 1:10 with the separation kept constant at 5nm. In figure 6-15 (a), the separation distance is further reduced 1nm which results in an increase of the enhancement factor to 8.6.

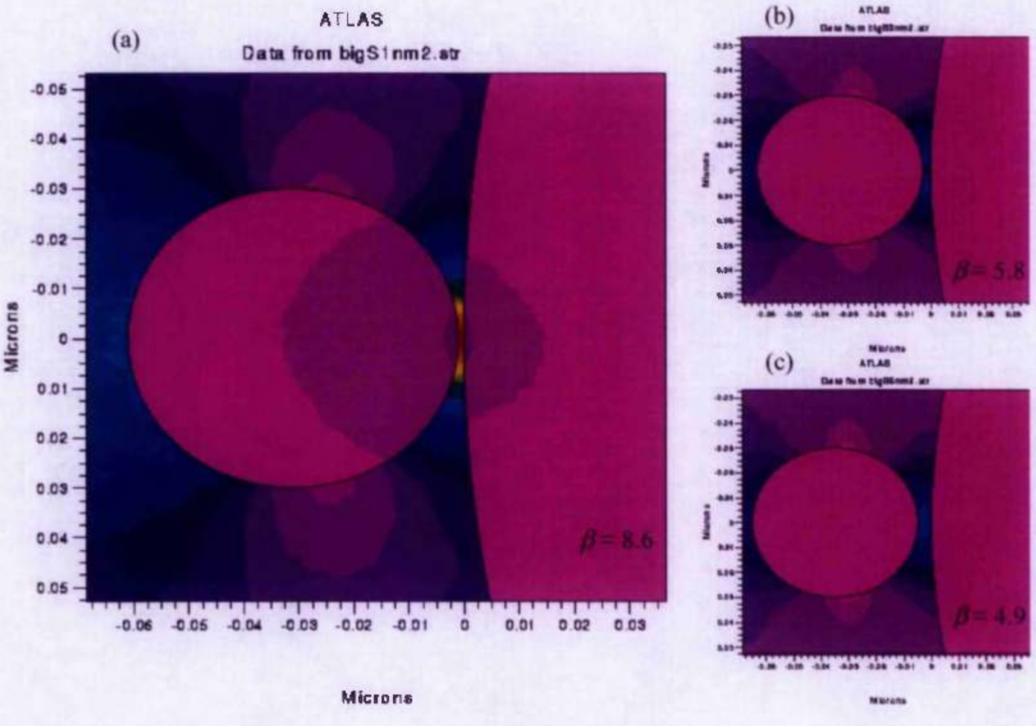

Figure 6-15: The effect of varying the distance between two spheres. R_1= 30nm, R_2= 300nm and (a) D_t=1nm, (b) D_t=3nm and (c) D_t=5nm. The enhancement factor falls from (a) 8.6, (b) 5.8 and (c) 4.9 respectively.

So far, the simulations have been carried out with undoped silicon spheres. According to Chaumet *et al.* [19] and Carey *et al.*, [18] the enhancement factor is controlled by the conductivity and also the separation distance. To investigate the effect of varying the conductivity of the spheres, the base impurity of the spheres was varied to change the resistivity.

Figure 6-16 shows the enhancement factor as a function of the resistivity of the spheres. The enhancement factor is shown to be related to the resistivity. As the resistivity is increased from 0.08 to 5.5 Ωcm, the enhancement factor increases from 3 to 15. However, when the resistivity is increased to 3000 Ωcm, the enhancement factor drops to 5.6. This illustrates, a screening effect, when the spheres are too conductive. This results in the electric field being disturbed, and hence unable to be applied uniformly across the spheres. The effect of having more conductive spheres results in the screening effect with a poorer field enhancement.

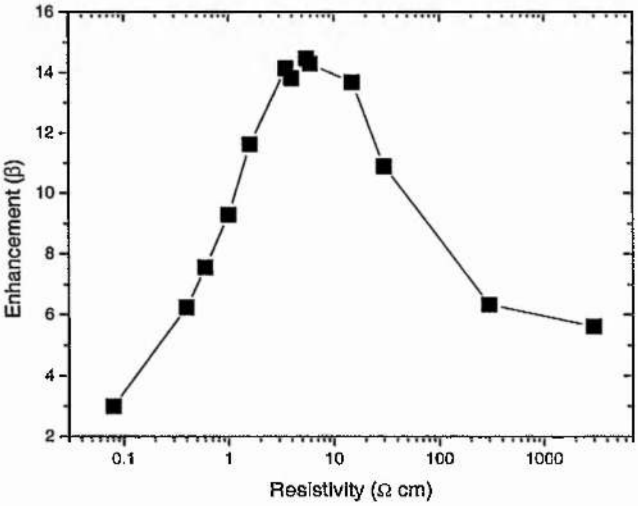

Figure 6-16: The variation of the enhancement factor as a function of the resistivity. The simulation of R_l=30nm, R_2 = 300nm and D_l= 5nm.

Using the information from the optimised resistivity (doping) that gives the highest enhancement, the separation is then varied. Figure 6-17 shows the variation of the enhancement with distance. Figure 6-18 shows the field contour distribution.

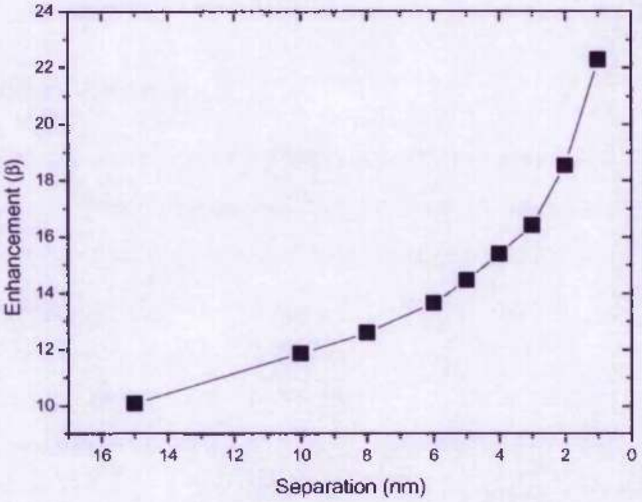

Figure 6-17: The variation of the distance, with the maximum (n-type) doping 7x10^{14}, the enhancement increase from 10 to 23, when the separation if reduced from 10 to 1nm.

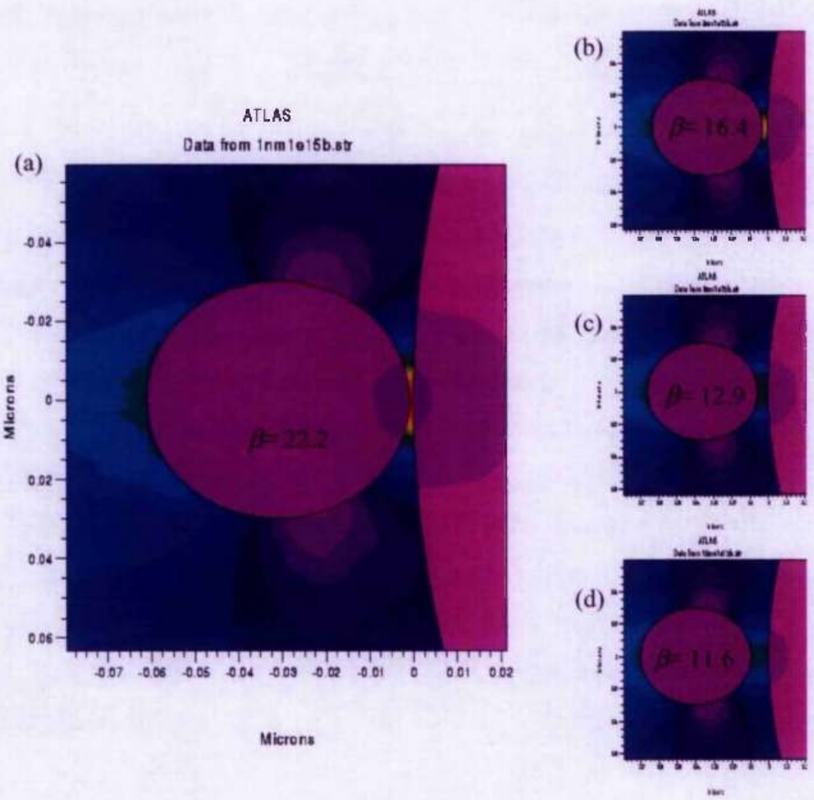

Figure 6-18: The field contour variations with distance. From (a) 1nm, (b) 3nm, (c) 6nm and (d) 10nm. The enhancement factor falls from 22.2, 16.4, 12.9 and 11.6 respectively.

6.8 Discussion

6.8.1 Structural properties

The schematic representation of the GAC films is shown in Figure 6-19. In Figure 6-19 (b), a highly stressed and dense film is shown with locally dense sp^2 clusters, probably cross-linked by a small fraction of sp^3 sites. Figure 6-19 (a) shows the possible arrangement when the a-C film has low sp^2 sites and low stress.

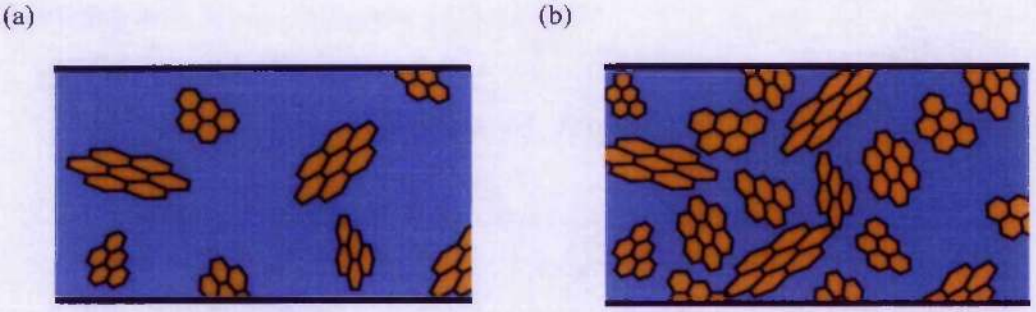

Figure 6-19: Illustration of (a) film with low sp^2 sites and stress, and (b) film with a high number of sp^2 sites and high stress.

The sizes of the clusters seems to be a very important parameter. The results from Raman and EELS, have shown that these films compose of high π bonding. It is difficult to estimate the average cluster size based on the data so far; electron paramagnetic resonance (EPR) measurements observed a spin density of $<10^{16}$ cm^{-3} for the films and together with the band gap of 0-0.5 eV this indicates that the films are composed of truly larger clusters than those observed in TAC. Therefore, the estimation of cluster size from Raman using I(D)/I(G) (~2) would have underestimated the actual cluster size. Using the model proposed by Ferrari and Robertson [72], the cluster size for a-C films with a Raman I(D)/I(G) of ~2 will be about 2 nm. Interestingly, the STM and TEM measurements give the real insight to the sp^2 clusters size, which is nearly ten times in these nanostructured carbons. Analysing the result for the 400 eV Ar assisting film, the STM shows that the conductive nano-clusters are on average 60 nm forming large islands close to 1.5 μm.

6.8.2 Effect of stress within the films

In order to understand the effects of intrinsic stress on the nano-structured carbon thin films, it is useful to compare the effects of high pressure on the lattice parameters of polycrystalline graphite. In the work by Lynch and Drickamer [88], hydrostatic pressure was applied on powdered graphite in order to study the changes in the inter-plane lattice spacing. A significant decrease of inter-plane of the c-axis was observed with an increase of pressure from 0 to 14 GPa. To compare these results, the relative plasmon energy was plotted as a function of the intrinsic stress. The intrinsic stress found in these films is about the same order of magnitude to those of the hydrostatic experiment.

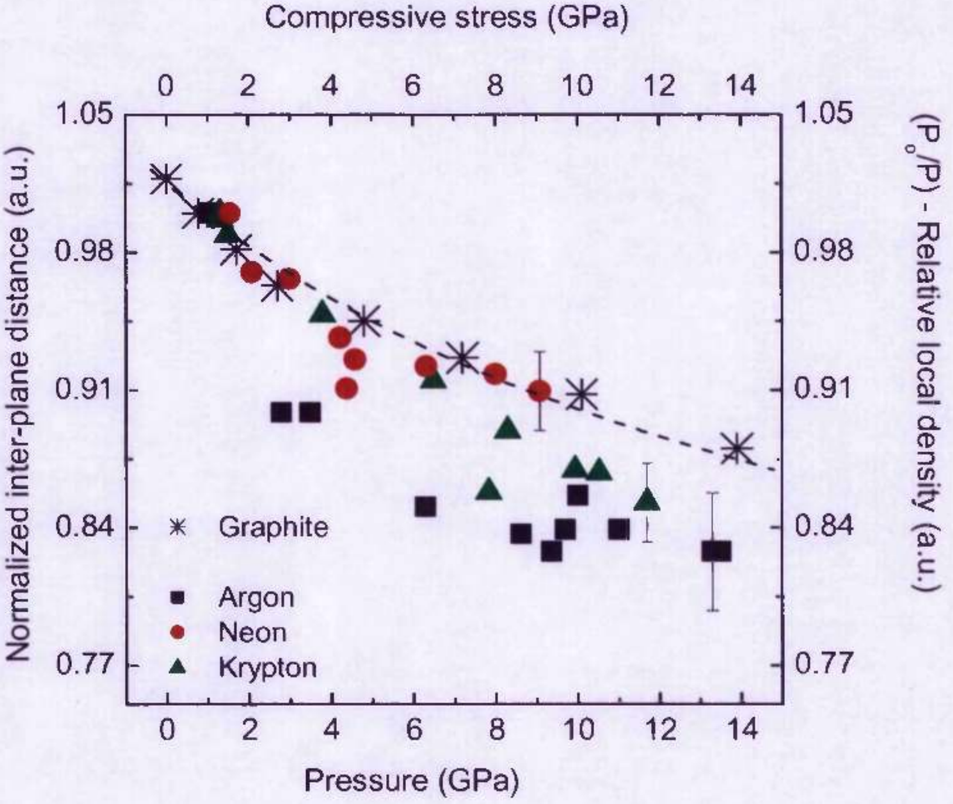

Figure 6-20: Comparison of the normalized inter-plane distance and local density to the variation of pressure and compressive stress.

In Figure 6-20, the relative local density (plasmon density) shows very similar trends to those of the changes in the inter-plane distance. Therefore, it is possible that under similar stress values within the thin films, the nano-domain could experience a similar effect where the inter-plane distance can be varied. The suggested reduction of the inter-plane distance can also be thought of as the effect of stress bringing the nano-domains closer together and hence resulting in an increase in the local density. This system of compressing the carbon nano-domains would therefore be crucial in determining the changes in the electronic properties.

Indeed the effect of stress has been a dominating force on the electronic property modifications. In Figure 6-21, the plasmon energy and sheet resistivity are plotted as a function of the intrinsic stress. Here, we observe the increase in the plasmon energy and decrease in the sheet resistivity as the intrinsic stress within the film increases. Therefore, intrinsic stress enhances the electronic properties by bringing the clusters closer together or by reducing the inter-plane distance within the nano-domains.

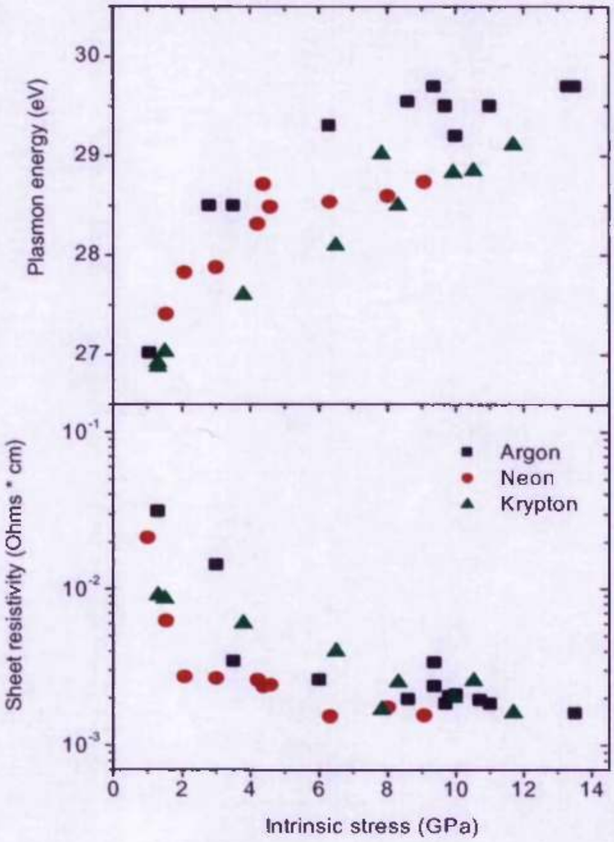

Figure 6-21: Plasmon energy and sheet resistivity as a function of the intrinsic stress of the films.

The effect of stress/pressure induced band structure modification has been observed in graphite. The work by Ahuja *et al.* [89] shows that the lattice constant c/a subject to 10 GPa hydrostatic pressure results in the reduction in the c/a ratio from 2.72 to 2.42. To have an idea of how significant is the reduction between the distances of the graphite planes on the electronic properties, we applied a simple two-band model [90] for the electrical conductivity in the basal plane of graphite. In this model, the concentration of electrons is $n_e = \frac{8\pi m_e^* kT}{\hbar^2 c}\ln\left[1+\exp{\eta}/_{kT}\right]$ where c is the interplanar distance and η is the chemical potential. Assuming band overlap and m^*_e is the effective mass of an electron, this two-band model indicates that the decrease of c can lead to the increase of the electron concentration an/or increase in η. This can benefit the electron emission process by providing a larger pool of electrons or lower barrier for emission. According to the hydrostatic experiment by Lynch et al. on graphite, [88] by applying a pressure of 12 GPa on a microcrystalline graphite sample, there is a 15% decrease in the distance between the planes.

6.8.3 The field emission model

The problem for any model that describes field emission from carbon thin films such as the F-N model is that the estimated effective barrier height is very small, 0.01-0.05 eV. It was found from the electron energy distribution of emitted electrons that the electrons were not originating from the conduction band region. In fact different researchers [91,92] have found that the emitted electrons originate from the valence band. Interestingly, the width of the energy distribution was deconvoluted to give a local field of 6500 V/μm with a barrier height of 4.9 eV.[92] It was suggested that the emission perhaps originated from either the valence band with the Fermi level position at the top of the valence band or metallic like predominantly sp^2 bonded carbon. This is consistent and in agreement with an emission mechanism that has a large work function of 4.9 eV and would require a large field enhancement factor of 200 to 400. Possible band structure is illustrated in Figure 6-22 where the electrons are emitted from the Fermi level. However, the reasons for the high enhancement factors are still unknown.

Indeed, the most significant difference in graphitic a-C from PAC films is the inhomogenity on the surface and the bulk due to the graphite-like sp^2 clusters. Figure 6-23 shows the possible band diagram along the surface, assuming a sp^2 cluster that is about 10nm, surrounded by a more insulating diamond-like sp^3 matrix. The band diagram would have a large variation in potential between the nano-cluster and surroundings. This effect causes significant change when an electric field is applied on the film surface. This inhomogeneity mechanism is comparable to the antenna effect proposed by Latham. [93] He proposed conducting filaments through the film cause field enhancement due to the external field lines focusing on charges trapped in the filaments. However, in this proposed model, the field enhancement does not require a filament through the film since the electric field does not penetrate through the films. Instead, the conductive clusters near the film surface could allow the field emission at low applied field.

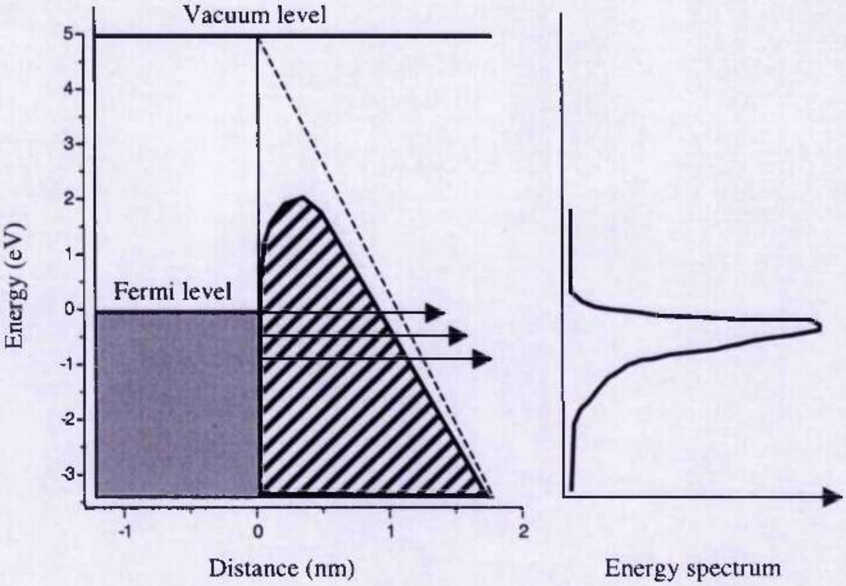

Figure 6-22: Schematic representation of the potential barrier, emission from the Fermi level results in the energy spectrum around the lower energy region.

It is interesting that the effect of the intrinsic stress plays a very important role in this model. Figure 6-24 shows the possible band model which is affected by stress/pressure. Indeed, stress promotes field enhancement by bringing the conductive clusters closer together. Also, stress could induce a band-overlapping effect which increases the electron density by moving the valance band above the Fermi level. This effect is similar to lowering the emission barrier height, therefore easing the emission process.

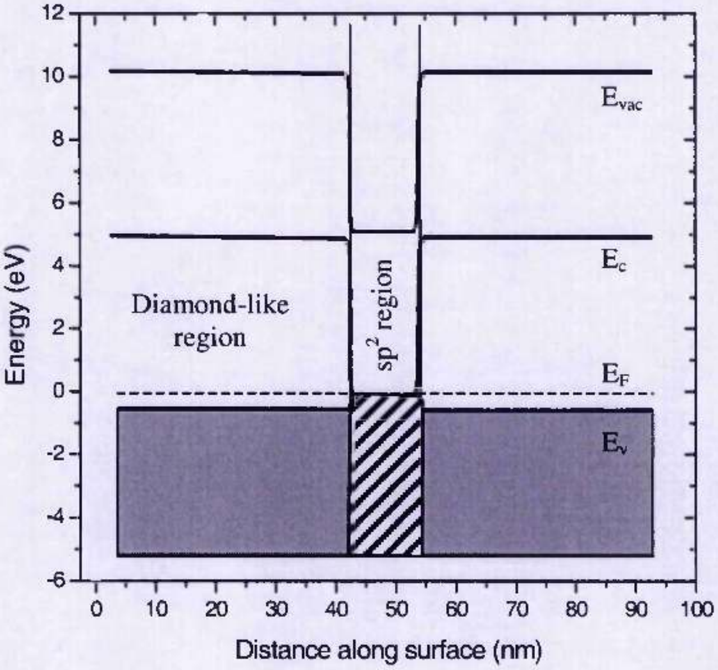

Figure 6-23: Schematic representation of the band diagram across an inhomogeneous surface.

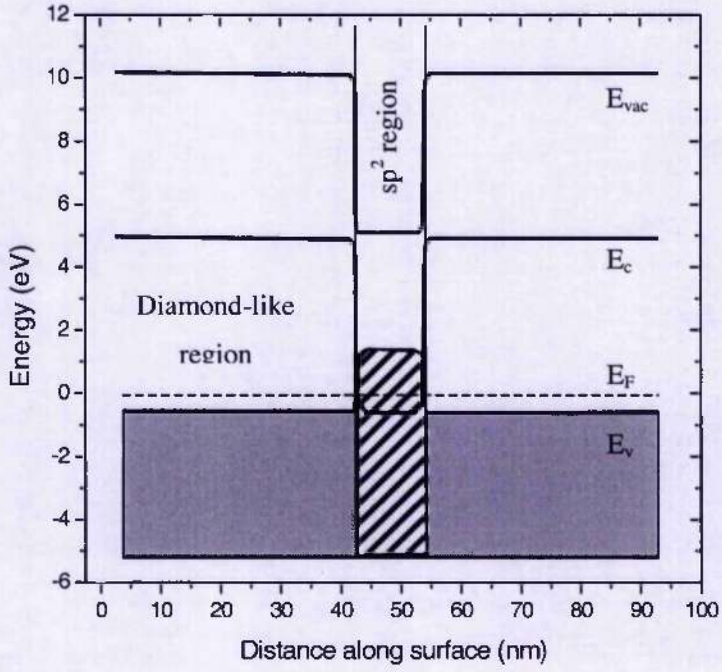

Figure 6-24: Schematic representation of the band diagram across an inhomogenous surface with the stress induced effect on the band overlapping.

6.9 Summary

In this chapter, we have discussed the field emission properties of nano-structured amorphous carbon. It has been shown that by changing the deposition conditions, the electronic and structural properties are altered. It is also possible to obtain high stress and high local density carbon films that are graphitic. Intrinsic stress and plasmon energy of up to ~12 GPa and ~29.5 eV respectively have been observed. These values in the past were only observed in the highly tetrahedral amorphous carbon films and were thought to originate from the sp^3 bonding.

The observed field emission threshold fields are consistent with the variation of intrinsic stress and plasmon energy. These suggest that low threshold fields can be obtained from the effects of having the carbon clusters close together. In fact, threshold fields as low as 7 V/μm have been obtained from these films. This value is lower than those reported from PAC and DAC films.

The simulations based on two conductive spheres have indicated that it is possible to obtain electric field enhancement by changing the separation distance. Field enhancement was increased from a factor of 10 to 23 when the separation distance is reduced from 15 to 1 nm.

Finally, the emission model from these GAC films is proposed. The modification of this emission model is based on the inhomogenity of the amorphous films. The dielectric mismatch and the effect of stress were explained.

Chapter 7

7 Field emission properties of carbon nanotubes

7.1 Introduction

Due to the special geometrical structure of a carbon nanotube (CNT), high aspect ratios of up to 1000 can be obtained. This would generate an enormous amount of electric field enhancement to allow electron emission at low macroscopic field. Furthermore, large current densities of the order of 4A/cm^2 have been reported. [94] To fully utilise carbon nanotubes as a cold cathode for displays, some important aspects need to be examined. Firstly, the demand on the applied electric fields needs to be low, typically much lower than 20 V/μm. This would allow for long life times, stability and prevent burnout. Secondly, the emission current density needs to be sufficiently high at such a low electric field. For a field emission flat panel display, current densities up to 10 mA/cm^2 are required. Indeed, many authors have obtained low threshold fields or high current densities from CNT emitters. In this chapter, we have conducted a systematic study based on the field emission properties of CNTs containing polystyrene (PS). The concentration of the CNTs was varied to control the field emission and electrical properties. We concentrated on the comparisons between the field emission thresholds, current densities and emission site densities. Results indicate that the field emission properties of randomly oriented CNTs are comparable to those of aligned as well as e-beam defined arrays of CNTs/carbon fibers.

7.2 Characteristics of the CNT-PS films

The MWNTs and Boron-doped MWNTs (BMWNT) were synthesised using a plasma arc-discharge between two graphite electrodes while BMWNTs were produced from Boron containing electrodes. [95] The boron concentration in the BMWNT is not precisely known, however, and electron energy loss spectroscopy indicates about 1 % of boron content within these tubes based on the K-edge spectra. The presence of boron does not change the crystal lattice significantly, so that the electron band structure remains essentially unaltered. However, there is an apparent depression of the Fermi level by *ca.* 0.1 eV. The TEM investigation of the as-grown nanotubes are shown in Figure 7-1 (a) and (b) for MWNT and BMWNT respectively. It can be observed that the as-grown carbon composite from the arc-discharged system contain MWNT, carbon particles and amorphous carbon layers. To improve the purity of the as-grown CNT a series of purification steps by micro-filtering and oxidation (500-600 °C for 40-50 min) were conducted to remove the amorphous carbon and carbon particles. The purified CNTs are shown in Figure 7-2. The TEM micrograph shows that the purification process removed the carbon particles and they are now composed of at least 90% of MWNT with diameters of about 10-50 nm.

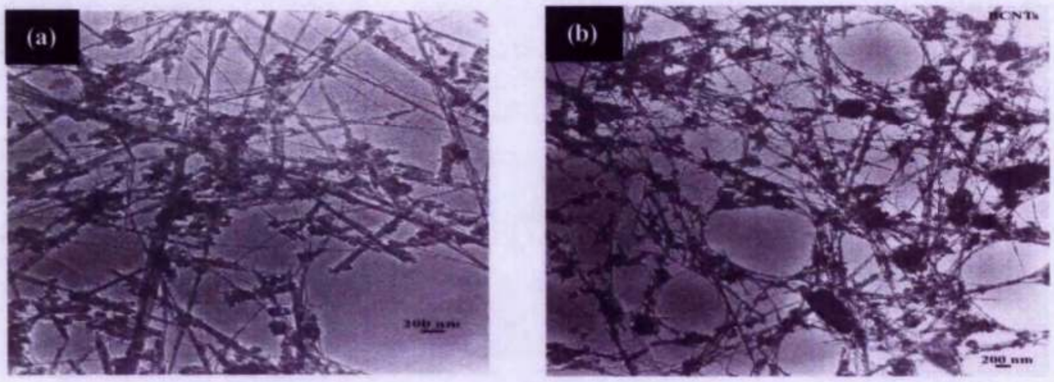

Figure 7-1: TEM images of the carbon nanotubes before (a) and after (b) purification.

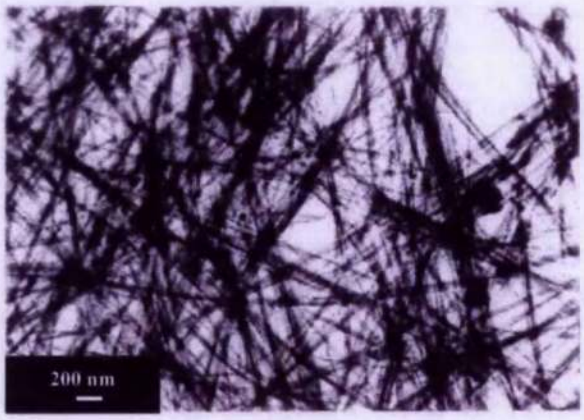

Figure 7-2: TEM micrograph of purified MWNT. Oxidation and micro-filtering removes the carbon particles and amorphous carbon.

Using HRTEM, the quality of the MWNTs before and after purification is studied. In Figure 7-3 (a), the MWNT is found to have about 30 walls and before purification, a layer of amorphous carbon is found on the surface of the MWNT. Figure 7-3 (b) shows two overlapping MWNTs pointed by the Arrows 1 and 2. After oxidation, the tube surface is seen to be clean without the amorphous carbon coating.

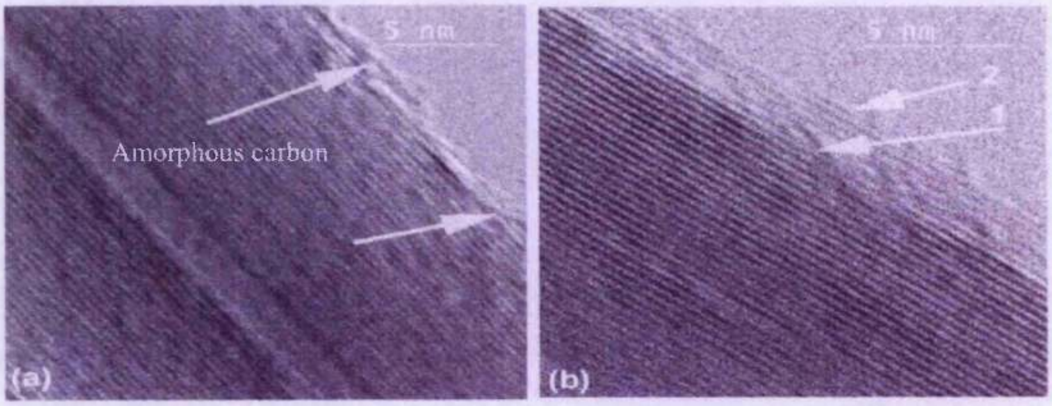

Figure 7-3: Amorphous carbon disappeared after the oxidation and tube surfaces are clean (b, two tubes overlapped arrows 1 and 2).

To use the CNT as an electron field emitter, the MWNT rich powder is mixed in PS with toluene into ratio by weight as $\left[\frac{MWNT}{(MWNT+PS)}\right]$ with in this work, ratios of 11.1%, 14.3%, 20%, 25% and 33% of films being produced. The mechanical and electrical properties of the composite film depend strongly on the ability to disperse the CNTs homogeneously throughout the polymer matrix without destroying the integrity of the CNTs. The MWNT was dispersed in the PS with toluene solution by sonification for 30 mins. The mixture was then cast into a Petri dish and the toluene was allowed to evaporate in vacuum to form a film of 0.2 mm thickness. All as-cast films were hot-pressed between 2 glass slides and heated to about 100 °C. Hot-pressing helps to remove residual solvent and prevent voids in the films. [96] Figure 7-4 compared the cross-section of the CNT-PS film before and after hot-pressing. It can be seen that the film after hot-pressing (Figure 7-4 (a)) is solid and does not have any visible voids. However, Figure 7-4 (b) shows that the as-cast film before hot-pressing is very porous.

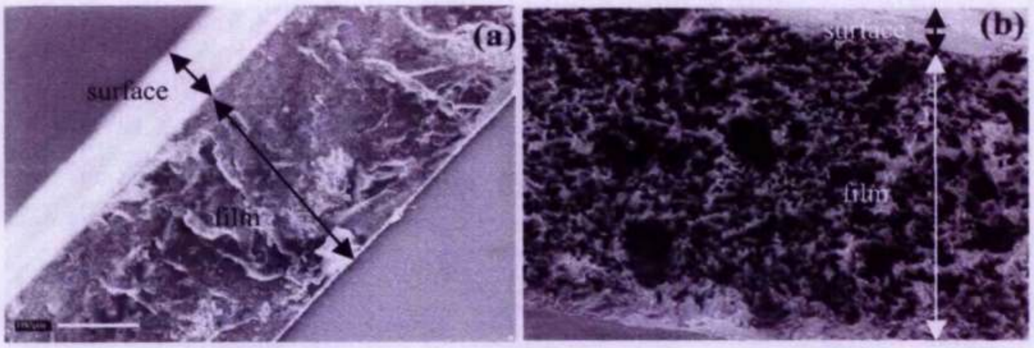

Figure 7-4: Film after hot pressing (a) and as cast film before hot pressing (b). Hot-pressed films are very uniform and solid (a). The as-cast films are very porous (b).

SEM observation on the high MWNT concentration sample (20% wt.) reveals that the surface composes of randomly networked CNTs on the film. In Figure 7-5, CNTs can be seen to form tracks across the surface, these CNTs are found to be cross-linked together in some regions. However, over the large scale, the distribution of these CNTs is found to be uniformly dispersed.

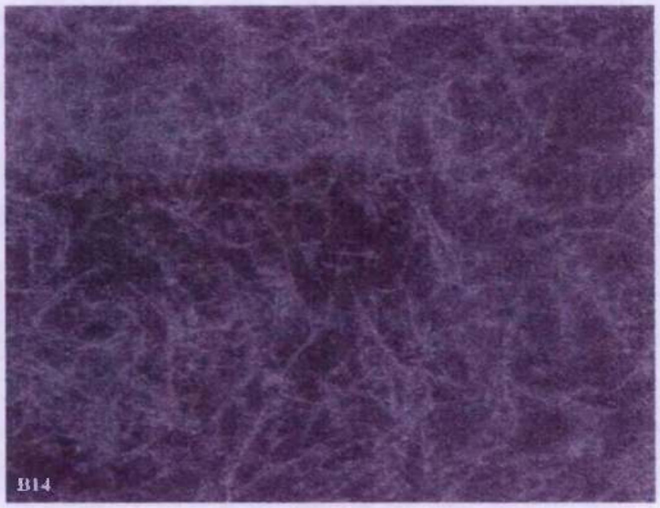

Figure 7-5: SEM observation of the film surface of a 20% wt. BMWNT-PS sample.

To investigate those CNTs that are embedded within the PS, the film was mechanically bent to create a 4 μm gap that exposed the embedded CNTs (Figure 7-6). Due to the mechanical bending, the CNTs are found to be aligned due to local stretching. At CNT concentrations below 14.3%, SEM revealed that the CNT concentration is reduced at the surface and in some cases can no longer be observed. However, some small tube sections can still be exposed to the surface.

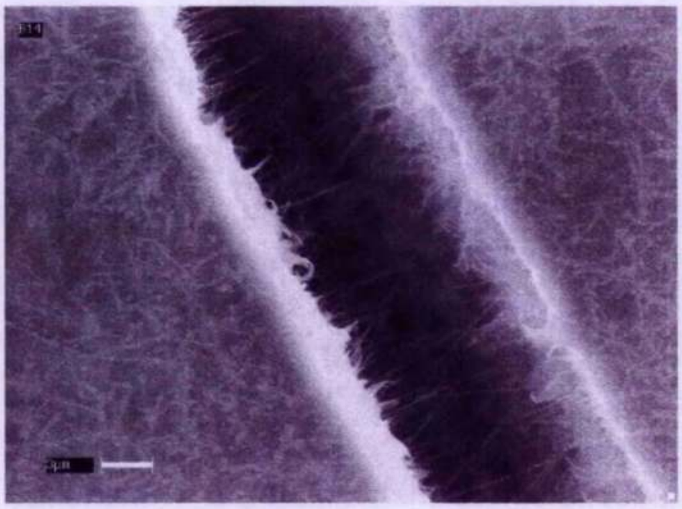

Figure 7-6: Mechanically bent film surface. CNTs are found to be embedded in the PS matrix.

All films were then cut into 1 cm^2 area and the composite CNT-PS film thickness was about 200 μm. The film was connected to a SEM pad using silver paint. Figure 7-7 shows the MWNT-PS emitter. The sample was left to dry out before any measurements were taken.

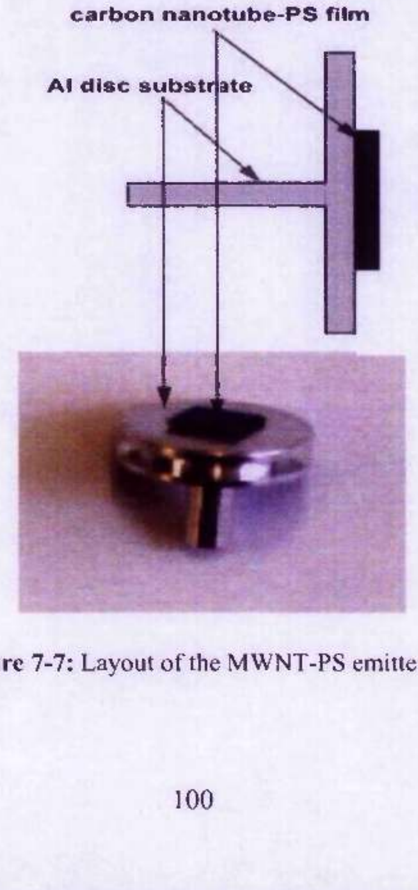

Figure 7-7: Layout of the MWNT-PS emitter.

To investigate the electrical properties, the sheet resistivities of these films were measured using a 4-point probe. This also gives an indication on the uniformity of these films. In Figure 7-8, the sheet resistivities of MWNT-PS and BMWNT-PS films were examined. The film resistivity decreases at the CNT concentration increases. For MWNT-PS films, the resistivities fell from 15 to 0.1 Ωcm as the nanotube concentration increases from 11.1 to 33.3 %. The BMWNT show a more conductive nature due to the effect of boron doping in the CNT. The sheet resistivity decreases from 2.5 to 5×10^{-4} Ωcm, when the concentration increases from 11.1 to 33.3%. Interestingly, the sheet resistivities on both sides of the film are found to be within the same order of magnitude, which indicates that the uniformity of the distribution of CNT within the film is good and also well dispersed across the film. The film resistivity, in general, decreases as the CNT concentration increases, which indicates the electrical conduction across the film is mainly controlled by the CNT network and CNT percolation within the bulk structure as previous reported.[96] The low film resistivity observed in BMWNT-PS films are due to the lower intrinsic resistance of BMWNTs.[95]

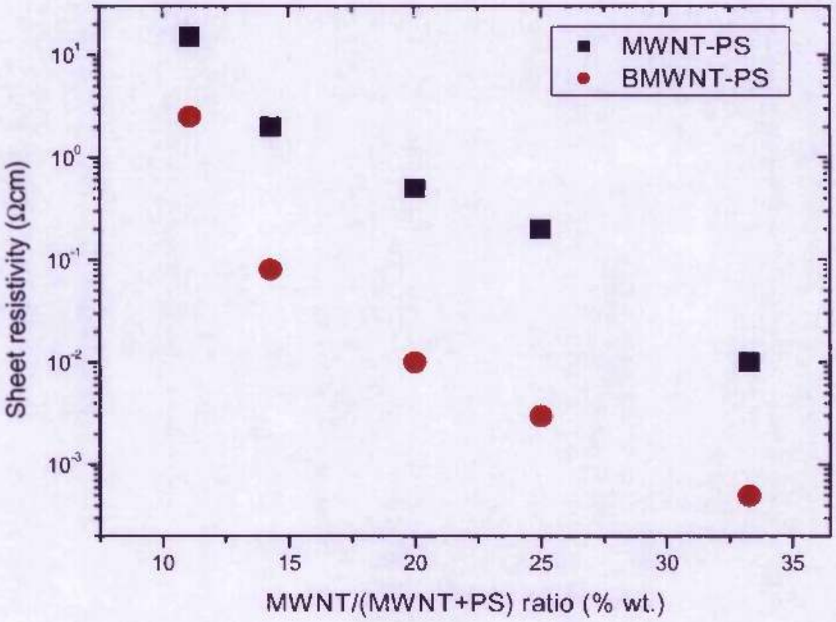

Figure 7-8: Sheet resistivity measured by a 4-point probe.

7.3 Field emission characteristics

In this section, the field emission characteristics are discussed in term of the threshold fields, current density and the emission site density. The electric field screening effects are found to dominate the emission threshold fields where in the sample with high CNT concentration, higher applied electric fields are required to emit electrons. The current density on the other hand is affected by the current saturation effects, however, current densities up to 10 mA/cm^2 can be obtained at low electric fields.

7.3.1 Probe technique

The field emission threshold field is determined by the probe measurement technique. For each sample, four different locations are tested. At each location, the voltage is ramped from 0 to 2200 V until the maximum current of 1 μA is reached before ramping down. To determine the threshold field, the I-V characteristics are recorded at 5 different separation distances.

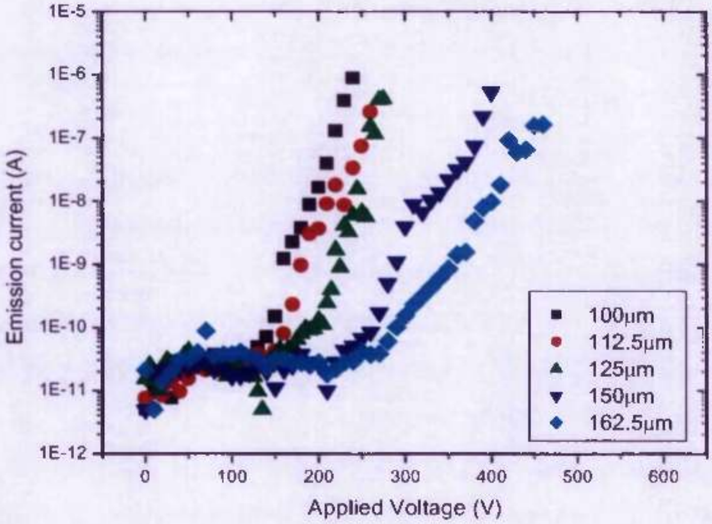

Figure 7-9: FE for sample with 11% wt. MWNT-PS concentration from 100-162.5 μm.

Figure 7-9 show the typical characteristic of sample with 11% wt. MWNT-PS concentration. By extracting the voltage to obtain an emission current of 1 nA, the threshold voltage was plotted as a function of the changes in separation distance shown in Figure 7-10. The slope obtained from the curve assuming a linear relation between the threshold voltage and variation in distance is the threshold field for that particular point in the sample.

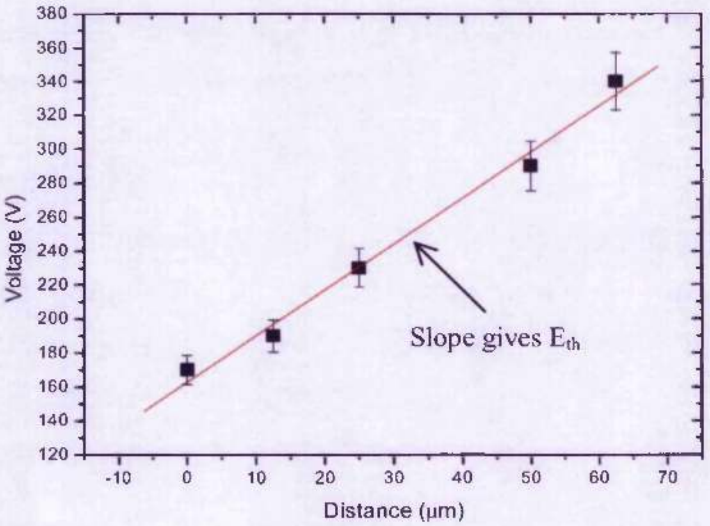

Figure 7-10: Variation of the threshold voltage as a function of the variation of the separation distance.

The threshold fields obtained out of the four different locations across the sample were averaged to give the threshold field of the sample. Figure 7-11 shows the variation of the threshold fields (E_{th}) as a function of CNT concentration. The threshold fields determined by the probe method shows that both MWNT-PS and BMWNT-PS films emit electrons at low electric fields between the ranges of 1.6 to 5.3 V/μm. The MWNT-PS films exhibit a E_{th} of 1.6 V/μm at 11.1% CNT concentration which increases to 5.3 V/μm at 33.3% CNT concentration. Similarly, for the BMWNT-PS film, E_{th} increases from 2.6 to 4.8 V/μm when the CNT concentration increases from 11.1 to 33.3 %. Despite the BMWNT being more conductive (as shown in Figure 7-8) there is no significant modification of E_{th} compared to the undoped MWNT. This indicates that the field emission mechanism is purely controlled by the geometric enhancement due to the high aspect ratio of the CNT and surface effects such as shielding. Interestingly, E_{th} for both types of film increases when the CNT concentration increases, which gives a strong indication of the effect of field shielding from adjacent CNTs.

This effect prevents the electric field to be uniformly/homogenously applied across the CNT surface and hence results in the reduction in field enhancement effect. However, there would be an optimal CNT concentration, as to the point when further reduction in the CNT concentration will not reduce E_{th}. In this work we are unable to determine lower CNT concentration samples, as when the CNT concentration is too low, dispersion of the CNT uniformly across the film is difficult. Despite the field emission threshold fields varying only slightly with the CNT concentration at low CNT %, it is worth noting that the observed threshold fields are very low when compared to metal-emitting surfaces [5] (> 100 V/μm) or diamond-like thin films [97] (10 – 30 V/μm).

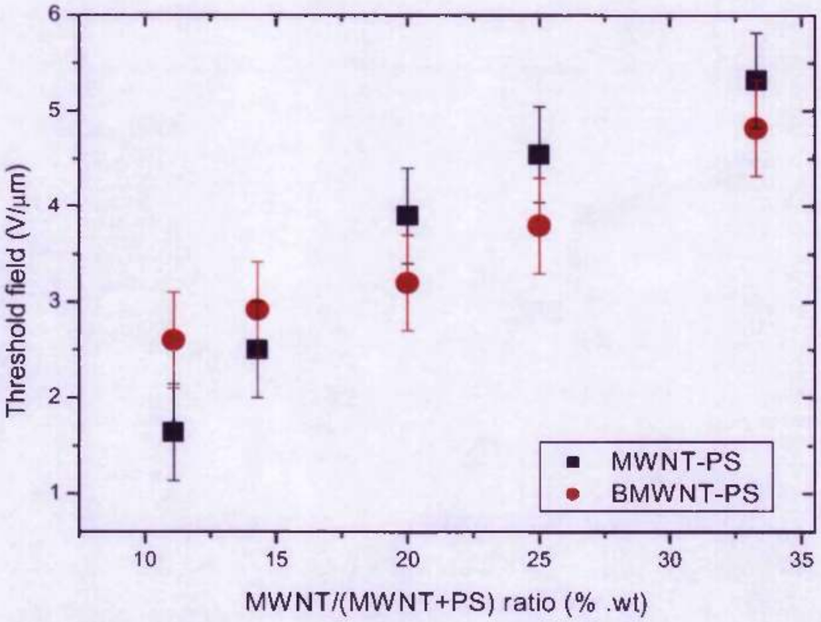

Figure 7-11: The variation of threshold field as a function of the CNT concentrations.

7.3.2 Planar technique

It is very difficult to determine the current density of the field emission characteristic using the probe technique. The emission area is believed to be less than 0.5 mm^2, and cannot be reliably determined. Therefore, the field emission characteristics were measured using the planar technique with a fixed test area. The field emission characteristics measured using the planar setup is shown in Figure 7-12 for MWNT-PS films and Figure 7-13 for the BMWNT-PS films. It can be observed that the emission threshold fields observed in both planar and probe set-ups are very similar and fall within the error bars. This is further evidence that the field emission measurements are self consistent in this work. Here, the current density is determined by the emission current over a fixed emission test area of 5 mm^2 and the emission area is controlled by the shape of the PTFE during the experiment. Interestingly, all films show current saturation effect at high current density of about 4 x 10^{-5} A/cm^2. There are a number of mechanisms that might lead to current saturation effects during field emission, among which are solid state transport in the cathodes, contact resistance, vacuum space charge effects and the effect of adsorbate states on the CNTs.[98,99,100]

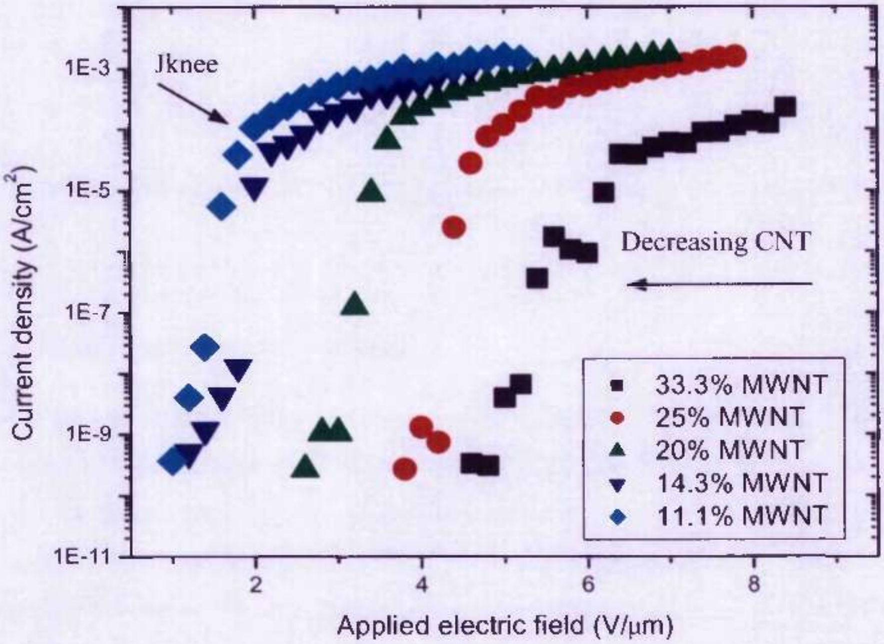

Figure 7-12: Emission characteristic of MWNT-PS films with different concentration.

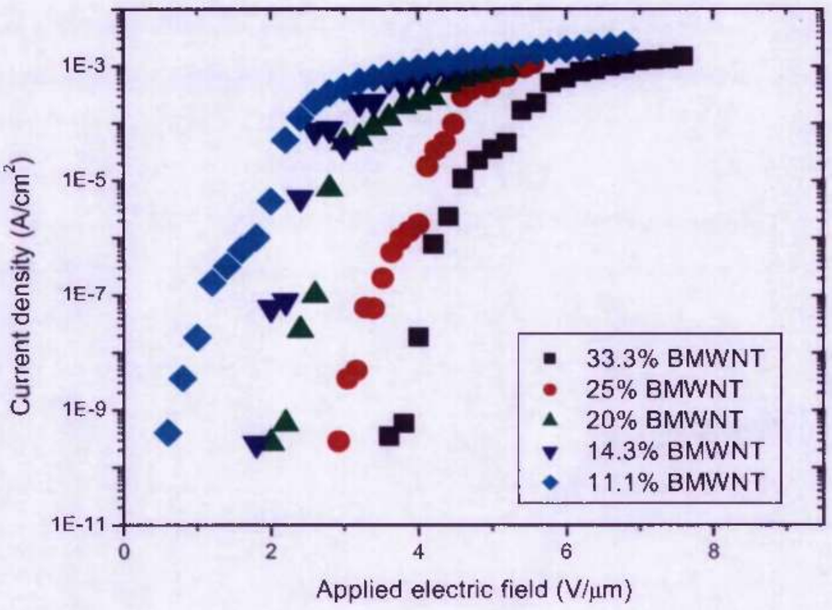

Figure 7-13: Emission characteristic of BMWNT-PS films with different concentration

7.3.3 Field emission site density

The setup for the field emission site density measurement is similar to the planar technique but a Charge Coupled Device (CCD) camera was installed to capture the emission image. The emission site density gives detailed information on where the electron emission originates on the sample. It is an important figure of merit that has been neglected by many workers who only characterise the emission properties based on threshold field and current density. There were two types of anode used in this experiment, low voltage and high phosphor/ITO glass.

The high voltage anode phosphor used was ZnS:Cu (green phosphor), with phosphor particle size of about 5 micron, thickness of the phosphor coating is about 20 micron, the working voltage is less than 1000V. The sheet resistance of the ITO is 100 ohm/cm^2. To fully understand the field emission properties of CNT-PS films, the current density, threshold field and emission site density must be characterised. In Figure 7-14, the current density was plotted as a function of electric field. The emission site density was recorded for different points indicated by the arrows.

The emission test area was 5 mm^2 to investigate the homogeneity of the emission pattern over a large area. It can be seen that for the sample with 11 % wt. BMWNT-PS a very spotty emission pattern resulted. This suggests that the electron emission is dominated by regions with higher field enhancement and these regions are randomly found across the film.

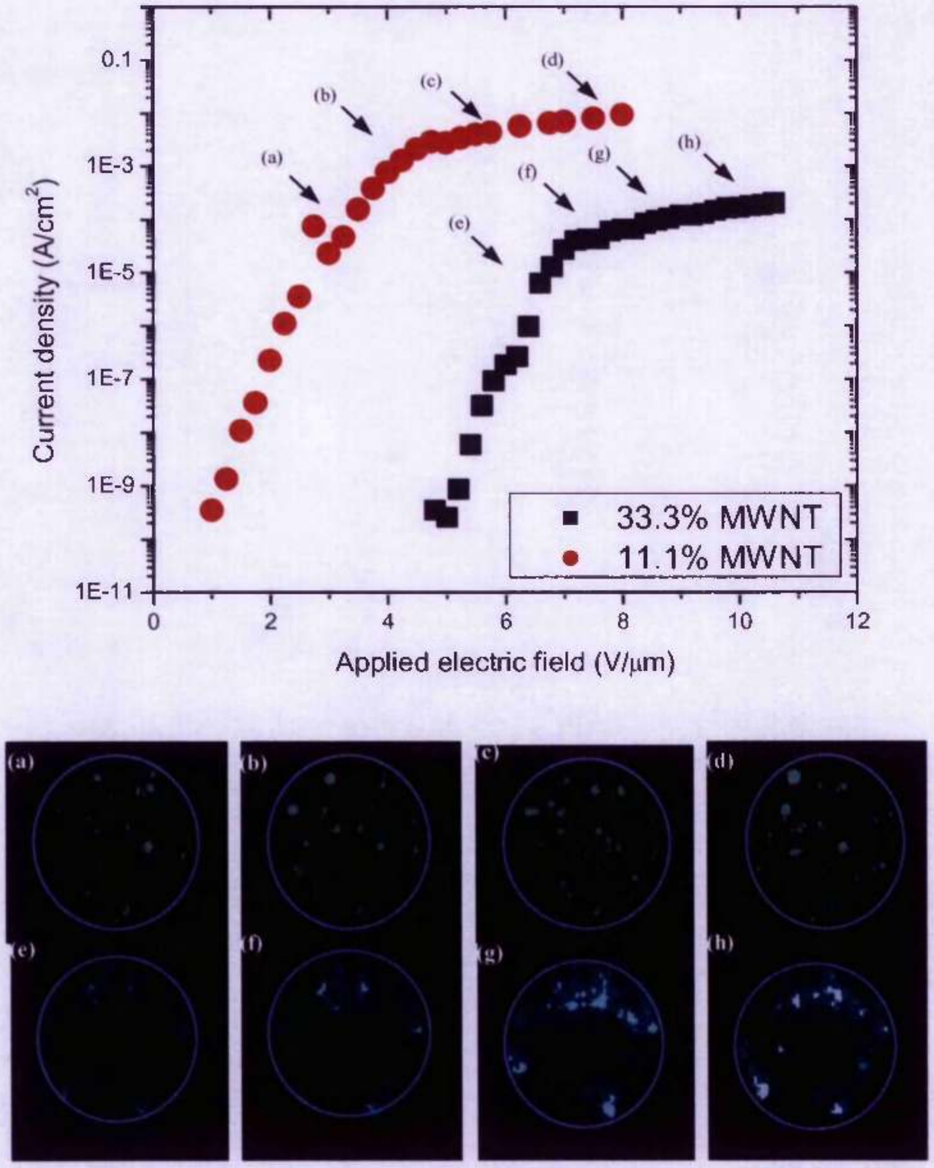

Figure 7-14: Emission current as a function of applied field of 33.3% wt. and 11.1% wt. BMWNT-PS sample. The images are captured at different applied fields.

For the sample with 33% wt. BMWNT-PS, the emission pattern is seen to be much higher where the emission regions are larger on average. However, preferential and "spotty" emission patterns were also observed. The effect of a using high voltage phosphor results in a dimmer image where the phosphor is less sensitive.

The emission site density can be estimated by counting the number of emission spots across the film. Assuming each spot size is about 5 μm which is the particle size of each phosphor, the emission site density for the 11% and 33% BMWNT-PS film is shown in Figure 7-15 and 7-16 respectively.

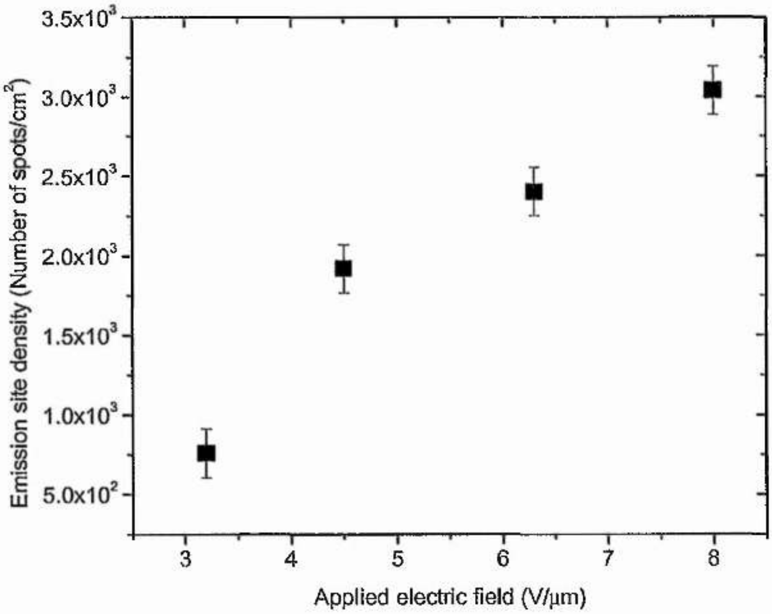

Figure 7-15: Site density of 11% BMWNT-PS film.

It can be observed that the site densities of both films are lower than 1 x 10^5 which is below the requirement for display applications. However, the poor site density may be explained by the sensitivity of the phosphor as well as the fact that no ballast resistor was used. A ballast resistor would cut off high emission sites and flatten out the uniformity of the remaining emitters. Therefore, a low voltage phosphor was used for the emission site density test.

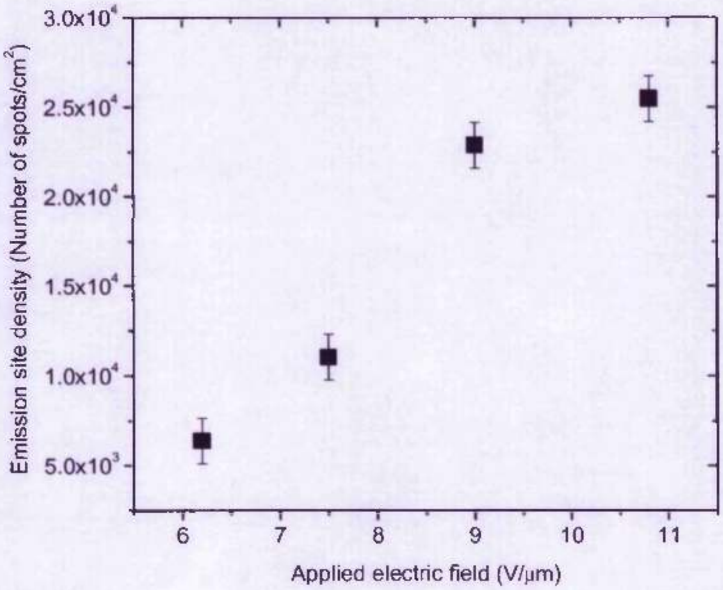

Figure 7-16: Site density of 33% BMWNT-PS film.

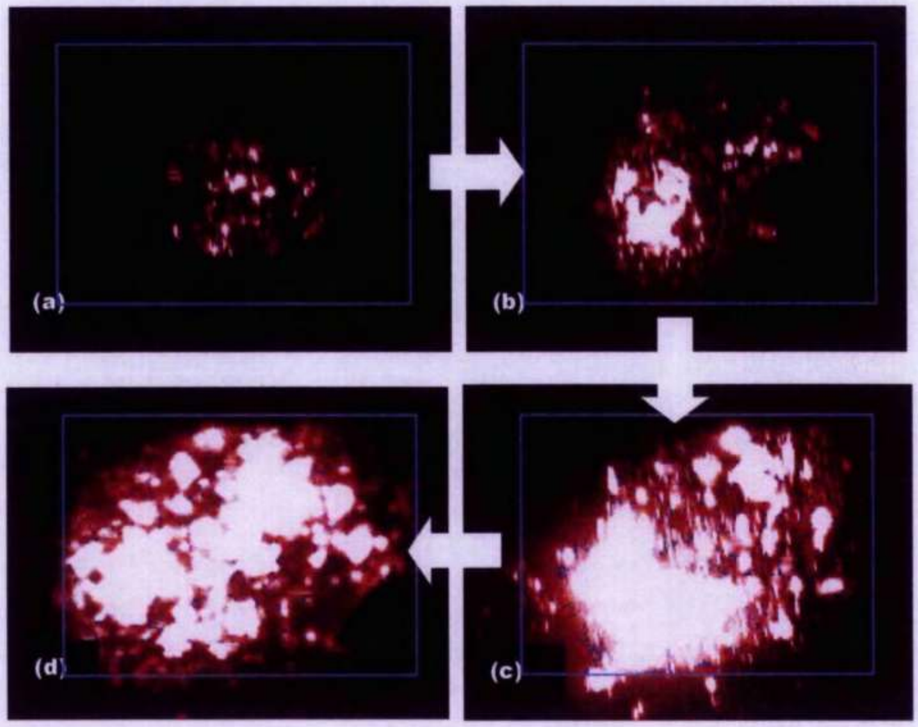

Figure 7-17: Emission site density of 11% wt. BMWNT-PS biased at (a) 1.3 V/μm, (b) 1.7 V/μm, (c) 2.0 V/μm and (d) 2.5 V/μm.

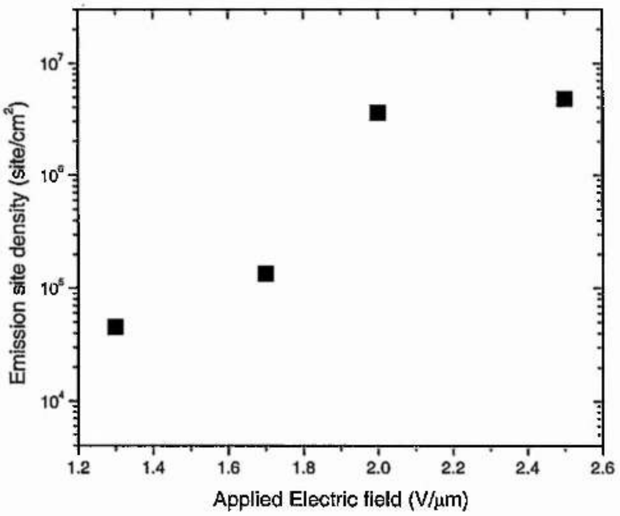

Figure 7-18: Emission site density based on low voltage phosphors as a function of applied field for a sample with 11% BMWNT-PS concentrations.

The low voltage phosphor operates at a lower voltage of 500 V, however, the particle size is much bigger than the high voltage anode at about 8 μm. Figure 7-17 shows the emission pattern of the sample with 11% wt. BMWNT-PS film with different applied fields. It can be observed that only a very low applied field of 2.5 V/μm is required to obtain an emission area of 70% over the 3 mm^2 area. This corresponds to an emission site density of about 4.8 x 10^6 (shown in Figure 7-18). For the sample with 33% wt. BMWNT-PS concentration, the emission pattern is shown in Figure 7-19. Higher applied fields were required to obtain good coverage for the emission pattern. However, it can be seen that it covers a larger area (~90%) over the 3 mm^2 region which corresponds to 1.3 x 10^7 sites/cm^2 (shown in Figure 7-20).

The difference in emission site density is due to the larger number of CNT on the film surface when compared to a low CNT density sample. However, due to the electric field screening effects, a large applied field is required to obtain a sufficient current to light up the phosphors. The low voltage phosphor is more sensitive to the emission and therefore very useful to obtain bright light emission to obtain the emission site density. In the case of using a high voltage phosphor, it can be observed that the field emission region is dominated by the CNT with lower field screening at the expense of sensitivity.

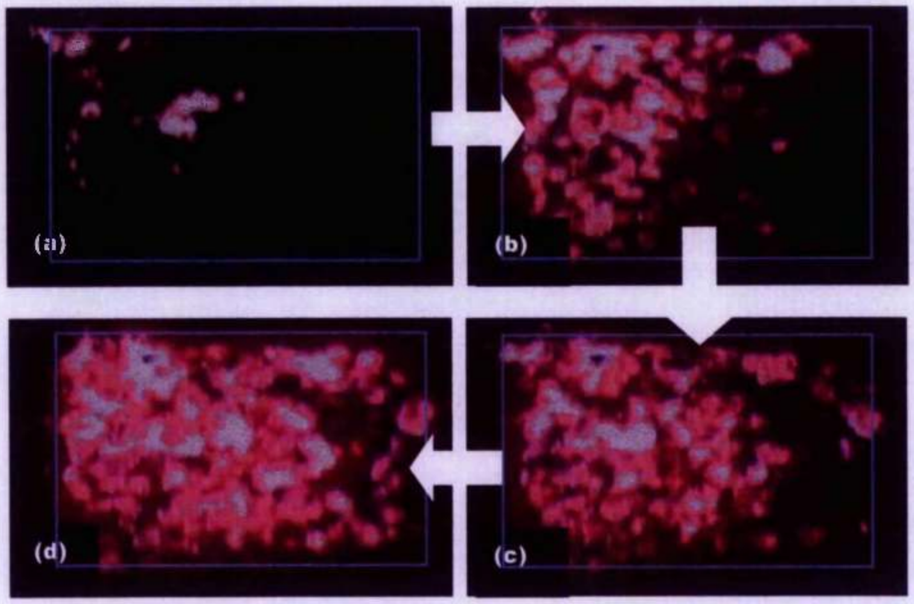

Figure 7-19: Emission site density of 20% BMWNT biased at (a) 5 V/µm, (b) 6 V/µm, (c) 7 V/µm and (d) 8.3 V/µm imaged on a low voltage phosphor.

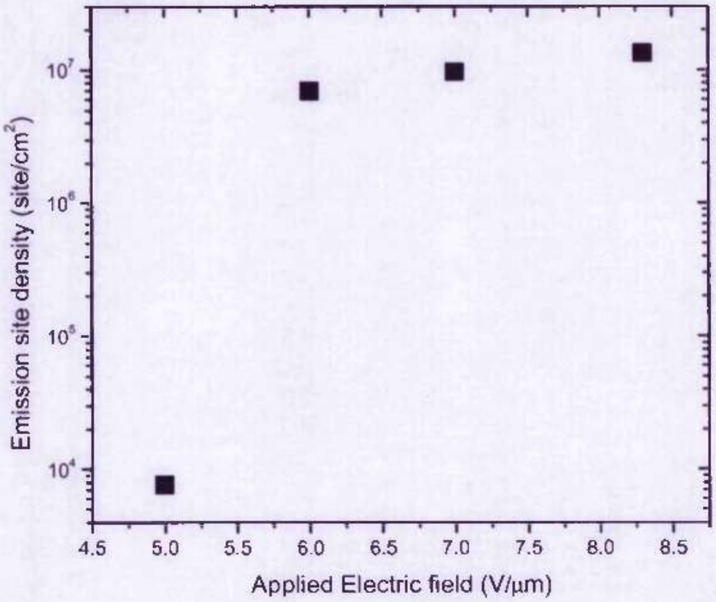

Figure 7-20: Emission site density on a low voltage phosphor as a function of applied field for a sample with 11% BMWNT-PS concentrations.

It is important to note that the results show that the CNT concentration or distance between the individual nanotubes is very important. Having high CNT concentration may have a higher emission site density, however, the required electric field is much higher. In the case of low CNT concentrations where the CNTs are further apart, the effect of field screening is lower or minimum, but this is at the expense of a lower site density.

7.4 Discussion

The field emission properties of the CNT-PS films will be discussed using the F-N analysis. The determination of the field enhancement factor and effective emission area will also be discussed. The emission current density of these films will be compared with CNT films that are aligned and emitters formed in arrays.

7.4.1 Fowler-Nordheim analysis

The field emission characteristics of these samples can be modelled by fitting the curves into the Fowler-Nordheim (FN) equation, $\frac{I}{\alpha}=\frac{A(\beta E)^2}{\phi}\exp\left(-\frac{B\phi^{3/2}}{\beta E}\right)$. Here, I is the emission current (A) and α is the effective emission area (cm^2), A and B are constants, and E is the macroscopic field (V/μm). β is the enhancement factor or amplification factor of the macroscopic field. β is often determined by the geometric shape of the emitter and can be approximately estimated to be $\frac{h}{r}$ where h is the height and r is the radius of the emitter. ϕ is the effective barrier height or in metal emitters it is the work function. Using the FN equation, one can estimate ϕ and β by plotting the FN plot where the slope is proportional to $\left(\frac{-B\phi^{3/2}}{\beta}\right)$ and the y-intercept is proportional to $\ln\left[\frac{A\alpha\beta^2}{\phi}\right]$. Using this, the slopes and y-intercepts of these films gives the FN SK diagram. [8] Figure 7-21 shows the variation of the FN slope and FN y-intercept for both MWNT-PS and BMWNT-PS films with different concentrations. It can be seen that as the concentration of the CNT decreases, the FN slope increases (less negative) and the FN Y-intercept decreases (more negative). The change in slope corresponds to an increase in β assuming the work function, ϕ, remains constant. The concomitant decrease in α with intercept, assuming the work function remains constant is in agreement with the reduction in CNT concentration which reduces the electric field screening at the surface. This in turn improves the field amplification effect and as less CNTs are present on the film surface, the effective emission area decreases. If we consider the emission area to vary linearly with the CNT concentration, the slight bowing upwards of the data set reflect the $(\beta)^2$ dependence of the curve as designed by the inventors of the S-K diagram. [8] Conversely, when the CNT concentration increases, the opposite effect happens where β decreases and α increases. This is observed in both types of films.

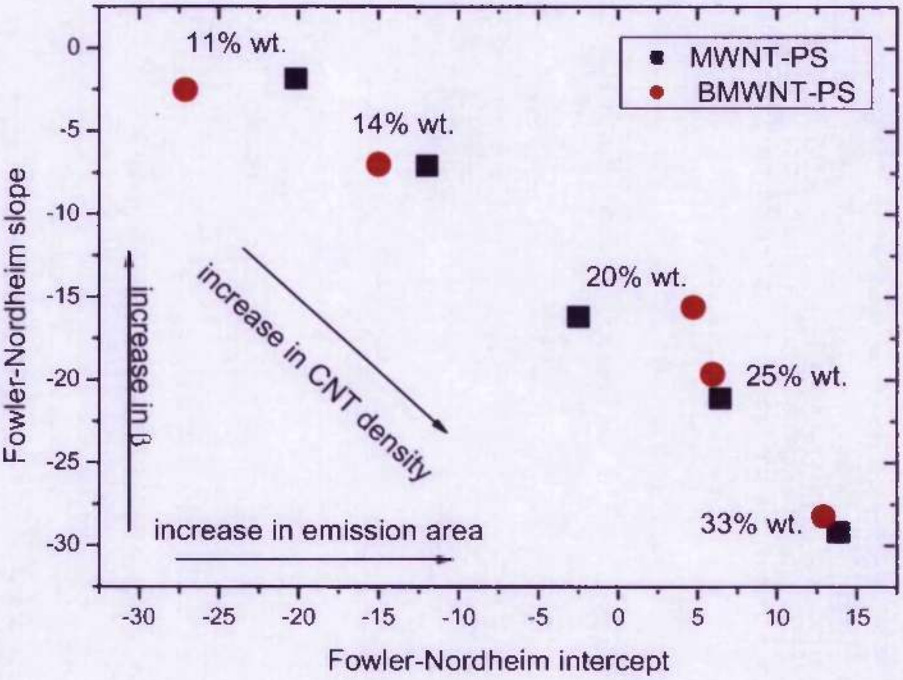

Figure 7-21: FN SK plot for both MWNT and BMWNT samples with different CNT concentrations.

7.4.2 Emission current density

In Figure 7-12 and 7-13, we define the onset point for current saturation effects as J_{knee}, which is the point where the field emission characteristics deviate from the tradition FN characteristics. The variation of J_{knee} as a function of CNT concentration is shown in Figure 7-

22. Interestingly, for the MWNT-PS films, J_{knee} is of the same order for both 11.1% and 33.3% films at 3 x 10^{-5} A/cm^2. The maximum value of J_{knee} was observed at a MWNT concentration of 20 %. This variation can be explained due to the fixed emission test area of 5 mm^2. Indeed, from the FN SK diagram (Figure 7-21), the effective emission area of MWNT-PS film with 11.1% was shown to be smaller than MWNT-PS film with 33.3%. Therefore, one would expect the current density or J_{knee} to be higher for the MWNT-PS film with 11.1%. However, if the emission test area is much higher than the effective emission area, the distribution of the emission current over 5 mm^2 would result in a fall in the current density or J_{knee}. To date, reports of large current density from CNT emitters are all based on small emission test areas, smaller than 0.5 mm^2 and we show that our simple to produce non-aligned films can compete with the best designed arrays fabricated using e-beam techniques.[33,101] The effect of boron doping of the MWNT has so far not shown any significant difference in terms of the emission threshold field. Investigations on J_{knee} do however throw up some notable results. At low BMWNT concentration, 11.1% and 16.7 %, there is no significant variation to that compared to the MWNT-PS films. When the BMWNT concentration was increased from 20 to 33.3 %, there is a significant drop in J_{knee} as compared to MWNT-PS films at the same concentration. It is noted from film resistivity measurements that the BMWNT-PS films are much more conductive due to the intrinsic electronic properties of the CNTs. This could be due to field screening effects, given that electric field line termination on conductive materials is much stronger.

Many other authors have observed current saturation effects. Here we fit the results from Collins *et al.*[37] which has 50 % wt. MWNT and Alexandrou *et al.*[102] which has 33.3% SWNT. Plotting the J_{knee} extracted from the two authors,[103] a curve was fitted together with the J_{knee} from MWNT-PS samples only. The curve indicates that J_{knee} is controlled by the CNT concentration within the polymer matrix and regardless of preparation technique or the type of CNT used. This significantly suggests that the current saturation mechanism in CNT-polymer matrix is largely controlled by the density of CNT present. This is also in agreement to the vacuum space charge effect where the position of the emitters contributes to the current saturation effects at high current density. It is also interesting to note that despite the same CNT to polymer concentration being used, a lower threshold field of 1.4 V/μm was observed from the SWNT sample (in ref. 106) as compared to 5.3 V/μm in this work. The current saturation effect occurs at about the same order of magnitude for both samples, further strengthing the case for the saturation to be associated with surface effects based on space charge rather than the physical properties of the films (MWNT vs. SWNT).

In order to compare the field emission characteristics of CNT in randomly networked polymers to the vertically-aligned films and arrays of CNT/nano-fibres (CNF), J_{knee} data was extracted from the field emission of "sparse", "dense" and "arrays" of CNF of 10^9, 10^7 and 10^6 CNF/cm^2 , respectively. [33] It is not possible to relate the CNT concentration of vertically-aligned CNT to that of the MWNT-PS matrix. However, based on the value of J_{knee}, it can be seen that films that are sparsely and densely grown have a value of J_{knee} around the 50% CNT-PS concentration. As for the Array of CNTs, J_{knee} falls within the region where the maximum value was observed from the MWNT-PS films. This gives an indication of the possible number of emitting CNT structures for the MWNT-PS film. Interestingly, the threshold fields of the CNF [33] are 4.5 to 3 V/μm, which is similar to those of the MWNT-PS films studied here.

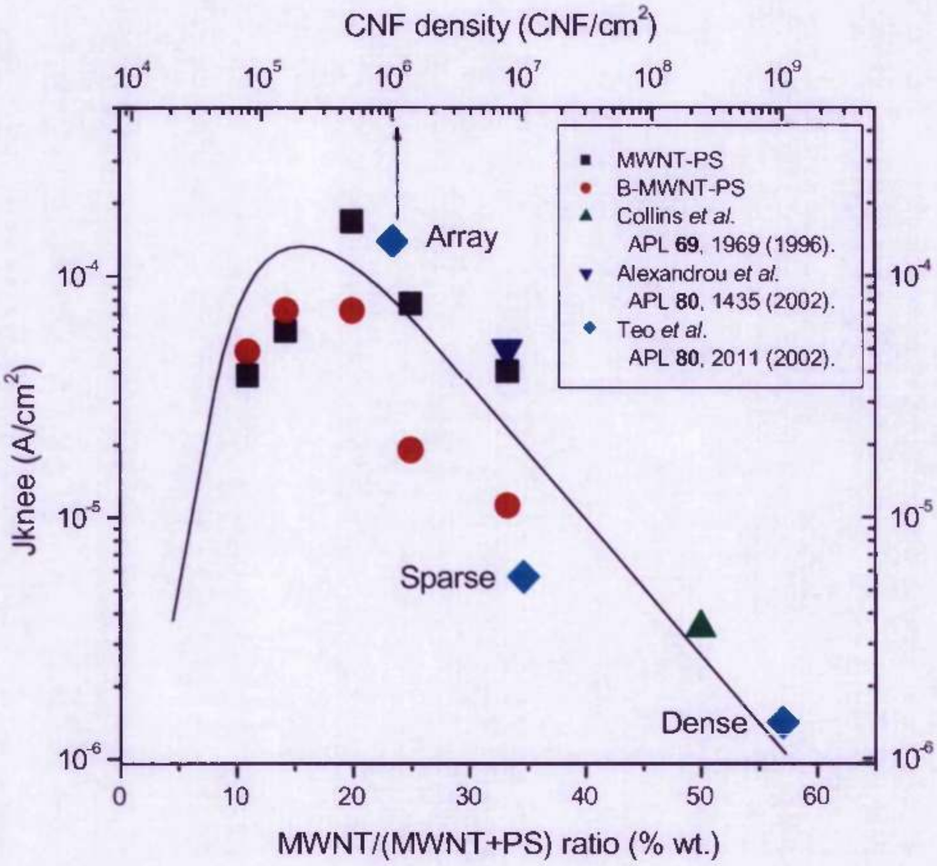

Figure 7-22: Comparison of the current saturation density J_{knee} as a function of the CNT concentration for different laboratories.

7.4.3 Current saturation effects

Electron field emission from carbon nanotubes (CNTs) has been extensively studied due to its low threshold fields [104] and high current densities [94]. It is essential to understand the behaviour of CNTs during high current density operation as it defines the limitations for applications as electron sources for high power vacuum microelectronics. Energy exchange processes during field emission becomes particularly important because the apex of these tubes are limited to a few nanometres. This would imply that a nanotube needs to sustain a very large current during the emission process. In fact, Dean *et al.* observed a large current density of 10^8 A/cm^2 from an isolated single-walled CNT during field emission.[105] Extrapolated current densities should be viewed with caution as it assumes linear scaling effects. However, the very high current density suggests that an intense amount of energy exchange is involved. There are two main phenomena associated with emission induced energy exchange processes. The Joule heating effect which was initially studied by Dyke *et al.* [106] and the "Nottingham" (cooling and heating) effect proposed by Henderson and Fleming [107] and later refined by Nottingham [108].

Resistive heating is usually associated with an unstable situation at high current density, where in the usual case, the resistivity increases rapidly with temperature. Interestingly, there have been reports that field emission from chemical vapour deposited (CVD) CNT induces luminescence and it was proposed that the phenomenon is mainly due to Joule heating along the body of the CNT [109,110]. However, as stable emission characteristics (current saturation) have been observed, [109,110] it indicates that Joule heating is not the only mechanism involved. The "Nottingham effect" on the other hand is a stabilizing effect, which can heat or cool a surface depending on the net energy of the emitted electrons [E_T] and the replacement energy of electrons [E_R]. The direction of energy exchange will be heating when [E_T] < [E_R] and cooling when [E_T] > [E_R].

Another important aspect for the Nottingham effect is the electronic transportation that occurs. Frank *et al.* have shown that multi-walled CNT (MWNT) conducts current ballistically and does not dissipate heat up to a current density of 10^7 A/cm^2. [111] Therefore, no energy is dissipated through the CNT and [E_R] is expected to be cold. It can be envisaged that variations in [E_T] at the apex of the CNT during field emission will be stabilised/cooled by [E_R]. Figure 7-23 illustrates the mechanism of cooling from a MWNT. The body of the tube is shown at a base temperature, *T*, with no joule heating $\Delta T \approx 0$ (change in temperature) due to ballistic electronic transportation. The Fermi level at the apex is shown to be higher in energy due to energy exchange during electron emission. When electrons traverse ballistically through the stem of the CNT, they are likely to be "hot", "electronically". But this electronic temperature will be converted to phonon energy due to the change in the shape and additional defects present at the tip of the CNT. This will cause "Joule" heating. In this work, the role of Nottingham effect and resistive heating has been considered in relation to current saturation during field emission from CNT.

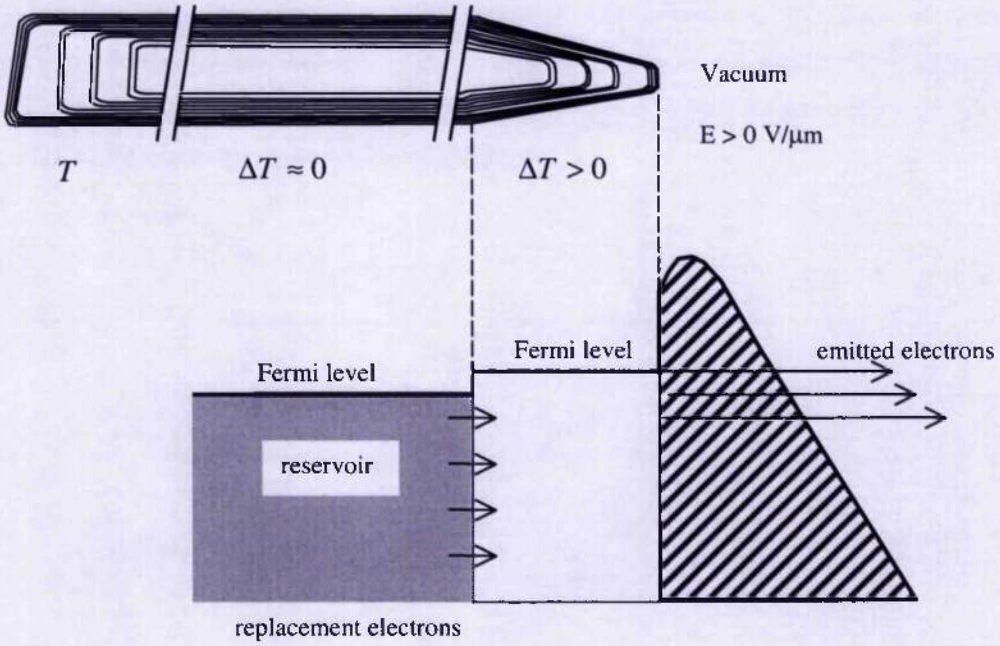

Figure 7-23: Schematic of field emission process from a MWNT. The apex region is illustrated with higher temperature than the body of the tube due to the effects of energy exchange during emission. Emitted electrons are replaced with cold electrons from the reservoir hence triggering a cooling effect.

As shown in Figure 7-12 and 7-13, the increase in MWNT concentration increases E_{th} in a linear manner. Interestingly, current saturation effects (CSE) are observed for both types of films at high current density. The saturation effects appear to be more significant at high MWNT concentrations, where, the current saturates at much lower current density. It is important to note that the field emission characteristics were measured for several cycles and stable measurements were obtained.

To investigate the saturation effect, one has to consider its value, E_{Knee}, which is the electric field at which current saturation begins. Figure 7-24 shows the variation of E_{Knee} as a function of E_{th} for both types of films. It is observed that E_{Knee} varies linearly with E_{th} with a slope of 1.24. Assuming that the y-intercept of the curve is zero, this is very close to the value observed by Collins *et al.*[112], which showed a linear relationship, with a slope of 1.29 for the turn-on voltage (for a 1 pA current) and saturation voltage. The similarity of the slope is all the more significant due to the fact that the threshold fields for emission in the two studies have been defined quite differently. The variation in E_{th} can be attributed to the effects of electric field screening that increases the emission threshold fields. Therefore, the emission process is limited by the local electric field. However, the saturation field that occurs at about 1.24 times of E_{th} suggests that the saturation effect is likely due the emission mechanism that is linearly related to the applied electric field.

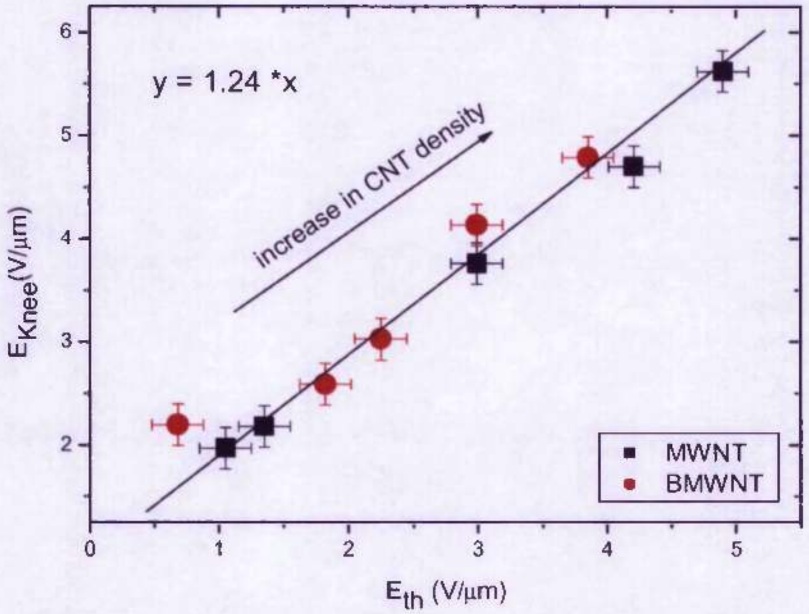

Figure 7-24: E_{Knee} plotted as a function of E_{th}. Showing a linear relationship of y = 1.24x.

The current saturation region can be fitted by an equation $J=kE^N$ where N is the saturation factor and k is a constant. The variation of the saturation factor as a function of the MWNT concentration is shown in Figure 7-25. In the classical vacuum space charge limited case,

$J=kE^{3/2}$. However, in this work, the lowest factor observed is 2.0, which clearly rules out that the charge saturation effect is due only to space charge limited current in the vacuum. Interestingly, the saturation factor increases with the MWNT concentration for both types of films. This seems to indicate that the amount of current saturation is affected by the amount of CNT within the polymer. This result also suggests that in order for the CNT to sustain a saturation effect linear to the CNT concentration, the mechanism that controls the saturation current has to come from within the CNT itself.

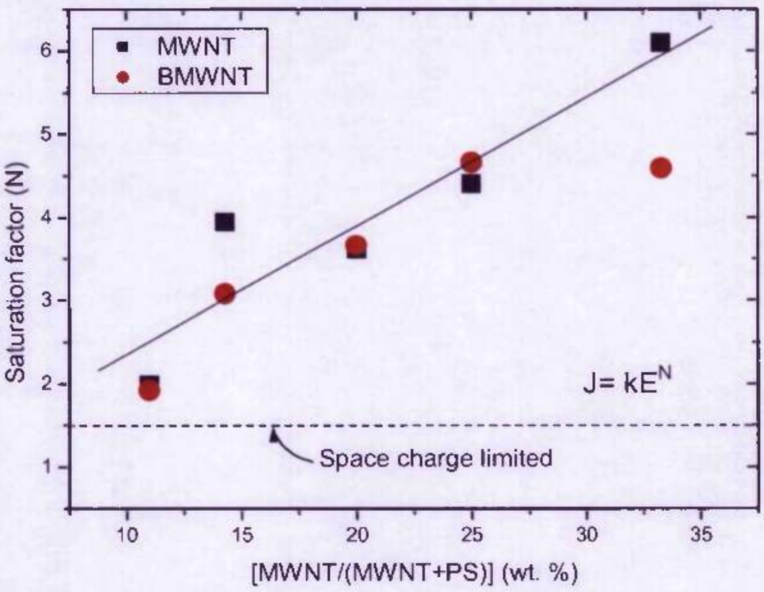

Figure 7-25: The current saturation factor (*N*) as a function of the MWNT concentration for both MWNT-PS films and BMWNT-PS films.

If we were to consider the field emission process to be dominated by tunnelling of electrons through a vacuum barrier described by the Fowler-Nordheim (F-N) model and the work function to be 5eV for all the films. The local field (F) at the apex of the CNT tip can be extracted using $F=\beta E$, where β is the F-N enhancement factor and E is the applied electric field. The F-N analysis of sample with 33% MWNT-PS composite film is shown in Figure 7-26.

The F-N slope (S_{FN}) obtained prior to saturation is -1.88 x 10^6, which gives a β factor of 406 and a local electric field for emission of about 2030 V/µm at the onset of emission. Considering that β=h/r (h and r is the height and radius of the emitter) and the average MWNT geometry in this work which is composed of 4 µm long and 10 nm in apex diameter CNT, the obtained β value is a realistic value of 200 to 800 considering the effects of field screening. Interestingly, the S_{FN} obtained for the saturation region is -2.97 x 10^5 which is lower than the S_{FN} before saturation. Since $S_{FN} = (-6.83 \times 10^7 \phi^{3/2}) / \beta$, an increase in S_{FN} would suggest that, 1) β increases at high field, or 2) ϕ got smaller in the saturation region, or 3) the emission no longer follows the F-N model, or 4) a mixture of the above three.

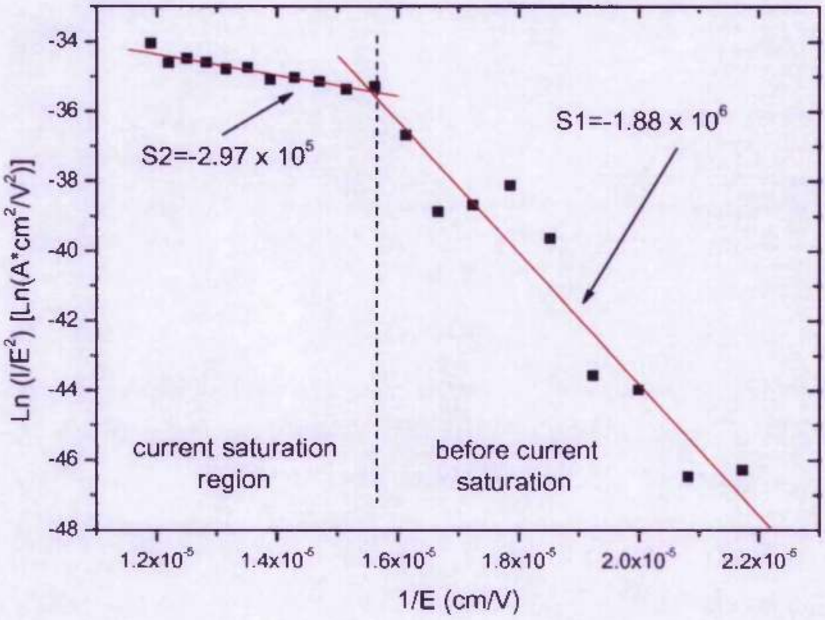

Figure 7-26: F-N plot of sample 33% MWNT-PS concentration. Solid lines resemble linear fitting for both region before and after saturation.

An increase in β seems unlikely because repeatable emission curves have been obtained and restructuring of the CNT cap [113] seems unlikely. Further evidence for stable emission from the CNT-PS films is shown in the field emission lifetime test. Figure 7-27 shows the variation of emission current over duration of 50 hours for a 20 % MWNT-PS film. The current density was measured before and after current saturation effects (see Figure 7-12) at 0.8 mA/cm^2 and 1.2 mA/cm^2 respectively. Despite slight variations initially for a current density of 1.2 mA/cm^2, stable emission has been observed over the 50 hr duration.

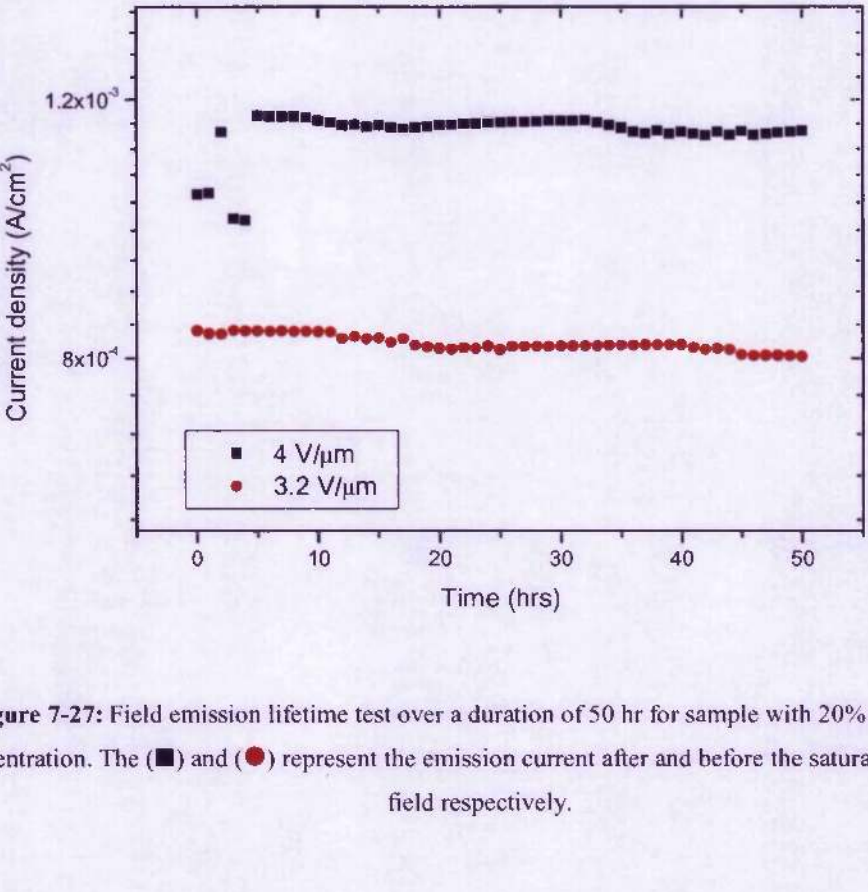

Figure 7-27: Field emission lifetime test over a duration of 50 hr for sample with 20% MWNT-PS concentration. The (■) and (●) represent the emission current after and before the saturation threshold field respectively.

However, variations in ϕ are possible if we consider that localised heating at the apex can occur during field emission. Reports have shown that field emission from defective CNT can induce localised heating up to 1500 K.[109] The field emission mechanism on the other hand, is likely to be dominated by electron tunnelling through a potential barrier rather than thermionic emission since electrons would not have acquired sufficient energy to surmount the barrier. If we were to take into account localised heating due to energy exchange processes, the emission current can be estimated [114] using:

$$J(F,T) = I_0(F)\frac{\pi p}{\sin(\pi p)} \qquad \textit{Equation 7-1}$$

$$I_0(F) = AF^2 \exp\left[-B\phi^{3/2} / F\right] \qquad \text{Equation 7-2}$$

Where, $p = k_B T / d$, $d \approx (9.76 \times 10^{-9} F) / \phi^{1/2}$, ϕ is the work function and F is the local electric field (V/cm) given by $F = \beta E$, A and B are F-N constants.

Equation 7-1 indicates that in order for the emission current to saturate, T needs to be stabilised or cooled. As Equation 7-1 is an inverted "sinc" function, the temperature cannot increase significantly as it will create an unstable current emission process. Therefore, the temperature at the apex of the tube should reach a maximum and then saturate. According to the Nottingham effect, the "inversion temperature" when no net energy exchange occurs is given by [114]:

$$T^* = (5.67 \times 10^{-5} F) / \phi^{1/2} \qquad \text{Equation 7-3}$$

Using the local field of obtained from F-N analysis where $F = 2030$ V/μm and $\phi = 5$ eV, and, T^* is found to be 515 K for a ϕ of 5 eV. If the surface energy at room temperature is [E] = $k_B T$ = 25 meV. Then [E] needs to increase by only 0.04 eV to obtain a local temperature of 515 K.

The expression that describes the temperature variation takes the form of $T_N + T_R$ which is the temperature rise due to Nottingham effect and Joule resistive heating respectively [114]:

$$T_A - T_0 = T_N + T_R$$

$$T_A = T_0 + [k_B T \cot \pi p / K(I_e / \alpha r)] + [\rho(T) / 2K\pi^2 (I_e / \alpha r)^2] \qquad \text{Equation 7-4}$$

where K is the thermal conductivity, I_e is the total emitted current, k_B is Boltzmann's constant, T_A and T_0 are the temperature at the apex and the body of the emitter respectively. αr is the product of the half angle of the tip and the radius of the tip. $\rho(T)$ is the bulk resistivity at temperature T and p is the field and temperature dependent factor given by $p = 9.3 x 10^5 \phi^{1/2} (T / E)$. Using T_0 =300 K, $\rho(T)$=10^5 Ω, K=1000 W m^{-1} K^{-1} and I_e= 60 μA, T_A is given by 873 K.

The very high thermal conductivity of the CNT is very useful in dissipating the energy (thermal) through the nanotubes itself. But, according to Equation 7-4 there is an inverse relation to K, and if the emitted energy of electrons is taken into account, this would be a convolution of an inverse T. Neither gives rise to a power law relationship for the current density to field or temperature. We think that the Nottingham effect now comes into play by providing a feedback loop which helps stabilise the emitted current.

Therefore, the emission process can be explained using the Nottingham effect by the direction of heating and cooling processes. The average energy of the conduction electrons at the apex region is affected by the temperature (T_A) at the apex region and is calculated to be 873 K. For $T_A < T^*$, emission heating can occur. This would increase the emission current and concurrently heating up T_A. However, when $T_A > T^*$, the cool electrons from the body of the CNT will cool the electrons at the apex region. T^* is calculated to be 515 K in our films. Therefore, we believe the inverse Nottingham effect stabilise the emission process and hence, the saturation of the emission current.

In conclusion, we have looked at the current saturation effects and have considered it in relation to the electronic transportation within the CNTs. The current saturation effect is strongly related to the energy exchange phenomena which is controlled by both the resistive heating and Nottingham effects. The thermal conductivity plays a very significant role in the current saturation, where the variation in MWNT concentration changes the current saturation factor.

7.4.4 Field emission model

The emission model for CNT is very much dependent on surface geometric enhancement. The very low threshold field from the nanotube emitter certainly originate from the very small diameter and very long length tube structure. The local field required to extract electrons from a metallic material with work function of 5 eV is about 2-3 x 10^3 V/μm. The electric field enhancement can be estimated by a factor of $\beta = h/r$ where h is the height of a single nanotubes and r the radius of curvature of the tip apex.

The proposed mechanisms for emission from CNT vary widely for different authors. Most authors observed two regions behaviour where an exponential F-N region was followed by a current saturation effect at high field. Fowler-Nordheim tunnelling theory has been well observed from experimental results. This suggests a tunnelling process due to electric field crowding at the sharp apex of a CNT with a workfunction similar to that of graphite. However, some work suggested that SWNT and MWNT are low workfunction emitters. Furthermore, the effects of absorbates have caused more confusion as the localised surface states are thought to improve the tunnelling probability of electron during field emission. Thus, the interpretations of results suggest that the field emission process may be more complicated than previously though with a simple model based on emission from a sharp metal-like surface. Multiple emission mechanisms may be responsible.

Field emission from CNT embedded in an insulating polystyrene matrix can be more complicated than emission from a single CNT film. Indeed the threshold field will be mostly controlled by the CNTs nearest to the anode or the CNT with the highest tunnelling probability. In which case, the overall emission must be dominated by only a region of a few microns or less which have these efficient emitters. The CNTs that are embedded within the polystyrene and near to the surface can also play a part in the emission process.

7.5 Summary

In conclusion, we have investigated the field emission characteristics of non-aligned MWNT-PS films and BMWNT-PS films. The threshold field from these films are mainly controlled by the amount of CNT mixed in the polymer matrix. The CNT concentration increases the effect of electrical field screening, and hence increases the threshold field. This work also suggests how simple it is to produce CNT emitters with field emission characteristics similar to those of vertically-aligned CNTs. We have also proposed a model which can explain the experimentally observed saturation in the current density of the CNT structures based on the inverse Nottingham effect.

Chapter 8

8 Influence of external stress on the field emission properties

8.1 Introduction

Stress can greatly influence the electronic properties of a material. It has been shown in Chapter 6 that the field emission properties of carbon thin films can vary according to the amount of intrinsic stress within the films. Threshold fields as low as 7 V/μm have been observed on a film with an intrinsic stress of 12 GPa, compared to 40 V/μm with intrinsic stress of 1 GPa. Stress/pressure can alter the electronic properties such as carrier density and interaction between the π and π^* bonds in carbon based materials. The beneficial effects on field emission were explained due to electronic band overlap effects and carbon cluster proximity effects. Among all carbon based materials, recent reports from carbon nanotubes have shown some unexpected and interesting results. Carbon nanotubes can be metallic or semiconducting depending on their chirality and diameter. The band gap was reported to vary linearly with stress at a ratio of $| dE_{gap}/d\sigma |$ =10.7 meV/GPa [115]. Using a semi-empirical tight-binding approach a semiconductor to metal transition was predicted when σ is greater than 10 GPa. [115] The study of electronic properties with stress is important in the view of the ability to manipulate carbon thin films and nanotubes. Additionally, it is interesting to study field emission properties when external stress is applied which could act as a basis for a pressure sensor.

8.2 Experimental setup

Two types of samples are used for this bending experiment, nanostructured amorphous carbon (a-C) thin films and carbon nanotube-polystyrene matrix (CNT-PS) thin films. Three a-C films with different intrinsic stress were used. These films are deposited on silicon substrates using Krypton as the assisting ions, and have intrinsic stress representing films with low (1 GPa), medium (6.5 GPa) and high intrinsic stress (11.7 GPa). The average threshold fields for field emission before bending are 37, 32 and 25 V/μm, respectively. For CNT-PS films, undoped CNTs with 8% wt. concentration were used. The average threshold field for CNT-PS film is about 2 V/μm. The preparation and characterisation of these samples was explained in Chapter 6 and 7. Compressive stress was applied to the samples using a three-point bending technique shown in Figure 8-1.The samples are bent using an optical fibre placed in the middle of the sample and two glass slides are used to clip at both ends of the sample to create a curvature. Optical fibres ranging from 50 μm to 1000 μm were used to allow different compressive stresses to be applied on the samples. The samples are cut into a dimension of 4 x 25 mm. Field emission properties were measured using the probe technique. The anode is place directly above the bent region where the stress is expected to be maximum.

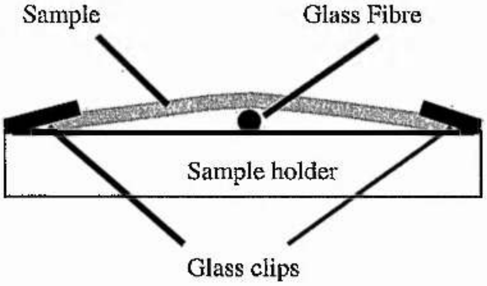

Figure 8-1: Sample stage of the film bending setup.

8.3 Effects of bending on a-C films

The variation in threshold fields for three a-C films as a function of the fibre diameter is shown in Figure 8-2. Bending the sample with different fibre sizes gives rise to different applied compressive stresses on the films. With increasing fibre size, an increased compressive stress is applied to the film. The variation in threshold field for the a-C with low intrinsic stress is shown in Figure 8-2 (a). It can be seen that as the fibre diameter increases from 0 to 125 μm, the threshold field decreases from 37 to 27 V/μm. This suggests that the increased compressive stress on the film enhances the field emission properties. However, further increase in the fibre diameter to 250 μm results in an increase of threshold field to 45 V/μm. It is expected that when excessive stress is applied on the film, relaxation of the microstructure can occur. Interestingly, this relaxation effect is reversible, and when the sample is unstressed after bending, the threshold field returns to 38 V/μm, similar to the value before bending. In Figure 8-2 (b), a similar cycle was observed for the a-C with medium intrinsic stress. The threshold field initially decreases from 31 to 17 V/μm, and, increases back to 22 V/μm when the fibre diameter increases from 0 to 125 μm and 250 μm respectively. Interestingly, when the fibre is tested post bending, the threshold field returns to 29 V/μm, which is in agreement with the sample with initial low intrinsic stress.

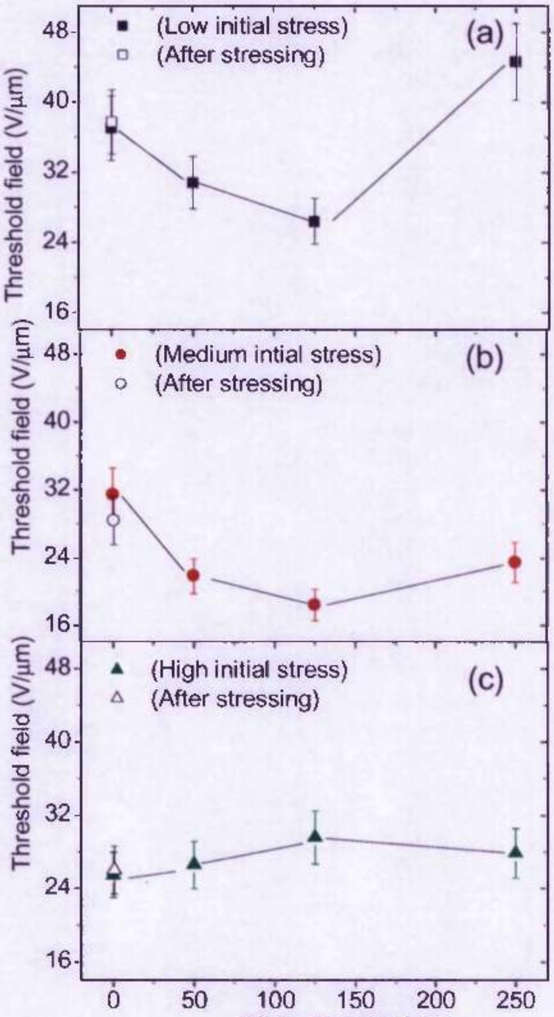

Figure 8-2: Threshold field as a function of the fibre diameter for (a) a-C thin film with initial stress of 1 GPa, (b) a-C thin film with initial stress of 6.5 GPa and (c) a-C film with initial stress of 11.7 GPa. Different fibre diameters represent different compressive stresses applied to these films externally.

The variation in threshold field for the film with high intrinsic stress is shown in Figure 8-2 (c). Despite bending the film with different fibre sizes, no significant changes in the threshold fields are observed. This can be attributed by the high intrinsic stress within the films, as it is not possible to induce any additional pressure which alters its "at equilibrium" microstructure. Comparing all three curves in Figure 8-2, it can be seen that the intrinsic stress within the a-C films controls the sensitivity of the bending process. The a-C film with high intrinsic stress was not responding to the bending process despite increasing the fibre diameter. However, a-C films with low and medium intrinsic stress did respond to the bending with a decrease in the threshold fields.

8.4 Effects of bending CNT-PS films

The bending of the CNT-PS films show different results from those of the a-C films. The a-C films are deposited on silicon substrates, which limit the maximum fibre size to 250 µm. Further bending of the a-C film results in cracking of the silicon substrates. However, the CNT-PS films are more flexible and hence thicker fibre sizes can be used. In this experiment, the film is bent up to a fibre size of 1000 µm. The variation in threshold field for CNT-PS films with 8 % wt. CNT concentration is shown in Figure 8-3. It can be seen that when the fibre size is increased from 0 to 500 µm, the threshold field decreases from 2.3 to 0.6 V/µm. When the fibre size is further increased to 1000 µm, the threshold field increases to 3.1 V/µm. Deformation of the sample was observed after bending the sample at 1000 µm. It can be seen that the deformation is due to melting of the polystyrene. In general, polystyrene turns into plastic from about 100 °C and melts at 340 °C. This suggests that when the films are bent at high curvature, stress induced changes on the CNTs could result in an increase effective temperature due to flow of high current densities through the film when subjected to field emission. At high current density, heating of the CNT above melting of the polystyrene could therefore cause deformation of the CNT-PS film. Interestingly, the decrease in threshold field is similar to those of a-C films with low and medium intrinsic stress.

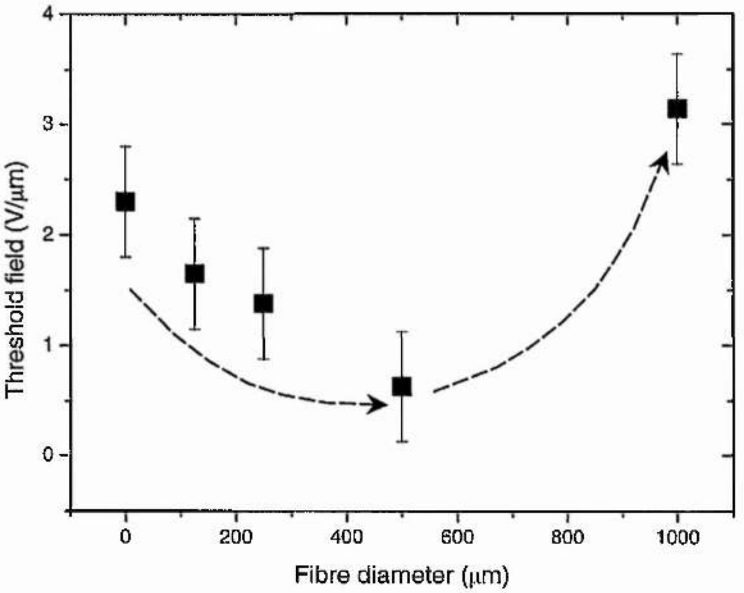

Figure 8-3: The variation of threshold field as a function of fibre diameter for CNT-PS films with 8 % *wt.* CNT concentration.

8.5 Summary and discussions

In summary, we have observed the effects of applying external stress on a-C films and CNT-PS films. The electron field emission properties are affected by the variation of compressive stress. The increases in stress on a-C films changes the electronic bands of the nanostructured carbon. This could be beneficial to field emission because, the π and π^* bands could shift towards each other or even overlap, hence increasing the electron concentration of the material. The illustration of the possible band structure modifications under the influence of stress is show in Figure 8-5. Stress/pressure on the a-C films can also cause the conductive carbon cluster to move closer to each other. This effect has been explained in Chapter 6, where the decrease in the separation distance between conductive clusters results in an increase in field enhancement, hence lower threshold fields. Using the following equation the variation in the electron concentration can be modelled:

$$n_e = \frac{8\pi m_e^* kT}{\hbar^2 c} \ln\left[1+\exp {}^{\eta}\!/_{kT}\right] \qquad \textit{Equation 8-1}$$

where c is the interplanar distance and η is the chemical potential. Assuming band overlap and m^*_e is the effective mass of an electron, this two-band model indicates that the decrease of c can lead to the increase of the electron concentration and/or η. This can benefit the electron emission process by providing a larger pool of electrons or lower barrier for emission.

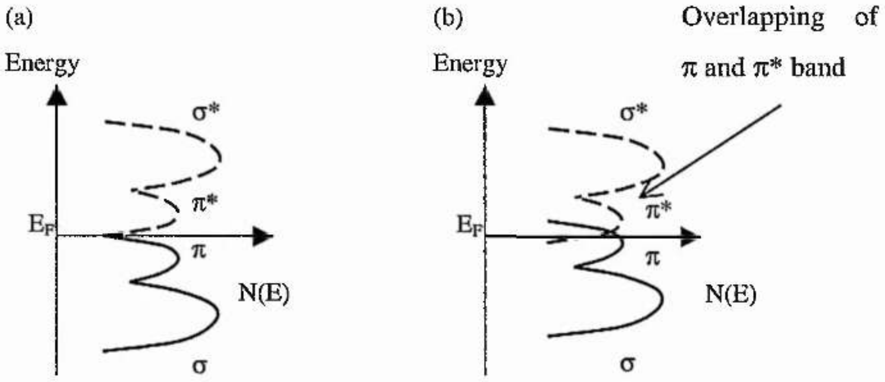

Figure 8-4 Effect of stress on the electronic bands of a-C film (a) before and (b) under the influence of stress/pressure.

As for the effects of stress on CNT-PS films, the variation is similar to that of a-C films. Under pressure, the band gap of the multi-walled nanotubes starts to decrease. Under a pressure of 10 GPa, a semiconductor to metal transition can occur when σ is greater than 10 GPa., hence increasing the density of states into a higher energy level. The band gap was reported to vary linearly with stress at a ratio of $|dE_{gap}/d\sigma|$ =10.7 meV/GPa [115].

The improved field emission characteristics can be explained using the F-N model. The emission current is dependent on both the supply function and transmission function. Traditionally, the supply function is described using Fermi-Dirac statistics to determine the energy distribution of electrons striking a metal surface. Therefore, the effect of stress can be viewed as increasing the supply function that increases the electron concentration at the emission surface.

Chapter 9

9 Conclusions

The work presented in this thesis studies critically the field emission characteristics of carbon based materials. Field emission properties from both amorphous carbon thin films and carbon nanotubes have been investigated. This study indicates the importance of the sp^2 hybridisation within the sp^3 matrix of the amorphous carbon thin films and rejects the early emphasis of a high sp^3 concentration in carbon films for good field emission properties. Although the field emission properties of carbon thin films are better understood, carbon nanotubes emerge as one of the most promising electron field emitters due to their low applied threshold fields and high emission current densities. This opens up the possibility for future device applications.

9.1 Amorphous carbon thin films

This work has illustrated the importance of the sp^2 phase within the amorphous carbon thin films for electron field emission. It is essential to consider three factors in order to understand the variations in threshold fields of these films.

1. The sp^2 configuration such as ring-like or chain-like configurations,
2. The sp^2 cluster size, and
3. The sp^2 concentration within the a-C:H films.

In Chapter 5, the deposition conditions were altered in order to modify these factors. Ar dilution changes the plasma chemistry during deposition without changing the composition of these films. The sp^2 content and the Tauc gap vary with the amount of Ar dilution. The Tauc gap was used to probe the sp^2 cluster size and the π bond concentration (measured by EELS) was used to estimate the sp^2 content. Results show that despite a lower sp^2 concentration and smaller sp^2 cluster, the 90% Ar diluted film exhibits the lowest threshold fields of the a-C:H films studied. Together with the optical density of these films, results point to the importance of having a-C:H films with a network of dense sp^2 bonding. The increased in Ar^+

bombardment during deposition results in smaller and fragmented sp^2 clusters being placed closer together. This would increase the field enhancement within the films as illustrated from the simulation of two conductive spheres.

Nitrogenation of the a-C:H films were designed to vary the conductivity and sp^2 concentration of the a-C:H films. The film conductivity and sp^2 concentration increase with N content. Interestingly, the emission threshold field increases with the sp^2 concentration unlike the results obtained in the Ar dilution section (Chapter 5.3.1). This difference can be explained based on the Raman analysis. The Raman result shows that the *G* peak shifts linearly with the N content, with no significant variation in the Raman *D* peak. The *D* peak is related to aromatic ring-like sp^2 configurations and the *G* peak is sensitive to both chain-like and ring-like configurations. This result suggests that in spite of an increase in the sp^2 concentration, these chain-like configurations are not beneficial to the field emission process.

The C_{60} ion implantation illustrated the effects of electric field screening. The C_{60} ions sputtered onto the a-C films leaves a layer of graphitic carbon on the surface. During field emission, the conductive layer screens away the electric field and prevented field penetration into the carbon thin film. This results in an increase in the field emission threshold fields.

The field emission properties of the as-deposited graphite-like amorphous carbon thin films show a close relationship to the intrinsic stress which is controlled by different ions and ion energies. The films are very graphitic with sp^2 concentrations close to 80% for all the dual ion beam deposited films. The increase in intrinsic stress results in an increase in the sp^2 clusters or "nano-structured carbon", with the clusters being moved spatially closer together which give rise to a higher internal non-geometric field enhancement. The variation in compressive stress also modifies the band structure of the nano-structured carbon. Stress on this graphitic carbon causes increased band over-lapping. In some cases, the valence band can overlap the Fermi level, which can be favourable for field emission.

Findings from the 2-D simulation gives good insight to the field enhancement mechanism. Two conductive spheres were embedded in a low dielectric matrix. This electrostatic problem was modelled under an uniform electric field applied across two parallel electrodes and the separation between these spheres was varied. By decreasing the distance from 15 nm to 1 nm, the field enhancement factor increases from 10 to 22. This simulation suggests the importance of having conductive clusters close to each other. Hence, the effect of having a film with high stress and high local density seems crucial in obtaining high field enhancement during field emission. This simulation result is in agreement with the model proposed by Carey *et al.*[18] and can be used to explain low threshold field from carbon based materials.

9.2 Carbon nanotubes

Carbon nanotubes were mixed into a polystyrene matrix to produce composite films for field emission testing. Using a hot pressing technique on the CNT-PS films, good quality films were produced. Carbon nanotubes have indeed shown good field emission capability, and to date exhibit the lowest threshold fields reported with high current densities. Threshold fields as low as 1.6 V/μm have been observed. However, despite the differences in the electronic properties of a B-MWNT and undoped MWNT, the field emission characteristics show the emission to be controlled mainly by the high geometric field enhancement. The effect of this field crowding at the apex of the nanotubes results in extremely high electric field enhancement that gives rise to electron emission at low macroscopic fields. There are still problems posed to the applications for carbon nanotubes for field emission displays such as, electric field screening and current saturation effects. To overcome these effects of field screening, the control of the carbon nanotube concentration on the polymer surfaces needs to be taken into consideration.

The emission site density results show a close relationship with the nanotube concentration. The emission map from these films shows "spotty" type emission, which suggests that the emission process is dominated by those nanotubes with high field enhancement. An emission site density of 10^7 sites/cm^2 was obtained using low voltage phosphors which meets the requirements of a field emission displays. However, further investigation of the phosphors is required in order to optimise display performance. Long and stable lifetime tests have also been conducted on these CNT-PS films. Over a period of 50 hrs continuous testing, there was no significant variation of the emission current. Therefore, this suggests that the industrial potential of using CNT-PS composite material as field emitters.

The origin of current saturation was studied in this work. The effect of current saturation was attributed to the energy exchange processes during field emission. Both resistive heating and Nottingham heating/cooling were considered. Due to the unique properties of CNT, ballistic conduction within the body of the tube provides a reservoir of "cool" replacement electrons. This provides a feedback loop in the field emission process which helps to stabilise the emission process. This cooling effect therefore results in the saturation of emission current at high fields.

A novel sensor based on the relationship between stress and electron field emission in carbon-based materials has been proposed.

9.3 Suggestions for future research

There are number of research avenues that will supplement this study, including:

- Application of pressure/stress of amorphous carbon thin films as a sensor. Using the benefit of the pressure sensitive property during field emission, a high power transducer can be designed to allow pressure sensitive operation.
- X-ray sources with low voltage operation and high current densities. Using a copper anode together with a modulating circuit, a portable and compact x-ray source can be designed.
- Incorporation of nanotubes into a polymer matrix for re-enforced polymer materials. Mixing CNT into a polymer not only changes its electronic property, it also increases the mechanical property of the polymer.
- Field emission lamp/light bulbs, based on cheap CNT-polymer composite materials. It is cheap and easy to produce these CNT-PS films, if suitable phosphors can be used. A very economical light source can be produced for light emitting applications.

The aim of the research reported in this thesis has been to understand the mechanism of electron field emission from carbon based materials. In spite of the encouraging results obtained, the field emission process still remains unclear in some areas and requires further studies, in particular, correlating field emission results to the proposed theories. Thus far many analyses have been simplified by using assumptions that are over simplistic and the actual emission process from carbon based materials may be more complicated. Therefore, this thesis can be used a foundation for future research in this area.

References

---

[1] H. W. Kroto, J. R. Heath, S. C, O'Brien, R. F. Curl, and R. E. Smalley, Nature (London) **318**, 162 (1985).

[2] S. Iijima, Nature (London) **354**, 56 (1991).

[3] C. A. Spindt, J. Appl. Phys. **39**, 3504 (1968).

[4] R. H. Fowler, L. Nordheim Proc.R. Soc. Lon. **A119**, 173 (1928).

[5] C. A. Spindt, J. Appl. Phys. **39**, 3504 (1968).

[6] R. G. Forbes, C. J. Edgcombe and U. Valdrè, Ultramicroscopy **95**, 57 (2003).

[7] T. Utsumi, IEEE Trans. Electron Devices **38**, 2276 (1991).

[8] W. A. Mackie, R. L. Hartman, M. A. Anderson, and P. R. Davis J. Vac. Sci. Technol. B **12**, 722 (1994).

[9] K. H. Bayliss, R. V. Latham, Proc. Roy. Soc. A **403** 285 (1986).

[10] G. A. J. Amaratunga and S. R. P. Silva, Appl. Phys. Lett. **68**, 2529 (1996).

[11] S. Aisenberg, and R.Chabot, J. Appl. Phys. **42**, 2953 (1971).

[12] M. W. Geis, J. C. Twichell, T. M. Lyszczarz, J. Vac. Sci. Technol. B. **14**, 2060 (1996).

[13] O. Groning, O. M. Kuttel, P. Groning, L. Schlapbach, J. Vac. Sci. Technol. B. **17** 1064 (1999).

[14] J. D. Carey, R. D. Forrest, R. U. A. Khan, and S. R. P. Silva, Appl. Phys. Lett. **77**, 2006 (2000).

[15] A. Ilie, A. C. Ferrari, T. Yagi and J. Robertson, Appl. Phys. Lett. **76**, 2627 (2000).

[16] A. Ilie, A. C. Ferrari, T. Yagi, S. E. Rodil, J. Roberston, E. Barborini, and P. Milani, J. App. Phys. **90**, 2024 (2001).

[17] J.Robertson, J.Vac.Sci.Technol.B, **17**, 659 (1999).

[18] J. D. Carey, R. D. Forrest, S. R. P. Silva, Appl. Phys. Lett. **76**, 2339 (2001).

[19] P. C. Chaumet, J. P. Dufour, J. Electrostat. **43**, 145 (1998).

[20] B. S. Satyanarayana, A. Hart, W. I. Milne, J. Robertson, Diam. & Relat. Mater. **7**, 656 (1998).

[21] L. K. Cheah, X. Shi, E. Liu, and B. K. Tay, J. Appl. Phys. **85**, 6816 (1999).

[22] N. Missert, T. A. Friedmann, J. P. Sullivan, and R. G. Copeland, Appl. Phys. Lett. **70**, 1995 (1997).

[23] A. Ilie, A. Hart, A. J. Flewitt, J. Robertson, and W. I. Milne, J. Appl. Phys. **88**, 6002 (2000).

---

[24] J. Schwan, S. Ulrich, V. Bathori, H. Erhardt, and S. R. P. Silva, J. Appl. Phys. **80**, 44 (1996).

[25] R. D. Forrest, A. P. Burden, S. R. P. Silva, L. K. Cheah, and X. Shi, Appl Phys. Lett. **73** 3784 (1998).

[26] Y. G. Baek, T. Ikuno, J. T. Ryu, S. Honda, M. Katayama, K.Oura, T. Hirao, Appl. Surf. Sci. **185**, 243 (2002).

[27] A. N. Obraztsov, I. Y. Pavlovsky, A. P. Volkov, A. S. Petrov, V. I. Petrov, E. V. Rakova, V. V. Roddatis, Dia. & Relat. Mater. **8**, 814 (1999).

[28] A. N. Obraztsov, I. Y. Pavlovsky, and A. P. Volkov, J. Vac. Sci. Technol. B **17**, 674 (1999).

[29] G. Y. Chen, J. S. Chen, Z. Sun, Y. J. Li, S. P. Lau, B. K. Tay, J. W. Chai, Appl. Surf. Sci. **180**, 185 (2001).

[30] S. P. Lau, Y. J. Li, B. K. Tay, Z. Sun, G. Y. Chen, J. S. Chen, X. Z. Ding, Diam. & Relat. Mater. **10**, 1727 (2001).

[31] Y. Saito, K. Hamaguchi, R. Mizushima, S. Uemura, T. Nagasako, J. Yotani, T. Shimojo, App. Surf. Sci. **146** 305 (1999).

[32] D. L. Carroll, P. Redlich, P. M. Ajayan, S. Curran, S. Roth, and M. Rühle, Carbon, **36**, 753 (1998).

[33] K. B. K. Teo, M. Chhowalla, G. A. J. Amaratunga, W. I. Milne, G. Pirio, P. Legagneux, F. Wyczisk, D. Pribat, D. G. Hasko, Appl. Phys. Lett. **80** 2011 (2002).

[34] L. Nilsson, O. Groening, C. Emmenegger, O. Kuettel, E. Schaller, L. Schlapbach, H. Kind, J-M. Bonard, and K. Kern, Appl. Phys. Lett. **76**, 2071 (2000).

[35] N. I. Sinitsyn, Y. V. Gulyaev, G. V. Targashov, L. A. Chernozatonskii, K. Kosakovskaya, Y. F. Zakharchenko, N. A. Kiselev, A. L. Musatov, A. I. Zhbanov, S. T. Mevlyut, O. E. Glukhova, Appl. Surf. Sci. **111**, 145 (1997).

[36] W. A. De Heer, A. Chatelain, D. Ugarte, Science, **270**, 1179 (1995).

[37] P. G. Collins, A. Zettl, Appl. Phys. Lett. **69**, 1969 (1996).

[38] W. Zhu, C. Bower, O. Zhou, G. Kochanski, S. Jin, Appl. Phys. Lett. **75**, 873 (1999).

[39] X. Xu, G. R. Brandes, Appl. Phys. Lett. **74**, 2549 (1999).

[40] X. Ma, E. Wang, Z. Wuzong, D. A. Jefferson, C. Jun, D. Shaozhi, X. Ningshen, Y. Jun, Appl. Phys. Lett. **75**, 3105 (1999).

[41] W. A. Chupka, and J. Berkowitz, J. Chem. Phys. **54**, 4256 (1971).

[42] N. Mutsukura, and K. Miyatani, Dia. Relat. Mater. **4**, 342 (1995).

---

[43] A. Raveh, J. E. Klemberg-Sapieha, L. Martinu, and M. R. Wertheimer, J. Vac. Sci. Technol. A **10**, 1723 (1992)

[44] J. D. Carey, R. D. Forrest, R. U. A. Khan, and S. R. P. Silva, Appl. Phys. Lett. **77**, 2006 (2000).

[45] S. Bosch, Microscopy and Analysis, pp. 49 (1991).

[46] R. A. Street, Hydrogenated Amorphous Silicon (Cambridge University Press, 1991).

[47] J. Tauc, The optical properties of solids (North Holland, Amsterdam, 1970).

[48] R. W. Hoffman, Physics of Thin Films edited by G. Hass, and R. E. Thun (Academic, New York, 1966), Vol. 3, pp. 211-273.

[49] R. F. Egerton, *Electron Energy Loss Spectroscopy in the Electron Microscopy* (Plenum, New York, 1986).

[50] U. Hoffmann, A. Weber, T. Lohken, C. P. Klages, C. Spaeth, F. Richter, Dia. & relat. Mater. **7**, 682 (1998)

[51] S. R. P. Silva, R. D. Forrest, D. A. Munindradasa, G. A. J. Amaratunga, Dia. & relat. Mater. **7**, 645 (1998)

[52] M. T. Kuo, P. W. May and M. N. R. Ashfold, Dia. & Relat. Mater. **11**, 1422 (2002).

[53] N. Missert, T. A. Friedmann, J. P. Sullivan, and R. G. Copeland, Appl. Phys. Lett. **70**, 1995 (1997).

[54] Y. Umehara, S. Murai, Yasuo Koide and Masanori Murakami, Dia. & Relat. Mater. **11**, 1429 (2002).

[55] G. K. Wachutka, IEEE trans., Computer-Aided Design, Vol. **9**, No. 11, pp. 1141 (1990).

[56] S. Tam, P. K. Ko, and C. Hu, IEEE Tran. ED **31**, N9 (1984).

[57] See, for example, *Proceedings of the First International Specialist Meeting on Amorphous Carbon*, edit by S. R. P. Silva, J. Robertson, W. I. Milne, and G. A. J. Amaratunga (World Scientific, Singapore 1998).

[58] A. Ilie, A. C. Ferrari, T. Yagi, and J. Robertson, Appl. Phys. Lett. **76**, 2627 (2000)

[59] E. Tomasella, C. Meunier, and S. Mikhailov, Surf. Coat. Technol. **141**, 286 (2001).

[60] L. Valentini, J. M. Kenny, G. Mariotto, P. Tosi, G. Carlotti, D. Fioretto, L. Lozzi, and S. Santucci, Diamon Relat. Mater. **10**, 1088 (2001)

[61] J. D. Carey, S. R. P. Silva, Appl. Phys. Lett. **78**, 347 (2001).

[62] P. J. Fallon, V. S. Veerasamy, C. A. Davis, J. Robertson, G. A. J. Amaratunga, and W. I. Milne, Phys. Rev. B **48**, 4936 (1999).

[63] S. R. P. Silva, K. J. Clay, S. P. Speakman, and G. A. J. Amaratunga, Diam. Relat. Mater. **4**, 977 (1995).

---

[64] B. S. Satyanarayana, A. Hart, W. I. Milne, and J. Robertson, Appl. Phys. Lett. **71**, 1430 (1997)

[65] S. R. P. Silva, R. D. Forrest, D. A. Munindradasa, and G. A. J. Amaratunga, Diam. Ret. Mater. **7**, 645 (1998).

[66] A. A. Talin, L. S. Pan, K. F. McCarty, T. E. Felter, H. J. Doerr, and R. F. Bunshah, Appl. Phys. Lett. **69**, 3842 (1996).

[67] *See chapter 6 for further discussion.*

[68] R. U. A. Khan, J. D. Carey, S. R. P. Silva, B. J. Jones, and R. C. Barklie, Phys. Rev. B. **63**, 121201 (2001).

[69] M. Chhowalla, A. C. Ferrari, J. Robertson, and G. A. J. Amaratunga, Appl. Phys. Lett. **76**, 1419, (2000).

[70] V. S. Veerasamy, J. Yuan, G. A. J. Amaratunga, W. I. Milne, K. W. R. Gilkes, M. Weiler, and L. M. Brown, Phys. Rev. B **48**, 8016 (1993).

[71] S. R. P. Silva, G. A. J. Amaratunga, Thin Solid Films **270**, 194 (1995).

[72] A. C. Ferrari, and J. Robertson, Phys. Rev. B **61**, 14905 (2000).

[73] M. M. de Lima Jr, R. G. Lacerda, J. Vilcarromero, and F. C. Marques, J. Appl. Phys. **86**, 4936 (1999).

[74] J. D. Carey, and S. R. P. Silva Appl. Phys. Lett. **78**, 347 (2001).

[75] A. C. Ferrari and J. Robertson, Phys. Rev. B **61**, 14095 (2000).

[76] C. Ronning, E. Dreher, J.-U. Thiele, P. Oelhafen, and H. Hofsass, Diam. Relat. Mater. **6**, 830 (1997).

[77] D. R. McKenzie, D. Muller, B. A. Pailthope, Phys. Rev. Lett. **67**, 773 (1991).

[78] J. Schwan, S. Ulrich, T. Theel, H. Roth, H. Ehrhardt, P. Becker, and S. R. P. Silva, J. Appl. Phys. **82**, 6024 (1997)

[79] Y. Lifshitz, S. R. Kasi, J. W. Rabalais, W. Eckstein, Phys. Rev. B. **41**, 10468 (1990).

[80] J. Robertson, Diam. Relat. Mater. 2, 984 (1993).

[81] R. G. Lacerda, P. Hammer, C. M. Lepienski, F. Alvarez, F. C. Marques, J. Vac. Technol. A. **19**, 971 (2001).

[82] S. Bhattacharyya, S.V. Subramanyam, Appl.Phys. Lett. **71** 632 (1997)

[83] C.Kilic, H. Mehrez, S. Ciraci, Phys. Rev. B. **12**, 7872 (1998).

[84] C. Uher, R. L. Hockey, E. Ben-Jacob, Phys. Rev. B. **35**, 4483 (1987).

[85] P. Hammer, N. M. Victoria, F. Alvarez, J. Vac. Sci. Technol. A **18**, 2277 (2000).

---

[86] M. Chhowalla, J. Robertson, C. W. Chen, S. R. P. Silva, C. A. Davis, G. A. J. Amaratunga, and M.I. Milne, J. App. Phys. 81, 139 (1997).

[87] B. Andre, F. Rossi, A. van Veen, P. E. Mijnarends, H. Scht, and M. P. Delplancke, Thin. Soild Films **241**, 171 (1994).

[88] R. W. Lynch and H. G. Drickamer, J. Chem. Phys. **44**, 181 (1966).

[89] R. Ahuja, S. Auluck, J. Trygg, J. M. Wills, O. Eriksson, B. Johansson, Phys. Rev. B. 51, 4813 (1995).

[90] W.N. Reynolds, P.R. Goggin Phil. Mag. **5**, 1049 (1960).

[91] C. Bandis and B. B. Pate, Appl. Phys. Lett. **69**, 4123 (1996).

[92] O. Groening, O. M. Kuttel, P. Groening, and L. Schlapbach, Appl. Phys. Lett. **71**, 2253 (1997).

[93] K.H. Bayliss and R. V. Latham, Proc. R. Soc. London, Ser. A 403, 285 (1986).

[94] W. Zhu, C. Bower, O. Zhou, G. Kochanski and S. Jin, Appl. Phys. Lett. **75**, 873 (1999).

[95] W.K. Hsu, S.Y. Chu, E. Munoz-Picone, J.L. Boldu, S. Firth, P. Franchi, B.P. Roberts, A. Schilder, H. Terrones, N. Grobert, Y.Q. Zhu, M. Terrones, M.E. McHenry, H.W. Kroto, D.R.M. Walton, Chem. Phys. Lett., **323**, 572 (2000).

[96] P.C.P. Watts, W.K. Hsu, G.Z. Chen, D.J. Fray, H.W. Kroto, D.R.M. Walton, J. Mat. Chem.**11**, 2482, (2001).

[97] S. R. P. Silva, J. D. Carey, R. U. A. Khan, E. G. Gerstner, and J. U. Angutia, Handbook of thin film material, edited by H. S. Nalwa (Academic, New York, 2002), p. 484.

[98] J. P. Barour, W. W. Dolan, J. K. Tron, E. E. Martin, and W. P. Dyke, Phys Rev. **92**, 45 (1953).

[99] W. A. Anderson, J. Vac. Sci. Technol. B **11**,383 (1993).

[100] K. A. Dean, and B. R. Chalamala, Appl. Phys. Lett. **76**, 375 (2000).

[101] J. T. L. Thong,a) C. H. Oon, W. K. Eng, W. D. Zhang and L. M. Gan, Appl. Phys. Lett. **79**, 2811 (2001).

[102] I. Alexandrou, E. Kymakis, G. A. J. Amaratunga, Appl. Phys. Lett. **80** 1435 (2002).

[103] Current density extracted from ref. 8 was based on an emission test area of the 3mm diameter conducting grid describe by the author. Jknee in this work was the transition between region I and II.

[104] C. H. Poa, S. R. P. Silva P. C. P. Watts, W. K. Hsu, H. W. Kroto, and D. R. M. Walton, Appl. Phys. Lett. **80**, 3189 (2002).

[105] K. A. Dean, and B. R. Chalamala, Appl. Phys. Lett. **76**, 375 (2000).

---

[106] W. P. Dyke, J. K. Trolan, E. E. Martin, and J. P. Barbour, Phys. Rev. **91**, 1043 (1953).

[107] J. Henderson, and G. M. Fleming, Phys. Rev. **58**, 887 (1940).

[108] W. B. Nottingham, Phys. Rev. **59**, 907 (1941).

[109] S. T. Purcell, P. Vincent, C. Jourent, and Vu Thien Binh, Phys. Rev. Lett. **88**, 105502 (2002).

[110] M. Sveningsson, M. Jönsson, O. A. Nerushev, F. Rohmund, and E. E. B. Cambell, Appl. Phys. Lett. **81**, 1095 (2002).

[111] S. Frank, P. Poncharal, Z. L. Wang, W. A. de Heer, Science **280**, 1744 (1988).

[112] P.G. Collins, A. Zettl, Phy. Rev. B. **55**, 9391 (1997).

[113] K. A. Dean, T. P. Burgin, and B. R. Chalamala, Appl. Phys. Lett. **79**, 1873 (2001).

[114] L. W. Swanson, L. C. Crouser, and F. M. Charbonnier, Phys. Rev. **151**, 327 (1966).

[115] R. Heyd, A. Charlier, and E. McRae Phys. Rev. B. **55** 6820 (1997).

Publications

- *Modification of electron field emission properties from surface treated amorphous carbon thin films.* J. D. Carey, C. H. Poa, R. D. Forrest, A. P. Burden, S. R. P. Silva, J. Vac Sci. Technol. B **18,** 1051 (2000).
- *Conditioning of amorphous cathodes via current stressing.* S. R. P. Silva, J. D. Carey, C. H. Poa, and J. M. Shannon, *in Cold Cathodes, Proceedings from the First International Symposium on Cold Cathodes*, Eds. M. Cahay, K. L. Jensen, P. D. Mumford, J. Yater, R. A. Murphy, D. Temple and V. J. Kapoor, The Electrochemical Society, vol. **2000-28**, pp. 226-246 (2001).
- *Field emission from non-aligned carbon nanotubes embedded in a polystyrene matrix.* C. H. Poa, S. R. P. Silva, P. C. P. Watts, W. K. Hsu, H. W. Kroto, D. R. M. Walton. Appl. Phys. Lett. **80,** 3189 (2002).
- *Stress-induced electron emission from nanocomposite amorphous carbon thin films.* C. H. Poa, R. G. Lacerda, D. C. Cox, S. R. P. Silva, and F. C. Marques. Appl. Phys. Lett. **81**, 853 (2002).
- *Effects of Ar dilution on the properties of hydrogenated amorphous carbon thin film.* C. H. Poa, R. G. Lacerda, D.C. Cox and S.R.P. Silva. Thin solid films (in press)
- *Unraveling the field emission properties of non-aligned carbon nanotubes.* C. H. Poa, R. C. Smith and S. R. P. Silva, P. C. P. Watts, W. K. Hsu, H. W. Kroto, and D. R. M. Walton. J. Vac. Sci Technol. B (in press)
- *Effects of Stress on Electron Emission from Nano-Structured Carbon Materials.* C.H. Poa, R. G. Lacerda, D. C. Cox, F. C. Marques and S.R.P. Silva. J. Vac. Sci Technol. B (in press).
- *Role of nanostructure on the electron field emission from amorphous carbon thin films.* J.D. Carey, R.D. Forrest, C.H. Poa and S.R.P. Silva. J. Vac. Sci Technol. B (in press).

Presentation list

- *Origin of Field Emission Enhancement Factors in Amorphous Carbon Thin Films.* C. H. Poa, J. D. Carey and S. R. P. Silva, Network on Diamond and Diamond-like Carbon, 28 June 2001,Møller Centre, Churchill College, Cambridge, U.K
- *Field emission from graphitic nanostructures in amorphous carbon thin films.* C. H. Poa, R. G. Lacerda, D. C. Cox, F. C. Marques and S. R. P. Silva, Nanotechnology in Carbon and Related Materials Conference, NanoteC'01, 29th August - 1st September 2001, University of Sussex at Brighton, U.K
- *Non-geometric field enhancement from graphite-like amorphous carbon thin films.* C. H. Poa, R. G. Lacerda, D. C. Cox, F. C. Marques and S. R. P. Silva, 3rd European Field Emission Workshop, EUROFE 2001,12th -16th November 2001, Alicante, Spain.
- *Effects of Ar dilution on the properties of hydrogenated amorphous carbon thin film.* C. H. Poa, R. G. Lacerda, V. Stolojan, D. C. Cox and S. R. P. Silva, The International Conference On Metallurgical Coatings And Thin Films, ICMCTF 2002, April 22 - April 26, 2002, Town and Country Hotel, San Diego, California, USA.
- *Field emission properties of carbon nanotube-polystyrene composite materials.* C. H. Poa, R. C. Smith, S. R. P. Silva, P. C. P. Watts, W. K. Hsu, H. W. Kroto, D. R. M. Walton, 15th International Vacuum Microelectronics Conference 48th International Field Emission Symposium, July 1-11 2002, Lyon, France.
- *The Application of Nanostructured Amorphous Carbon Thin Films as an Efficient Electron Source.* C. H. Poa, R. G. Lacerda, D. C. Cox, and S. R. P. Silva, F. C. Marques, 15th International Vacuum Microelectronics Conference 48th International Field Emission Symposium, July 1-11 2002, Lyon, France.